

天主教輔仁大學物理學系碩士論文

指導教授：張敏娟

Belle-II實驗中進行CDC偵測器二維軌跡標定

CDC 2-D Track finding at Belle-II experiment

研究生：黃誠亨 撰

中華民國一百年七月

私立輔仁大學物理學系碩士班  
論文口試委員會審定書  
黃誠亨先生之論文  
Belle-II 實驗中進行 CDC 偵測器二維  
軌跡標定  
CDC 2D Track Finding at Belle-II  
experiment

經本委員會議合格，特此證明。

論文口試委員

職稱	姓名	<u>張敏娟</u>
助理教授	張敏娟	<u>王正祥</u>
教授	王正祥	<u>王名儒</u>
教授	王名儒	

系主任



中華民國 100 年 07 月 29 日

# 摘要

位於日本筑波市的高能加速機構中(KEK)的加速器(KEKB)以及偵測器(Belle)在運行超過10年後，於2010年7月開始，關機並且進行升級計畫。計畫內容分為兩大部分，一部分是屬於加速器的升級(Super KEKB)，另一部分是屬於偵測器的升級(Belle-II)。

隨著偵測器的升級，隸屬於偵測器中的子偵測器們也要跟著升級。其中我們輔大高能實驗室所加入的團隊是其中一個子偵測器“中央飄移室”(Central Drift Chamber, CDC)中的觸發信號小組。CDC偵測器主要目的是量測帶電粒子的軌跡及動量，是提供整個偵測器裡的粒子鑑別的一樣利器。因此在CDC中對於軌跡的判定是特別的重要。

這篇論文主要做的是CDC偵測器中的二維軌跡判定。我們利用霍夫轉換(Hough transform)的演算法，在霍夫平面下找到帶電粒子的軌跡路徑方程。我們藉由模擬單一帶電粒子通過CDC時的狀況，分類出幾種狀況，並且提出對應方法。在成功獲得帶電粒子軌跡方程後，我們也做了以下研究:(1)在不同粒子帶有相同動量時，及(2)相同粒子帶有不同動量時的軌跡圓的變化研究，並且(3)利用軌跡方程回推動量。我們發現對各種情況下的分類對應解法，是個不錯個方法。最後也找出了最佳的解析度大小，讓二維軌跡判定的成功率更高及回推的動量更準確。

關鍵詞:日本高能研究加速機構、Belle-II、中央飄移室、二維軌跡標定、霍夫轉換。

# Abstract

High Energy Accelerator Research Organization (KEK) is located in Tsukuba city, Japan. An accelerator KEKB and a detector Belle are located in a tunnel inside KEK. Belle experiment is operated for 11 years. It is stopped for upgrade in 2010 July. The upgrade accelerator is named SuperKEKB, and the upgrade detector is named Belle-II.

The Fu Jen Catholic University high energy lab joins the Central Drift Chamber(CDC) trigger system group. The main purpose of CDC chamber is to measure the trajectory and momentum of charged particles. CDC is an important tool to identify charged particles.

This thesis describes two dimensional track finding method in CDC trigger system. We use the Hough transform algorithm to find the trajectory equation of charged particle in Hough plane and translate back to CDC x-y plane. We simulate a single charged particle which pass through the CDC chamber. We classify cluster cases and optimize the mesh size for a better cluster cell gathering. We use the trajectory function to trace back the momentum of the input single charged particle. The results between the input and output values are consistent.

Keyword: KEK, Bell-II, Central Drift Chamber(CDC), 2-D Track Finding, Hough Transform.

## 誌謝詞

猛然回首碩士生活已經到達了尾聲，從一開始的懵懵懂懂的大學生，到現在已經要以碩士生的身份畢業了。在碩士生活中，很開心能夠加入了由張敏娟教授所帶領的高能研究室。在實驗室中每個成員，從學長:智嘉、昆嶸、建佑，同屆的彥錚，學弟:威廷、彥甫、新博，以及大學部的逸哲、柏增、宇珣，每位都是一起同甘共苦的夥伴們。能在此完成此篇論文，非常感謝老闆、王名儒老師與王正祥老師以及在日本KEK的Iwasaki-san耐心及細心的指導，還有在台大的學長姐們的幫忙，以及在這一路上來扶持著我的每一位夥伴、朋友們(小林哥、小東、俊傑、軒宇、K哥、趙哥、小鬼、勇哥、彬彬、崑銘、文俊、阿政、大木...)。最後要感謝的是我的父母，感謝他們的培育與支持，讓我繼續往下走的動力，才能有今日的我。感謝大家的支持，謝謝!!



# Contents

<b>1</b>	<b>Motivation</b>	<b>1</b>
<b>2</b>	<b>Current B-Factory</b>	<b>5</b>
2.1	KEKB Accelerator . . . . .	5
2.2	Belle Detector . . . . .	8
2.2.1	Beam Pipe . . . . .	10
2.2.2	Silicon Vertex Detector (SVD) . . . . .	12
2.2.3	Central Drift Chamber (CDC) . . . . .	14
2.2.4	Aerogel Cherenkov Counter System (ACC) . . . . .	17
2.2.5	Time-of-Flight Counters (TOF) . . . . .	19
2.2.6	Electromagnetic Calorimetry (ECL) . . . . .	22
2.2.7	$K_L$ and Muon Detection System (KLM) . . . . .	24
2.2.8	Extreme Forward Calorimeter (EFC) . . . . .	25
<b>3</b>	<b>Upgrade B-Factory</b>	<b>27</b>
3.1	SuperKEKB Accelerator . . . . .	27
3.2	Belle-II Detector . . . . .	32

<b>4 Upgrade CDC and CDC Trigger System</b>	<b>36</b>
4.1 Overview . . . . .	36
4.2 Structure . . . . .	39
4.3 Trigger System at Belle-II . . . . .	43
4.4 CDC Trigger System at Belle-II . . . . .	46
4.4.1 CDC Trigger Front-end at Belle-II . . . . .	47
4.4.2 Track Segment Finder in CDC at Belle-II . . . . .	50
4.4.3 2-D Track Finding and 3-D Trigger in CDC at Belle-II	53
<b>5 2-D Track Finding Algorithm and Hough Transformation</b>	<b>55</b>
5.1 2-D Track Finding Algorithm . . . . .	55
5.2 Hough Transformation . . . . .	56
<b>6 2-D Track Finding Simulation</b>	<b>61</b>
6.1 Types of Clusters . . . . .	61
6.2 Mesh Size Optimization . . . . .	71
6.3 Track Reconstruction . . . . .	74
6.4 Some Testing . . . . .	77
6.4.1 Some Calculations Related to Physics Laws . . . . .	77
6.4.2 Different Particle vs. Track Radius . . . . .	79
6.4.3 Different Momentum vs. Track Radius . . . . .	85
6.5 Mesh Size Optimization II . . . . .	95
<b>7 Summary</b>	<b>101</b>

# List of Figures

1.1	The related issues written in this chapter. . . . .	1
1.2	The Luminosity related issues. . . . .	2
1.3	The integrated luminosity record of the two B-factory. The blue line stands for Belle, and the green line for BaBar. . . . .	3
1.4	The KEKB and Belle-II Upgrade scheme. . . . .	4
1.5	The upgrade schedule. On the top is for integrated luminosity and on the bottom is for peak luminosity. . . . .	4
2.1	The related issues written in this chapter. . . . .	5
2.2	The KEKB related issues in this section. . . . .	5
2.3	The bird-view picture of KEK . . . . .	7
2.4	The simple operation of KEKB . . . . .	7
2.5	The idea of the $\pm 11$ mili rads colliding angle . . . . .	7
2.6	The Belle related issues in this section. . . . .	8
2.7	The Belle detector is illustrated in the overall view. . . . .	9
2.8	The Belle detector is illustrated in the side view. . . . .	10
2.9	The Beam pipe related issues in this section. . . . .	10

2.10	The cross section of the beryllium beam pipe at the interaction point.	11
2.11	The arrangement of the beam pipe and horizontal masks.	12
2.12	The SVD related issues in this section.	12
2.13	The configuration of SVD1.	13
2.14	The CDC related issues in this section.	14
2.15	Overview of CDC structure.	15
2.16	The cell structure and cathode sector configuration of CDC.	16
2.17	Mean of $dE/dx$ vs. momentum observed in collision data.	16
2.18	The ACC related issues in this section.	17
2.19	The arrangement of ACC at the central part of the Belle detector.	18
2.20	Schematic drawing of a typical ACC counter module: (a) barrel and (b) end-cap.	19
2.21	The TOF related issues in this section.	19
2.22	Mass distribution for particle momentum below $1.2 \text{ GeV}/c$ .	21
2.23	The size of a TOF/TSC module.	21
2.24	The ECL related issues in this section.	22
2.25	The ECL overall configuration.	23
2.26	The KLM related issues.	24
2.27	The configuration of RPC in barrel (left) and end-cap (right).	25
2.28	The EFC related issues.	25
2.29	The overall view of the forward and backward EFC.	26

2.30	The side view of forward EFC. . . . .	26
3.1	The related issues written in this chapter. . . . .	27
3.2	The SuperKEKB related issues in this section. . . . .	27
3.3	Schematic view of the beam collision in the Nano-Beam technique. . . . .	28
3.4	Schedules for injector upgrade and damping ring(upper) and Main Ring(lower). . . . .	31
3.5	The Belle-II related issues in this section. . . . .	32
3.6	The geometry difference between Belle-II (top) and Belle detector (bottom). . . . .	33
4.1	The related issues written in this chapter. . . . .	36
4.2	The upgrade CDC in Belle-II related issues in this section. . . . .	37
4.3	The Belle-II CDC Structure related issues in this section. . . . .	39
4.4	A schematic plot of Belle-II CDC side view. . . . .	40
4.5	Wire configuration of the Belle and Belle-II. . . . .	41
4.6	The Belle-II trigger system related issues in this section. . . . .	43
4.7	The schematic overview of the trigger system. The output from the five sub-trigger system are sent to the Global Decision Logic (GDL). The red lines are new added to the trigger system. . . . .	45
4.8	The CDC trigger system related issues in this section. . . . .	46
4.9	The logical flow of CDC trigger system. . . . .	47

4.10	The CDC Trigger front-end related issues in this section. . . . .	47
4.11	Hardware configuration of the CDC trigger system. . . . .	49
4.12	The Track Segment Finder (TSF) related issues in this section. .	50
4.13	The geometric shape of a track segment(TS). Each square corresponds to a wire cell. . . . .	51
4.14	Table of the sense wire, super-layers and TSs relation . . . . .	52
4.15	The 2-D Track Finding and 3-D trigger related issues in this section. . . . .	53
5.1	The 2-D Track finding algorithm and Hough Transformation related issues in this chapter. . . . .	55
5.2	The Hough transformation related issues in this section. . . . .	56
5.3	Schematic view of the right handed and left handed circles in the CDC x-y plane. . . . .	57
5.4	Schematic view of Hough plane. (a) left handed side is plus plane. (b) right handed side is minus plane. . . . .	59
5.5	In Hough plus plane, there are 4 arcs and they all pass through a point. A track function can be formed in this case. In Hough minus plane, there are 4 arcs in parallel. That means no track function can be formed. . . . .	60
5.6	The cross point $r_0$ and $\phi_0$ are the solution of the track function in the CDC x-y plane. . . . .	60
6.1	The related issues written in this chapter. . . . .	61

6.2	The Cluster type study related issues in this section. . . . .	62
6.3	A single $\pi^+$ passes through the CDC chamber. The green tracking points are the TS hits in each axial super-layers. . .	63
6.4	An example of our Hough transformation. . . . .	63
6.5	Only one peak region in Hough plane. . . . .	64
6.6	More than one peak region in Hough plane. . . . .	64
6.7	Schematic of the case 1, a perfect case. There is only one red block in the Hough plane. The peak position is the center of the only red block. . . . .	65
6.8	Left plot is the schematic of the case 2, a good case. Right-up is the corresponding simulation result in the CDC x-y plane. Right-bottom plot is the case in the Hough plus plane. . . .	66
6.9	Left plot is the schematic of the case 3, a good case. Right-up is the corresponding simulation result in the CDC x-y plane. Right-bottom plot is the case in the Hough plus plane. . . .	67
6.10	Two kinds of schematic of the case 4, bad cases. . . . .	68
6.11	Two kinds of case 4 plots, bad cases. Top plots are the corresponding simulation results in the CDC x-y plane. Bottom plots are the cases in the Hough plus plane. . . . .	69
6.12	Left plot is the schematic of the case 5, a bad case. Right-up is the corresponding simulation result in the CDC x-y plane. Right-bottom plot is the case in the Hough plus plane. . . .	70

6.13	Two kinds of the simulation result in the CDC x-y plane of the case 6, bad cases. . . . .	71
6.14	The Mesh size optimization related issues in this section. . .	71
6.15	The track reconstruction related issues in this section. . . .	74
6.16	Left plot: the red blocks in Hough plane are all connected with each other. Right plot: The peak position of $(\log r, \phi)$ in the Hough plane translate to the center of the track circle, $(C_x, C_y)$ in the CDC $x - y$ plane. . . . .	76
6.17	Some calculations related issues in this section. . . . .	77
6.18	The related issues written in this section. . . . .	79
6.19	The track radius obtained from good cases, $P$ sample. . . .	81
6.20	The track radius obtained from good cases, $\pi^+$ sample. . . .	82
6.21	The track radius obtained from good cases, $e^-$ sample. . . .	83
6.22	The related issues written in this section. . . . .	85
6.23	The track radius obtaining from good cases( $0.4 \text{ GeV}/c$ ). . .	87
6.24	The track radius obtaining from good cases( $0.5 \text{ GeV}/c$ ). . .	88
6.25	The track radius obtaining from good cases( $0.6 \text{ GeV}/c$ ). . .	89
6.26	The track radius obtaining from good cases( $0.7 \text{ GeV}/c$ ). . .	90
6.27	The track radius obtaining from good cases( $0.8 \text{ GeV}/c$ ). . .	91
6.28	The track radius obtaining from good cases( $0.9 \text{ GeV}/c$ ). . .	92
6.29	The track radius obtaining from good cases( $1.0 \text{ GeV}/c$ ). . .	93
6.30	The relationship between averaged radius and momentum. . .	94
6.31	The Mesh size optimization II issues in this section. . . . .	95

7.1	The summary related issues in this section. . . . .	101
2	The related issues written in this Appendix A. . . . .	103
3	The related issues written in this Appendix B. . . . .	109
4	The related issues written in this Appendix C. . . . .	112



# List of Tables

2.1	The geometric parameters of ECL . . . . .	23
3.1	Fundamental parameters of SuperKEKB and present KEKB	29
3.2	Machine parameters of SuperKEKB. Values in parentheses denote parameters at zero beam current . . . . .	30
4.1	Main parameter of the CDC Belle and upgraded Belle-II . .	37
4.2	Configuration of the Belle-II CDC sense wires. . . . .	41
4.3	Main parameter of the CDC Belle and Belle-II. . . . .	42
6.1	We separate the 100 events into six cases, in the divided mesh size of ( $\phi$ 350, $\log r$ 100). . . . .	72
6.2	We remove the contribution from case 6 and calculate the percentage of good cases and bad cases. The percentage of good cases is 78% and bad cases is 22%. The divided mesh size is ( $\phi$ 350, $\log r$ 100). . . . .	73
6.3	The ratio of good and bad cases in different divided mesh sizes. The best mesh size should be divided into ( $\phi$ 200, $\log r$ 50). . . . .	74

6.4	A summary of the environment settings in this section. . . . .	80
6.5	The number of events in each cases, $P$ sample. . . . .	81
6.6	The number of events in each cases, $\pi^+$ sample. . . . .	82
6.7	The number of events in each cases, $e^-$ sample. . . . .	83
6.8	The summary of the averaged track radius using $P$ , $\pi^+$ , and $e^-$ in the same momentum. The expected radius is 200 cm. The results are very close to the expected result. . . . .	84
6.9	The Momentum and the expected Radius. . . . .	86
6.10	A summary of the environment settings in this section. . . . .	86
6.11	The number of events in each cases( $0.4 \text{ GeV}/c$ ). . . . .	87
6.12	The number of events in each cases( $0.5 \text{ GeV}/c$ ). . . . .	88
6.13	The number of events in each cases( $0.6 \text{ GeV}/c$ ). . . . .	89
6.14	The number of events in each cases( $0.7 \text{ GeV}/c$ ). . . . .	90
6.15	The number of events in each cases( $0.8 \text{ GeV}/c$ ). . . . .	91
6.16	The number of events in each cases( $0.9 \text{ GeV}/c$ ). . . . .	92
6.17	The number of events in each cases( $1.0 \text{ GeV}/c$ ). . . . .	93
6.18	Summary of the average radius in different momentum range. .	94
6.19	The values of expected momentum, averaged radius and the trace back momentum from the averaged radius. . . . .	95
6.20	The simulation environment settings for mesh size optimization- II. . . . .	96

6.21	Divided mesh size ( $\phi$ 96, $\log r$ 96). Left side is the number of events and the ratio of good and bad cases. Right side is the averaged radius from good cases. . . . .	97
6.22	Divided mesh size ( $\phi$ 200, $\log r$ 50). Left side is the number of events and the ratio of good and bad cases. Right side is the averaged radius from good cases. . . . .	98
6.23	Divided mesh size ( $\phi$ 200, $\log r$ 100). Left side is the number of events and the ratio of good and bad cases. Right side is the averaged radius from good cases. . . . .	99
6.24	Summary of the previous divided mesh size results. . . . .	100
1	( $\phi$ 50, $\log r$ 50). . . . .	104
2	( $\phi$ 50, $\log r$ 100). . . . .	104
3	( $\phi$ 50, $\log r$ 200). . . . .	104
4	( $\phi$ 100, $\log r$ 50). . . . .	105
5	( $\phi$ 100, $\log r$ 100). . . . .	105
6	( $\phi$ 100, $\log r$ 200). . . . .	105
7	( $\phi$ 200, $\log r$ 50). . . . .	106
8	( $\phi$ 200, $\log r$ 100). . . . .	106
9	( $\phi$ 200, $\log r$ 200). . . . .	106
10	( $\phi$ 300, $\log r$ 50). . . . .	107
11	( $\phi$ 300, $\log r$ 100). . . . .	107
12	( $\phi$ 300, $\log r$ 200). . . . .	107

13	$(\phi \text{ 400}, \log r \text{ 50})$ .	108
14	$(\phi \text{ 400}, \log r \text{ 100})$ .	108
15	$(\phi \text{ 400}, \log r \text{ 200})$ .	108
16	Proton	110
17	$\pi$ meson	110
18	Electron	111
19	$0.4 \text{ GeV}/c$	112
20	$0.5 \text{ GeV}/c$	113
21	$0.6 \text{ GeV}/c$	113
22	$0.7 \text{ GeV}/c$	113
23	$0.8 \text{ GeV}/c$	114
24	$0.9 \text{ GeV}/c$	114
25	$1.0 \text{ GeV}/c$	114



# Chapter 1

## Motivation

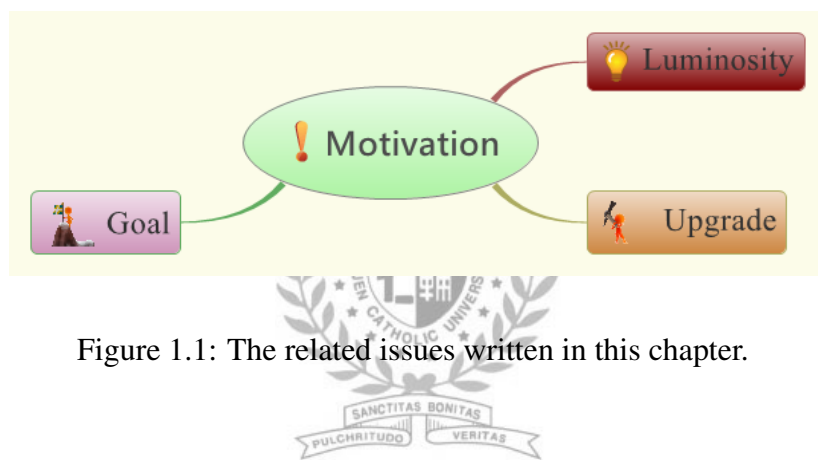


Figure 1.1: The related issues written in this chapter.

In scattering theory and accelerator physics, luminosity is the number of particles per unit area per unit time times the opacity of the target, usually expressed in either the cgs units  $cm^{-2}s^{-1}$  or  $b^{-1}s^{-1}$ . The integrated luminosity is the integral of the luminosity with respect to time. The luminosity is an important value to characterize the performance of an accelerator. The following elementary relations for luminosity hold:

$$L = \rho v \quad (1.1)$$

$$\frac{dN}{dt} = L\sigma \quad (1.2)$$

$$N = \sigma \int L dt \quad (1.3)$$

$$\frac{d\sigma}{d\Omega} = \frac{1}{L} \frac{d^2 N}{d\Omega dt} \quad (1.4)$$

where  $L$  is the peak luminosity.  $\int L dt$  is the integrated luminosity.  $N$  is the number of interactions.  $\rho$  is the number density of a particle beam.  $d\Omega$  is the differential solid angle.  $\frac{d\sigma}{d\Omega}$  is the differential cross section.[1]

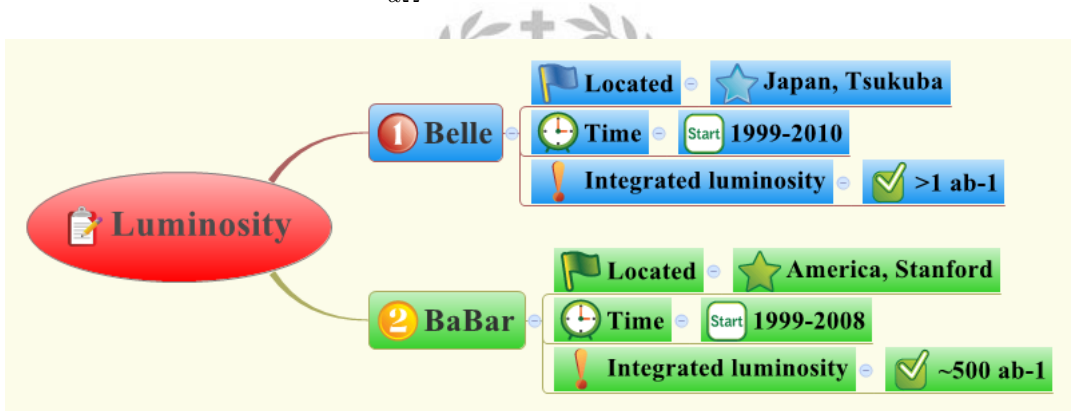


Figure 1.2: The Luminosity related issues.

The key words in this section are connected and shown in the Fig. ???. In Fig. 1.3, it displayed the integrated luminosity reached by Belle and BaBar detectors in the past 11 years. Belle and BaBar are the two collaboration for B physics search since 1999.

Belle is located at the Japan Tsukuba. It was operated since 1999 to 2010. The total accumulated data sample are more than  $1 ab^{-1}$ . This achievement

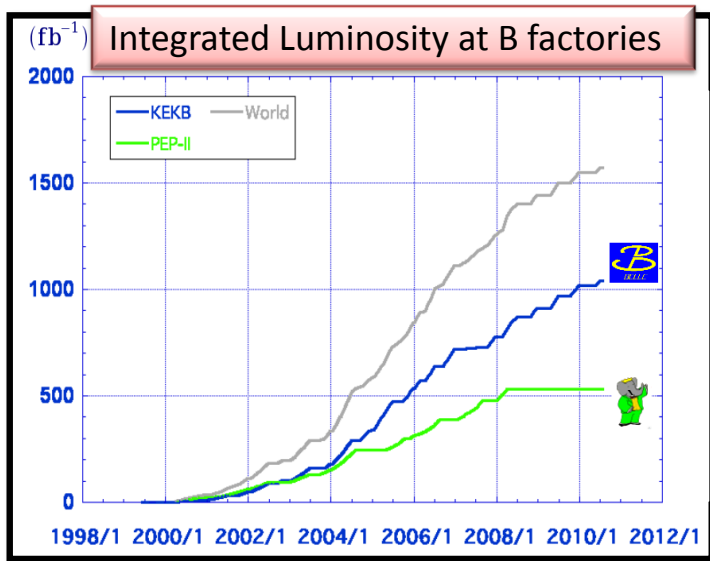


Figure 1.3: The integrated luminosity record of the two B-factory. The blue line stands for Belle, and the green line for BaBar.

reaches the original technical milestone.

BaBar is located at the America Stanford linear accelerator Center(SLAC) National Accelerator Laboratory. It was operated since 1999 to 2008. The integrated luminosity reached by BaBar is about  $500 \text{ fb}^{-1}$ .

Numerous results from Belle and BaBar have confirmed the good precision of the theoretical predictions from the Standard Model. During the Belle operation time, M.Kobayashi and T. Maskawa were awarded as the 2008 Nobel Prize winner in physics. Because their 3 generation theory and CP violation phase theory were confirmed by the two B-Factory.

Japan government funded 100 oku ¥(about 3.5 billion NT dollar) to support the upgrade plan for the accelerator and detector. For KEKB and Belle, they are shut down now. They are going to become superKEKB and Belle-II

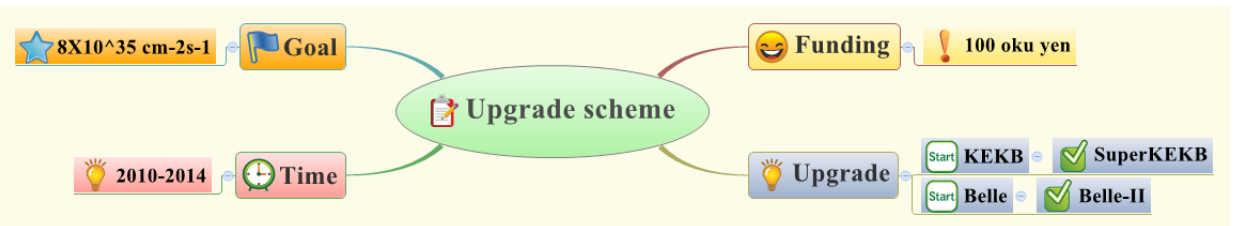


Figure 1.4: The KEKB and Belle-II Upgrade scheme.

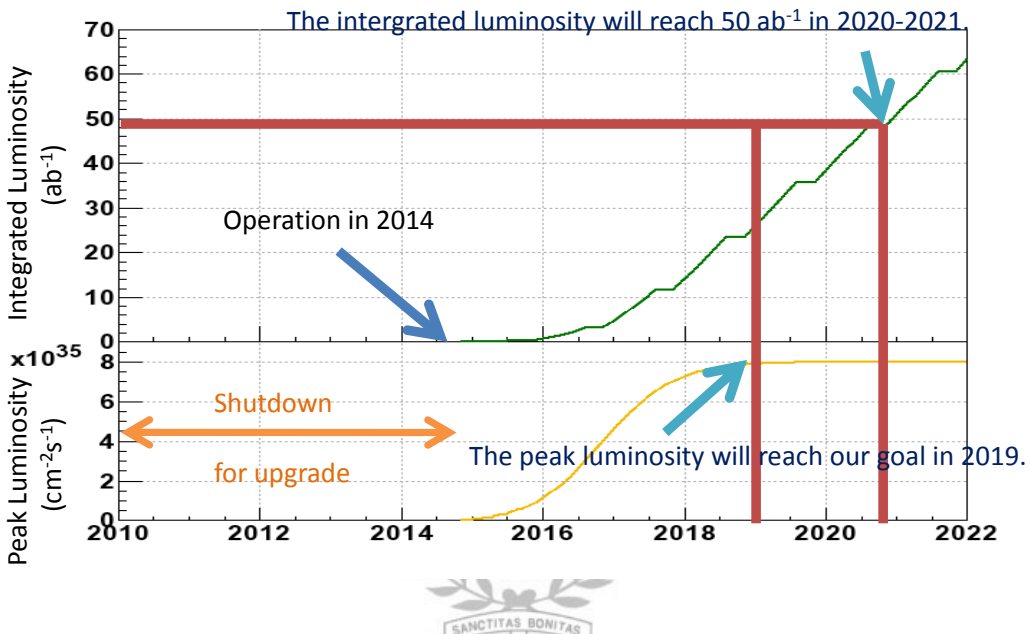


Figure 1.5: The upgrade schedule. On the top is for integrated luminosity and on the bottom is for peak luminosity.

soon. The goal for peak luminosity is  $8 \times 10^{35} \text{ cm}^{-2}\text{s}^{-1}$  after upgrade. The Fig. 1.5 shows the upgrade schedule. In 2010-2014, KEKB and Belle are shut down for upgrade. They are expected to start operation in 2014. On the top, it is for integrated luminosity, and on the bottom is for peak luminosity. We expect the goal luminosity can be reached in 2019. The integrated luminosity are expected to reach  $50 \text{ ab}^{-1}$  in 2020-2021.

# Chapter 2

## Current B-Factory

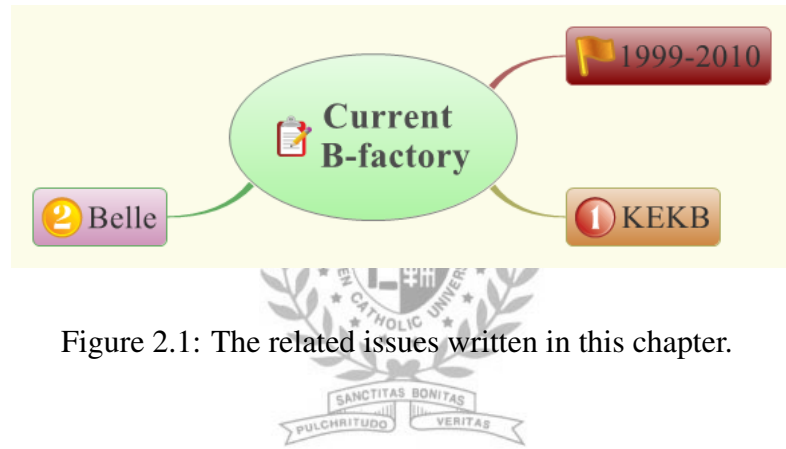


Figure 2.1: The related issues written in this chapter.

### 2.1 KEKB Accelerator

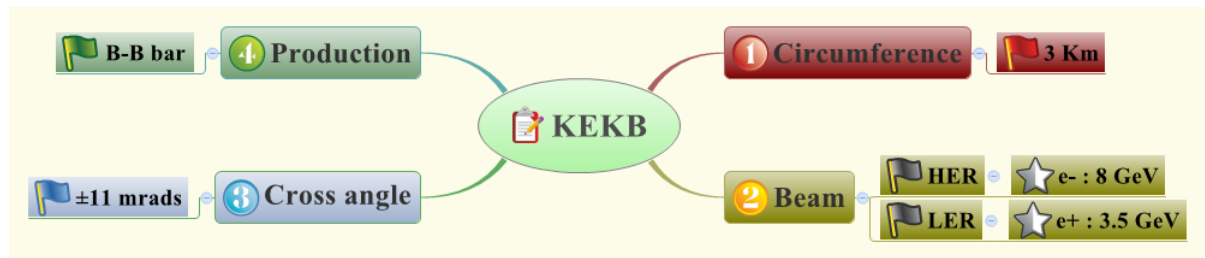


Figure 2.2: The KEKB related issues in this section.

The main idea of this section is described by the Fig. 2.2. A Japanese high-energy physics research organization named High Energy Accelerator

Research Organization (KEK). Inside KEK, there is a big accelerator and detector. Here I start from the accelerator part, the KEKB.

The KEKB is a circle accelerator with three kilo meters circumference. Two rings are built for the electron and positron beams to accelerate. The ring for electron beams is called the high-energy ring (HER) and the ring for positron beams is called low-energy ring (LER). The two beams collide each other inside Belle detector. The head-on colliding point, we call it the interaction point (IP). In the IP, the energy of electron beams is 8 GeV and the positron beams is 3.5 GeV. The head-on colliding angle of the two beams is about  $\pm 11$  mili rads. The center-of-mass energy of the colliding beams is 10.5 GeV, which is just above the  $\Upsilon(4S)$  resonance state. The main production of the  $\Upsilon(4S)$  is  $B\bar{B}$ . Therefore, the KEKB is usually called a B-Factory.

The bird-view picture of KEK is shown in Fig. 2.3. The simple operation of KEKB is illustrated in Fig. 2.4. The idea of the  $\pm 11$  mili rads colliding angle is shown in Fig. 2.5.



Figure 2.3: The bird-view picture of KEK

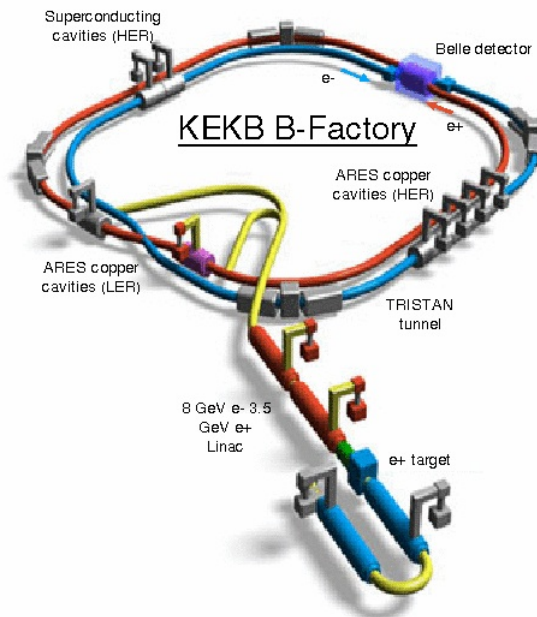


Figure 2.4: The simple operation of KEKB

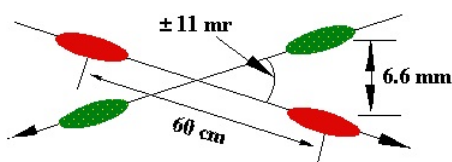


Figure 2.5: The idea of the  $\pm 11$  mili rads colliding angle

## 2.2 Belle Detector

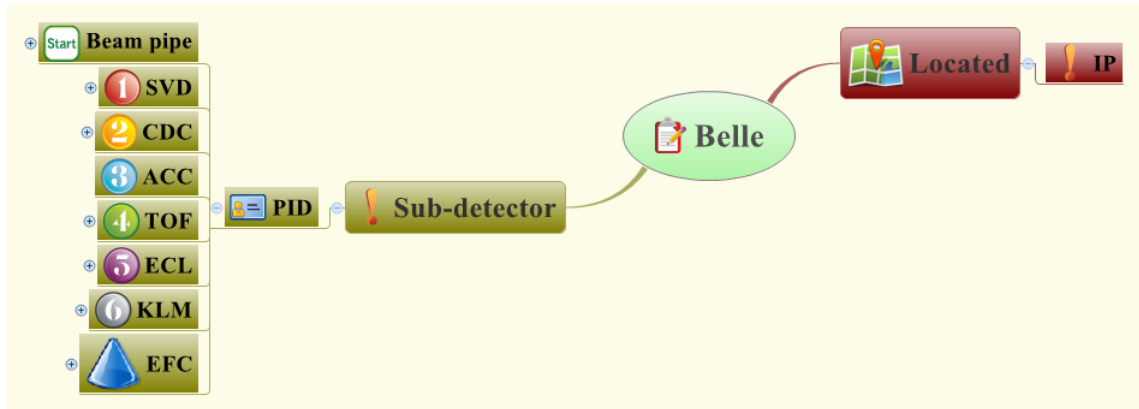


Figure 2.6: The Belle related issues in this section.

The Belle detector is designed for particle identification and event reconstruction. Inside Belle, there are several sub-detectors. The Fig. 2.6 shows the briefly contains in this section. From the inner to the outer, Belle sub-detectors are Silicon Vertex Detector (SVD), Central Drift Chamber (CDC), Aerogel Cherenkov Counters (ACC), Time-of-flight (TOF), Electromagnetic Calorimeter (ECL) and  $K_L$  and Muon Detector (KLM).

The decay vertices are mainly measured by the SVD. The tracking information is mainly reconstructed by the 50-layer CDC. To separate the pi and K particles by their Cherenkov light, ACC is the one. For the charged particles with momentum below 1.2 GeV/c, TOF can not only detect the flying time but also do the particle identification. For the neutral particles, ECL can detect their energy and reconstruct their decay position. For longer life time particle, say,  $\mu$  and  $K_L$ , KLM can detect their tracks and decay vertices. An extreme forward calorimeter (EFC) is placed at the small angle region of for-

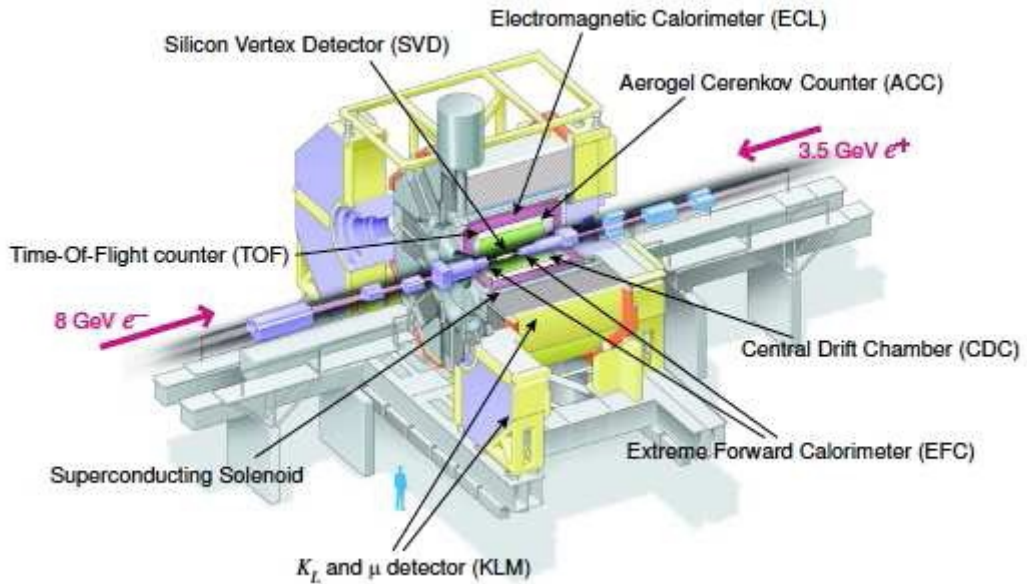


Figure 2.7: The Belle detector is illustrated in the overall view.

ward and backward beam direction. It can measure the on-line luminosity. The Belle detector is illustrated in the overall and side view in Fig. 2.7 and 2.8, respectively.

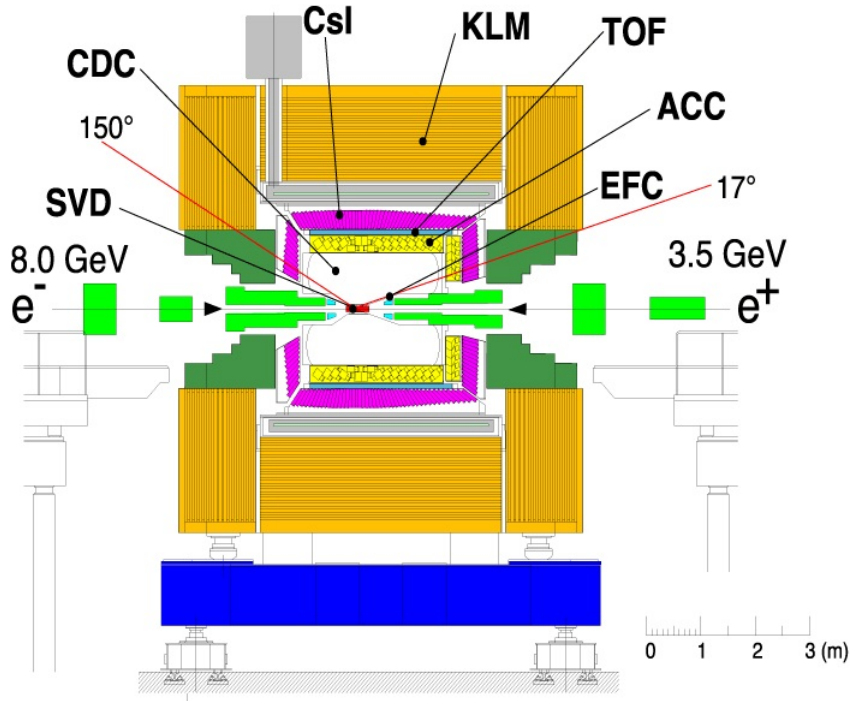
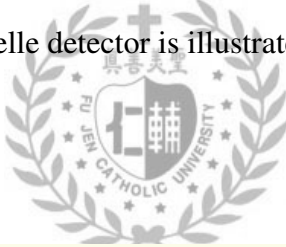


Figure 2.8: The Belle detector is illustrated in the side view.



### 2.2.1 Beam Pipe



Figure 2.9: The Beam pipe related issues in this section.

The main idea in this section is plotted in the Fig. 2.9.

The Beam pipe is located at the region where  $e^-$  and  $e^+$  collide and create a mount of particles of high luminosity. The precise measurement of B meson decay vertices is required. The Fig. 2.10 shows the cross section of

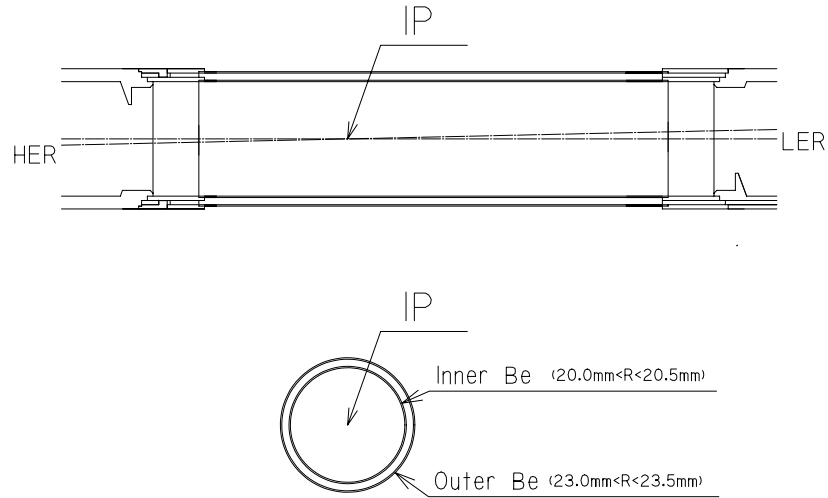


Figure 2.10: The cross section of the beryllium beam pipe at the interaction point.

the beryllium beam pipe. The central part of the beam pipe is a double-wall beryllium cylinder with inner diameter 40 mm and outer diameter 46 mm. A 2.5 mm gap between the two walls provides a space for helium gas cooling the beam system. The inner and outer walls are 0.5 mm thick. There are some masks in the outer part to cover particle background. The configuration is shown in Fig. 2.11.

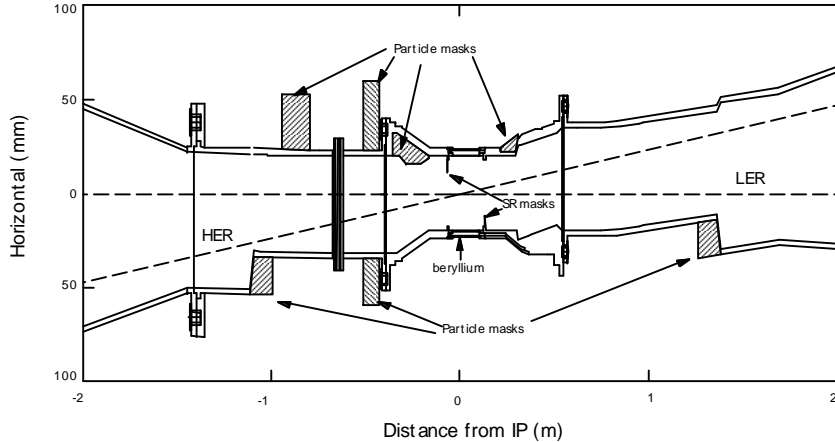


Figure 2.11: The arrangement of the beam pipe and horizontal masks.



## 2.2.2 Silicon Vertex Detector (SVD)

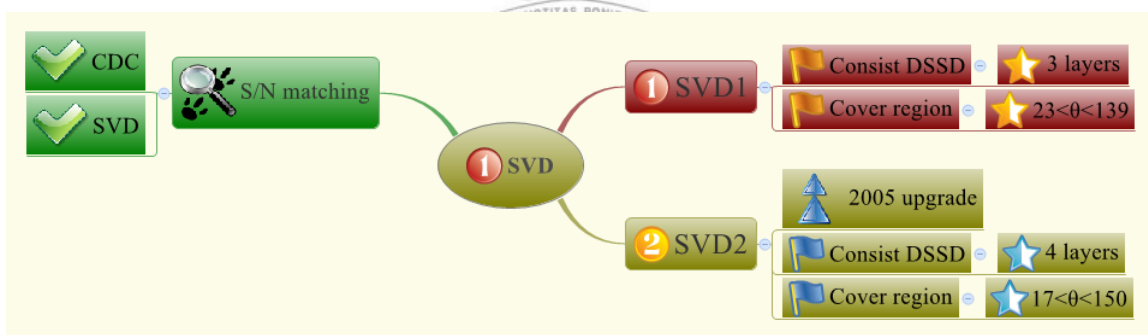


Figure 2.12: The SVD related issues in this section.

The main idea in this section is plotted in the Fig. 2.12. The decay vertices of B mesons are measured by Silicon vertex Detector (SVD). The SVD consists of 3 layers of double side strip detector (DSSD). There are 32 ladders DSSD in SVD, comprising 8, 10 and 14 ladders in the inner, middle and

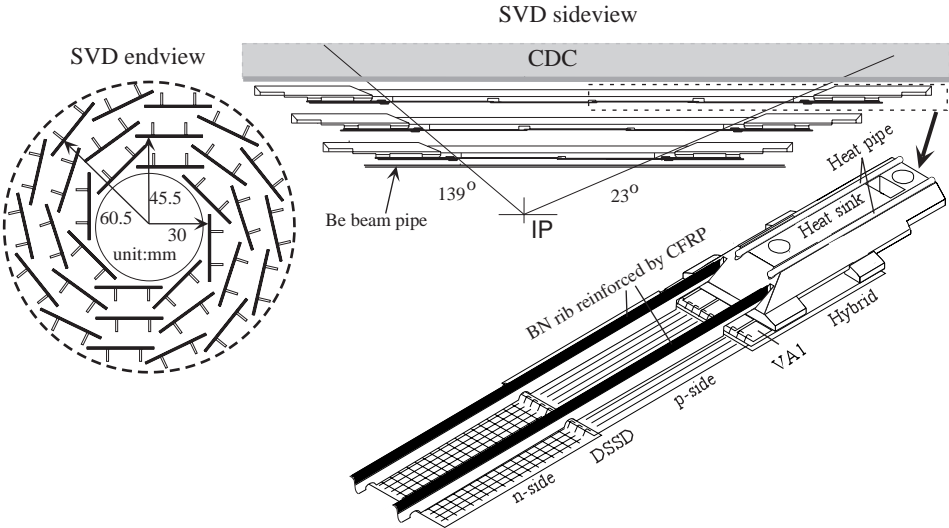


Figure 2.13: The configuration of SVD1.

outer layers. The SVD covers a solid angle  $23^\circ < \theta < 139^\circ$ , it about 86% of the full solid angle. Fig. 2.13 shows the configuration of the first version of SVD (SVD1). Each DSSD consists of 1280 sense strips and 640 readout pads on opposite sides. SVD strip with high yields and good signal-to-noise (S/N) ratios are needed to ensure the efficient matching CDC and SVD. The matching efficiency is defined as: a CDC track matched the SVD hits in at least 2 layers; the the  $r - \phi$  and  $r - z$  information are the same in at least 1 layer. The average matching efficiency is better than 98.7% after one year operation.

In 2005, the SVD detector is upgraded. The upgraded SVD detector is called SVD2. The main different issues in SVD2 are consisting 4 layers and covering wider solid angle  $17^\circ < \theta < 150^\circ$ . And, the first DSSD layer is closer to the beam pipe than SVD1. The vertex resolution is improved in this way.

### 2.2.3 Central Drift Chamber (CDC)

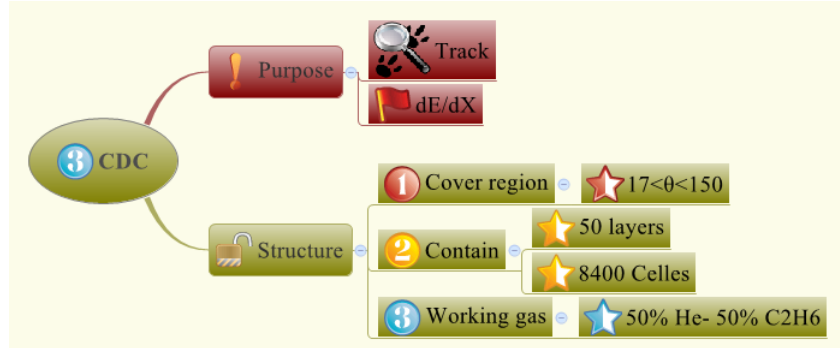


Figure 2.14: The CDC related issues in this section.

The main idea in this section is plotted in the Fig. 2.14.

The CDC detector is designed for the track reconstruction of the charged particles and to measure the  $dE/dx$ . The momentum resolution in CDC,  $\sigma_{p_t}/p_t \sim 0.5\% \sqrt{1 + p_t^2}$  ( $p_t$  in  $GeV/c$ ) is required to be  $p_t \geq 100 MeV$ .

The structure of CDC is shown in Fig. 2.15. It is asymmetric in the Z direction in order to provide an angular coverage in the polar angle region of  $17^\circ \leq \theta \leq 150^\circ$ . The chamber consists of 50 cylindrical layers. Each layer contains three and six either axial or small-angle-stereo layers. There are three cathode strip layers and total 8400 drift cells. The configuration of cell structure and cathode sector is shown in Fig. 2.16. Since the majority of the decay particles of B meson have momenta lower than  $1 GeV/c$ , so the use of a low-Z gas to minimize multiple scattering is important for improving the momentum resolution. The low-Z gases have a smaller photo-electric cross section than argon-based gases. Moreover, it reduces background from synchrotron radiation. A good  $dE/dx$  resolution can be provided by the large

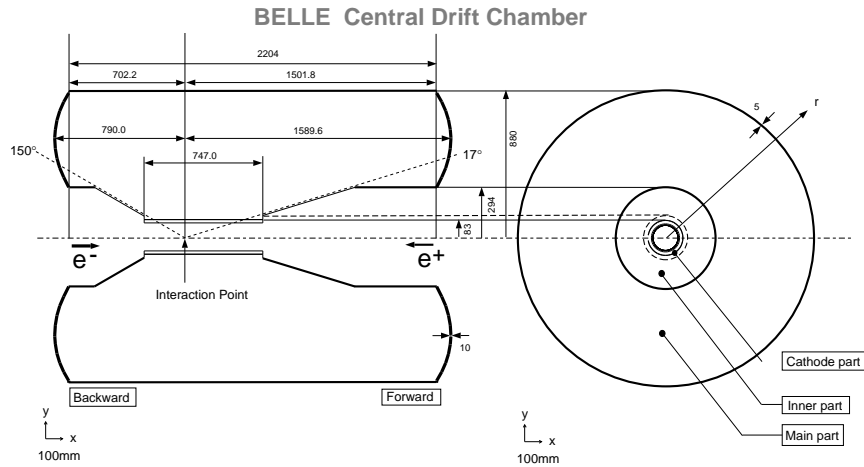


Figure 2.15: Overview of CDC structure.

ethane component. We choose a 50% helium-50% ethane mixture gas to fill the chamber. In Fig. 2.17, it shows the scatter plot of measured  $\langle dE/dx \rangle$  and particle momentum, together with the expected mean energy losses for different particle species.



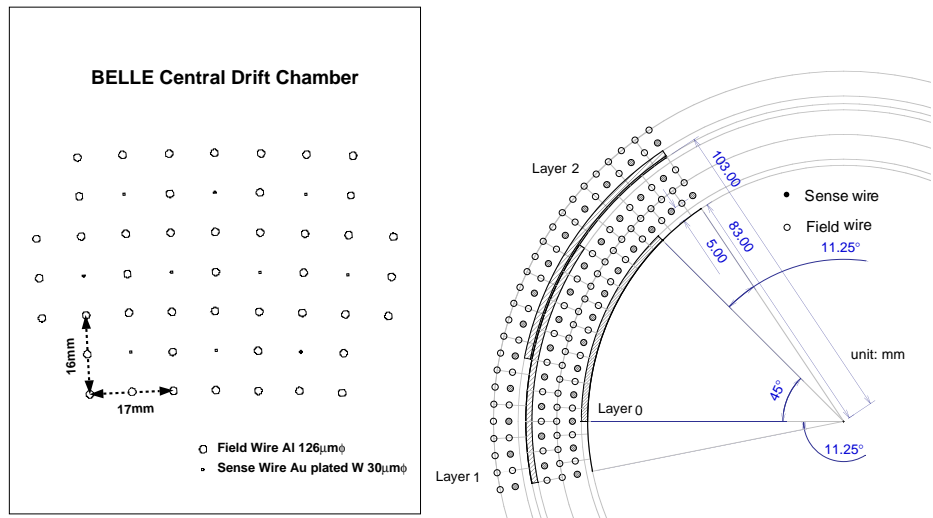


Figure 2.16: The cell structure and cathode sector configuration of CDC.

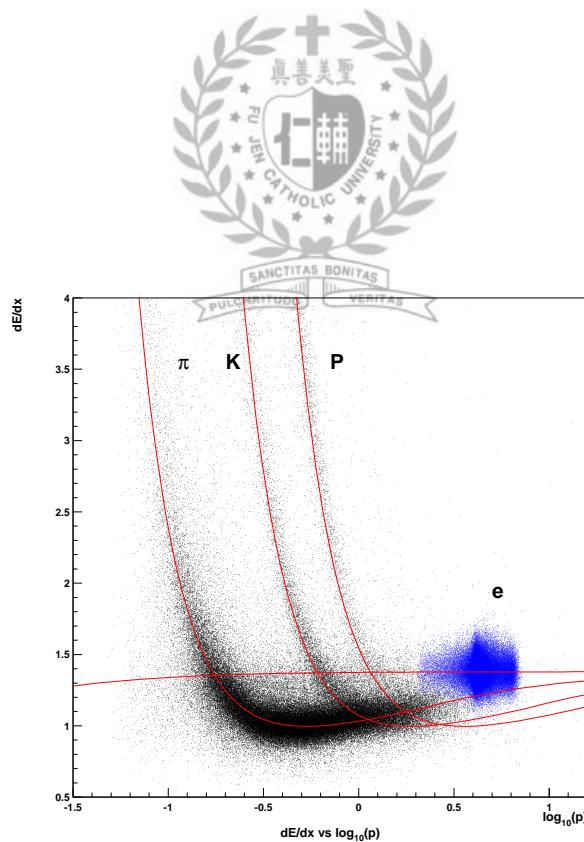


Figure 2.17: Mean of  $dE/dx$  vs. momentum observed in collision data.

## 2.2.4 Aerogel Cherenkov Counter System (ACC)

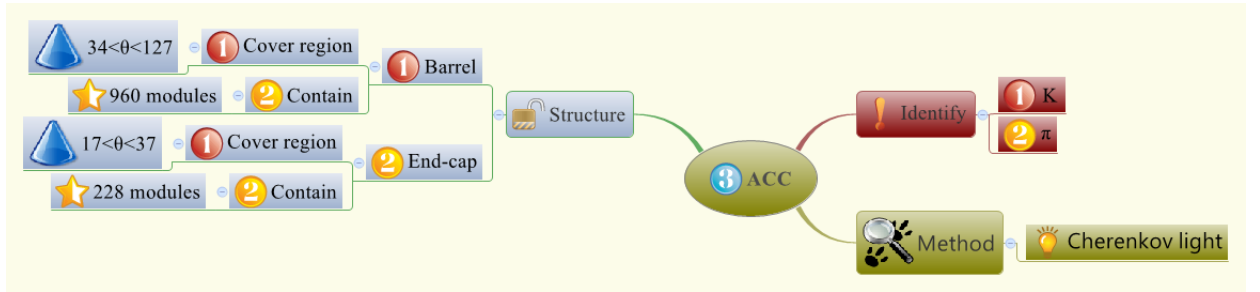


Figure 2.18: The ACC related issues in this section.

The main idea in this section is plotted in the Fig. 2.18.

The Cherenkov light is an electromagnetic radiation emitted when a charge particle passes through a dielectric medium at a speed exceed the velocity of light. The dielectric medium in ACC is aerogel. The refractive index of aerogel satisfies  $n > 1/\beta = \sqrt{1 + (m/p)^2}$ , where m and p are the mass and momentum of the particle. In the refractive index equation, it contains mass term. So this refractive index equation can be used for distinguishing particle species. The primary goal of ACC is to separate  $\pi$  and  $K$  particles, momentum range from  $1.2 \text{ GeV}/c$  up to  $4 \text{ GeV}/c$ . The arrangement of ACC is shown in Fig. 2.19. ACC can be separated into two parts: barrel and end-cap. The barrel part covers the region in polar angle from  $34^\circ$  to  $127^\circ$ . It also consists 960 counter modules segmented into 60 cells in the  $\phi$  direction. The end-cap part covers the region in polar angle from  $17^\circ$  to  $34^\circ$ . It also consists 228 modules arranged in 5 concentric layers. All the counters are arranged in a semi-tower geometry and pointing to the interaction point. The refractive

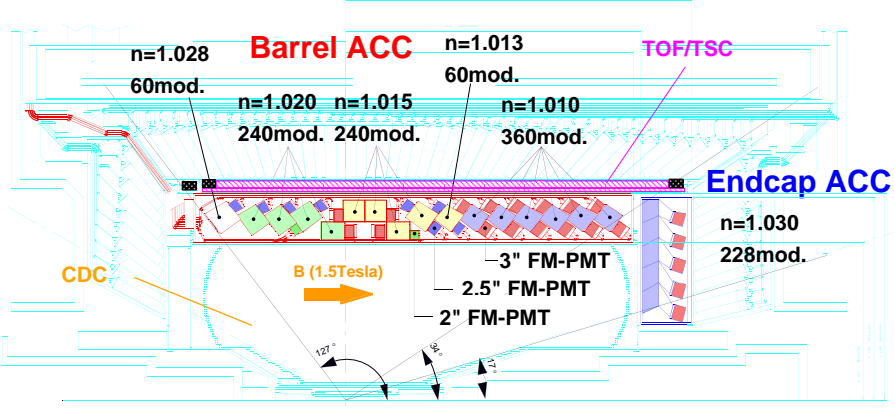


Figure 2.19: The arrangement of ACC at the central part of the Belle detector.

indices of aerogels are selected to be between 1.01 and 1.03, depending on their polar angle region. A typical single ACC module is shown in Fig. 2.20 (a) and (b) for the barrel and the end-cap, respectively.



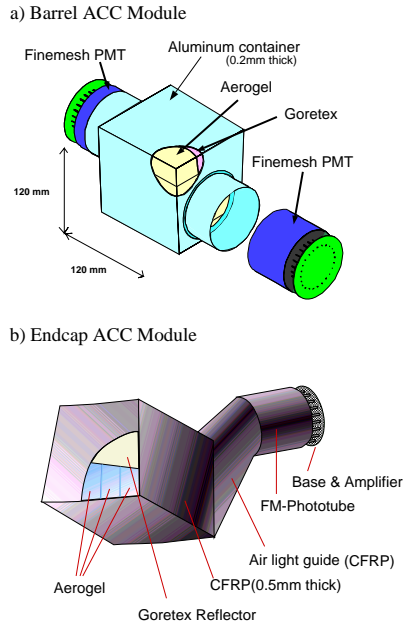


Figure 2.20: Schematic drawing of a typical ACC counter module: (a) barrel and (b) end-cap.



## 2.2.5 Time-of-Flight Counters (TOF)



Figure 2.21: The TOF related issues in this section.

The main idea in this section is plotted in the Fig. 2.21.

A time-of-flight (TOF) detector is made by several plastic scintillation counters. TOF is very powerful for particle identification. When a charged particle travels through the scintillating medium, the particle provides some energy to excite the atom and produce photon. By detecting these photons,

the time of flight can be measured. For a 1.2 m flight path, the TOF with 100 ps time resolution is effective. For those momenta below  $1.2 \text{ GeV}/c$  particles, 90% of them are produced from  $\Upsilon(4S)$  decays. For particle identification in TOF, we calculate the mass distribution for each track by using the following equation:

$$M_{track}^2 = \left(\frac{1}{\beta^2} - 1\right) = \left(\left(\frac{cT_{obs}^{twc}}{L_{path}}\right)^2 - 1\right)P^2$$

where  $P$  and  $L_{path}$  are momentum and path length of particle determined from the CDC track fit, respectively. Assuming the  $\mu$  mass, and  $T_{obs}^{twc}$  are time walk correction, we can get a precise observed time in this way. In the Fig. 2.22, it shows the mass distribution using TOF measurement. The plot aims for those momentum below  $1.2 \text{ GeV}/c$  particles.

The TOF consists of 128 TOF counters and 64 TSC (trigger scintillation counters). TOF covers the range from  $17^\circ$  to  $127^\circ$ . Two trapezoidal shaped TOF counters and one TSC counter construct one module, showing in Fig. 2.23. The 1.5 cm gap between the TOF counters and TSC counters is to isolate TOF from photon conversion backgrounds. The photon conversion backgrounds is taken from the coincidence between the TOF and TSC.

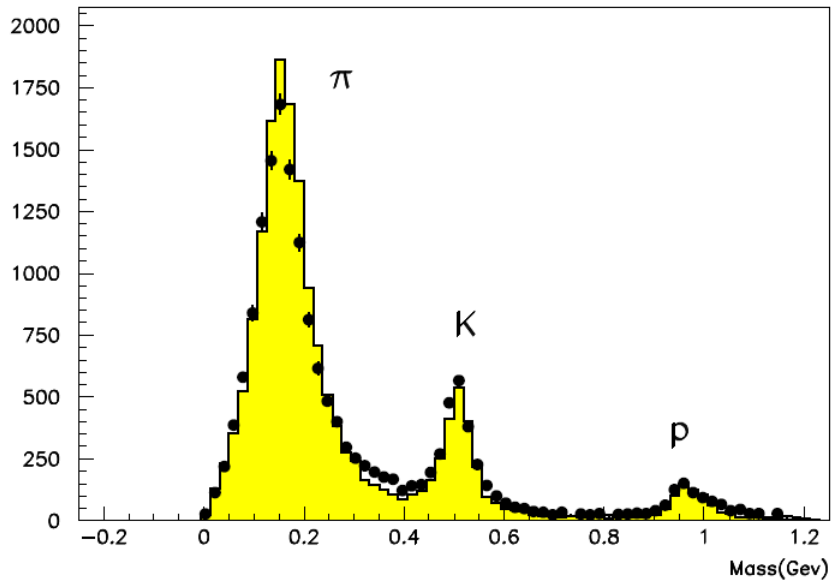


Figure 2.22: Mass distribution for particle momentum below  $1.2 \text{ GeV}/c$

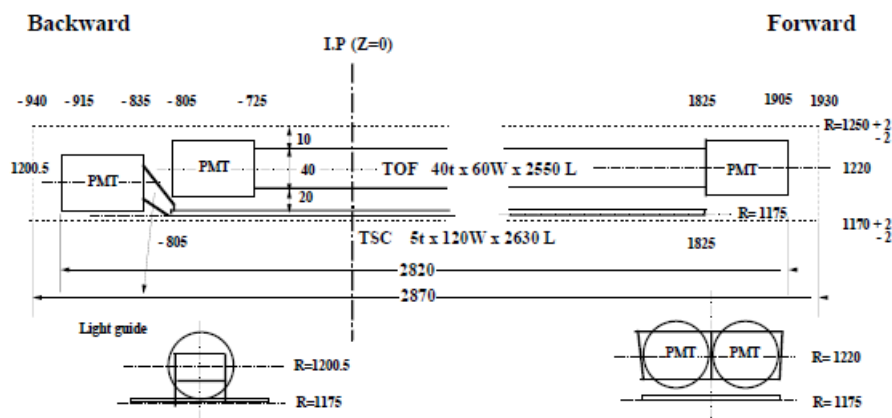


Figure 2.23: The size of a TOF/TSC module

## 2.2.6 Electromagnetic Calorimetry (ECL)

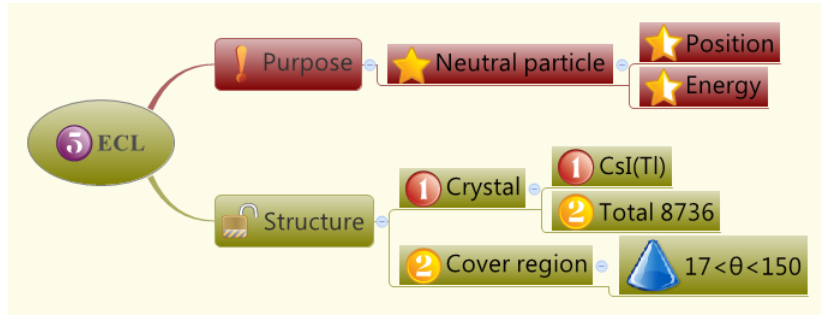


Figure 2.24: The ECL related issues in this section.

The main idea in this section is plotted in the Fig. 2.24.

The main purpose for ECL detector is to detect energy and position of photons. Meanwhile, ECL has to operate in high efficiency and good resolution conditions. Most of photons are the end-production of cascade B meson decays. So, a good performance in energy measurement below 500 MeV is important.

Fig. 2.25 shows the overall configuration of ECL detector. It is constructed by three parts: barrel, forward and backward end-cap. The size of CsI(Tl) crystals are 55 mm × 55 mm (front face) and 65 mm × 65 mm (rare face) for barrel. And the size of the end-cap parts, the crystals are in a range from 44.5 mm × 44.5 mm to 70.8 mm × 70.8 mm for the front face, and from 54 mm × 54 mm to 82 mm × 82 mm for rare face. Each crystal has a tower-like shape and is arranged to almost points to the IP with a small tilt angle of  $\sim 1.3^\circ$  in the  $\theta$  and  $\phi$  direction in barrel and angle of  $\sim 1.5^\circ$  and  $\sim 4^\circ$  in the  $\theta$  direction in the forward and backward end-cap, respectively.

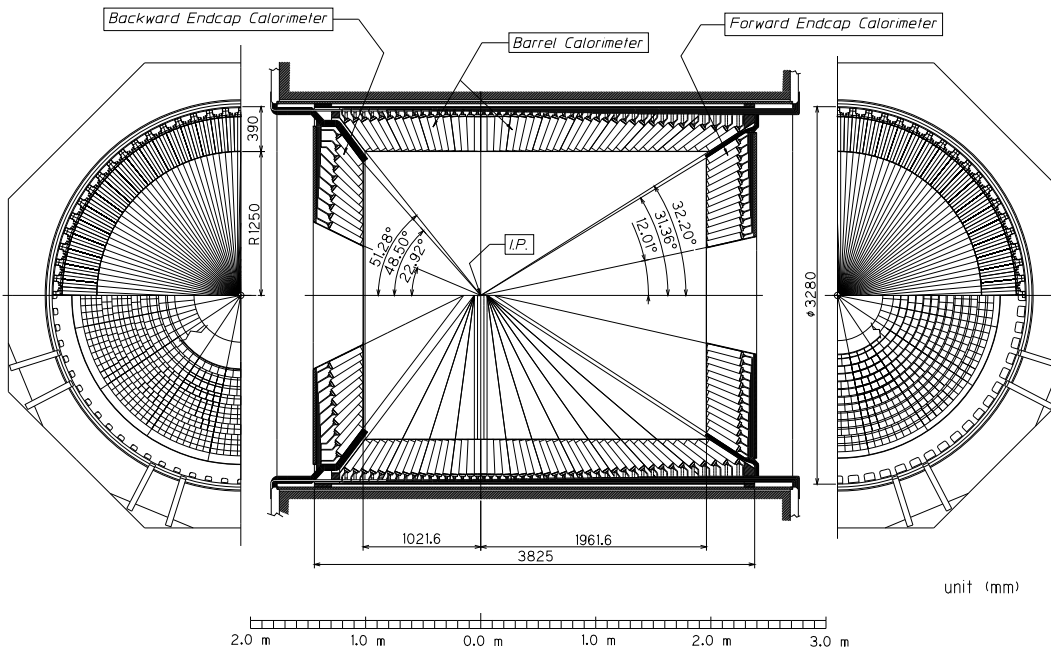


Figure 2.25: The ECL overall configuration.

The ECL detector contains 8736 CsI(Tl) counters and covers the range of polar angle region of  $17^\circ < \theta < 150^\circ$ . The geometric parameters of each region are shown in Table. 2.1.

Table 2.1: The geometric parameters of ECL.

Item	$\theta$ coverage	$\theta$ seg.	$\phi$ seg.	No. of crystals
Forward end-cap	$12.4^\circ - 31.4^\circ$	13	48 - 144	1152
Barrel	$32.2^\circ - 128.7^\circ$	46	144	6624
Backward end-cap	$130.7^\circ - 155.1^\circ$	10	64 - 144	960

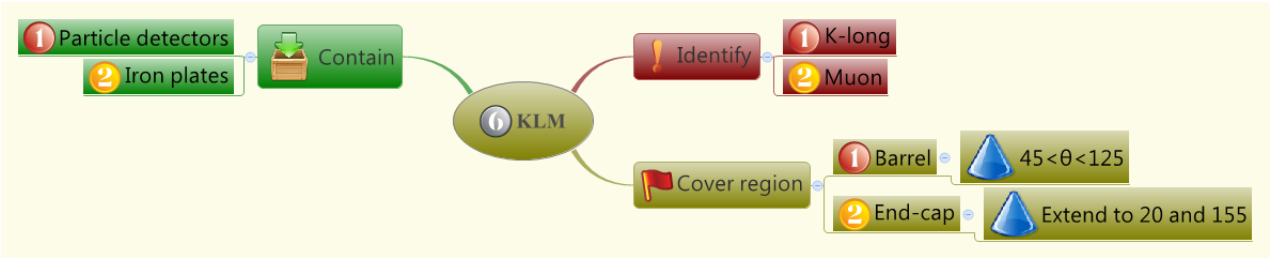


Figure 2.26: The KLM related issues.

### 2.2.7 $K_L$ and Muon Detection System (KLM)

The main idea in this section is plotted in the Fig. 2.26. The outermost sub-detector in Belle is KLM detector. It is designed to identify  $K_L^0$  and muon ( $\mu^\pm$ ) with momentum bigger than  $600 \text{ MeV}/c$ . KLM includes several layers of iron plates. In barrel, KLM covers angle range from  $45^\circ$  to  $125^\circ$ . In end-cap in the forward and backward, KLM extends the covering range from  $20^\circ$  to  $155^\circ$ . There are 15 (14) detector layers and 14 iron layers in the barrel (end-cap) region. The iron plates provide 3.9 interaction lengths. For  $K_L$ , additional 0.8 interaction lengths from ECL may help to detect it.

The charge particle detection is provided by glass-electrode resistive plate counters (RPCs). RPCs have two parallel plate electrodes with high bulk resistivity, they are separated by a gas-filled gap. One RPC super-layer consists of two RPC layers to provide  $\theta$  and  $\phi$  information. The configuration of the RPC is shown in Fig.2.27.

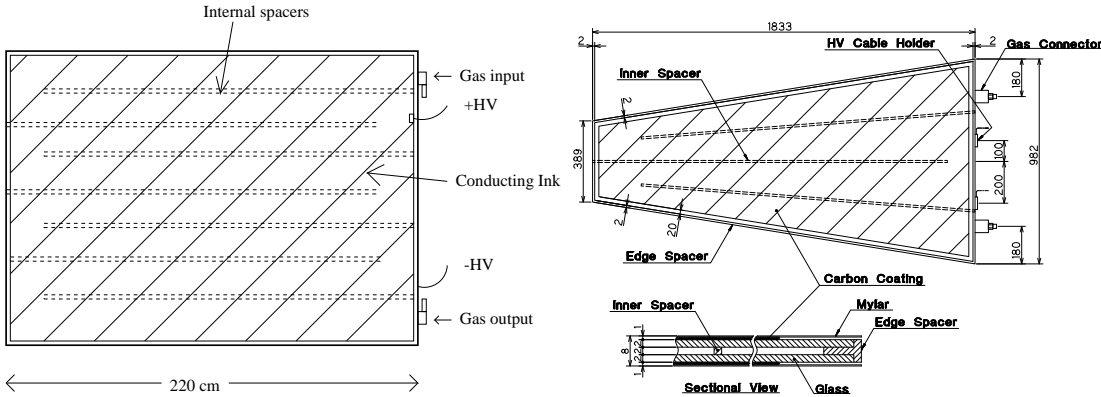
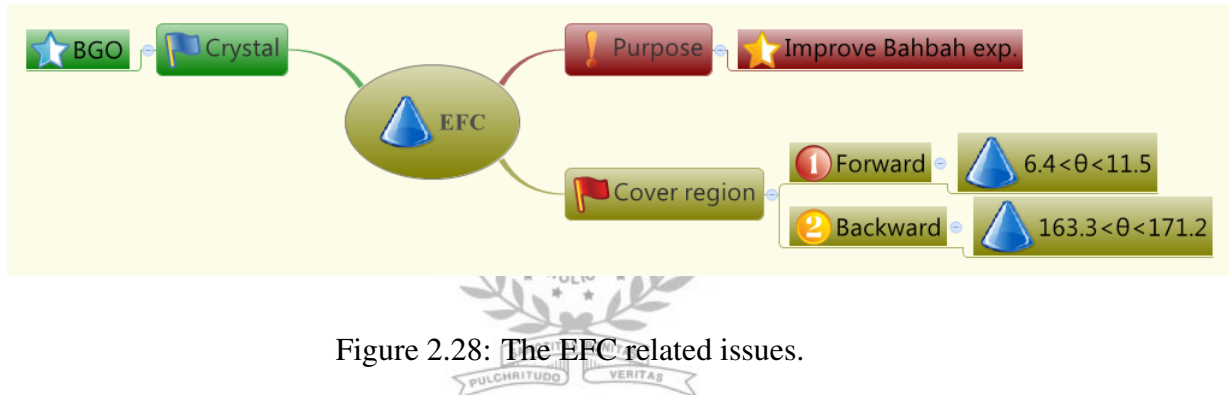


Figure 2.27: The configuration of RPC in barrel (left) and end-cap (right).

### 2.2.8 Extreme Forward Calorimeter (EFC)



The main idea in this section is plotted in the Fig. 2.28. The EFC detector is a further extending detector. The EFC covers the angular range from  $6.4^\circ$  to  $11.5^\circ$  in the forward direction and  $163.3^\circ$  to  $171.2^\circ$  in the backward. In order to improve the sensitivity to some physics processes, such as  $B \rightarrow \tau\nu$  or  $B \rightarrow \nu\nu$ . The EFC is located in the very high radiation area. So, the BGO crystal is selected to against the radiation hardness (bismuth Germanate,  $Bi_4Ge_3O_{12}$ ). The crystal arrangement is shown in Fig. 2.29. The crystals are shaped in trapezoid and the segmented into 32 in  $\phi$  and 5 in  $\theta$  for both ends. The schematic side view of the forward EFC is shown in 2.30.

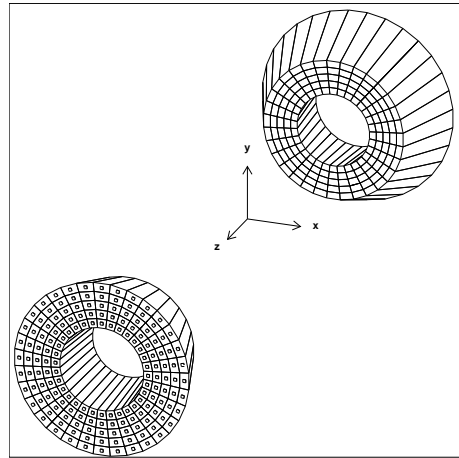
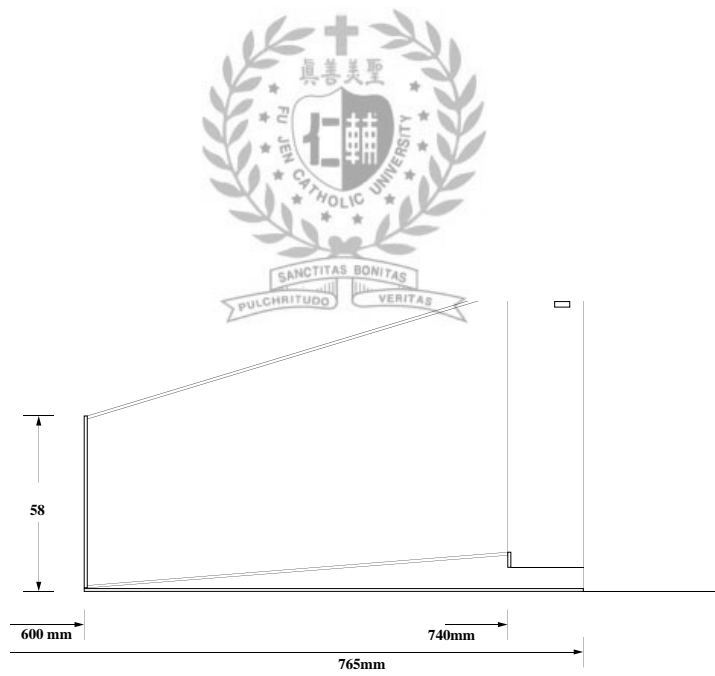


Figure 2.29: The overall view of the forward and backward EFC.



EFC Forward Side-View

Figure 2.30: The side view of forward EFC.

# Chapter 3

## Upgrade B-Factory

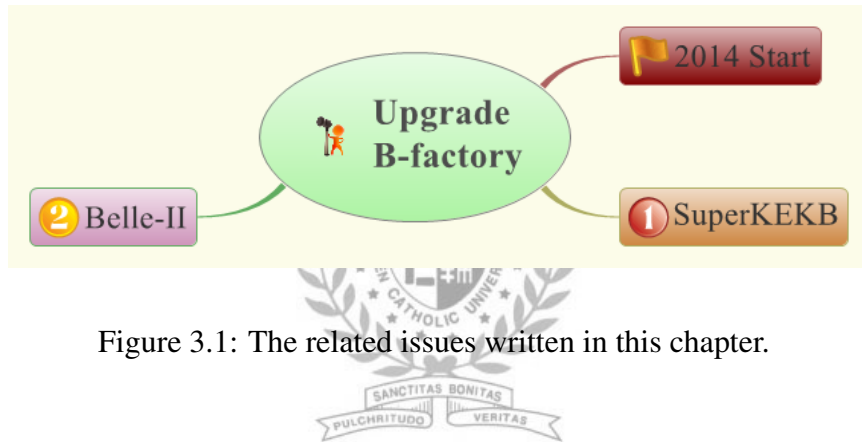


Figure 3.1: The related issues written in this chapter.

### 3.1 SuperKEKB Accelerator

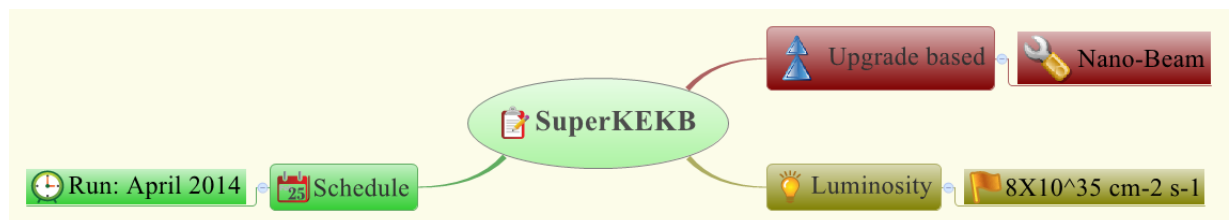


Figure 3.2: The SuperKEKB related issues in this section.

The main idea of this section is described by the Fig. 5.2. SuperKEKB will be the upgraded accelerator in KEK, Japan. It uses the same tunnel as

KEKB. The upgrade accelerator is based on the Nano-Beam technique. The luminosity goal of the SuperKEKB is  $8 \times 10^{35} \text{ cm}^{-2}\text{s}^{-1}$ . The schedule for operation is aimed at 2014.

## Machine Parameters of SuperKEKB

The Nano-Beam technique is to squeeze the vertical beta function( $\beta_y^*$ ) at the IP by minimizing the longitudinal size of the overlap region of the two beams at the IP. The Fig. 3.3 shows a schematic view of the beam collision in the Nano-Beam technique.

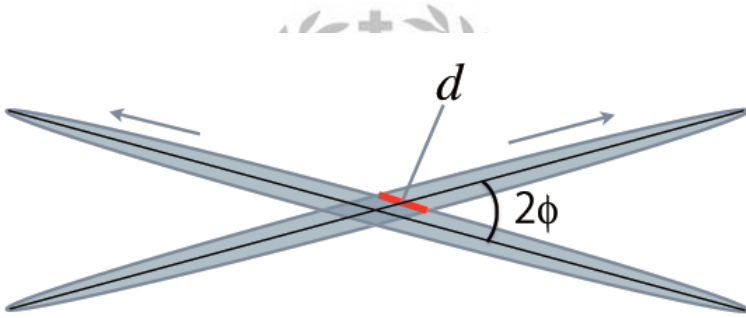


Figure 3.3: Schematic view of the beam collision in the Nano-Beam technique.

The luminosity of a collision is expressed by the following equation, assuming flat beams and equal horizontal and vertical beam sizes for two beams at the IP:

$$L = \frac{\gamma_{\pm}}{2er_e} \left( \frac{I_{\pm} \xi_{y\pm}}{\beta_{y\pm}^*} \right) \left( \frac{R_L}{R_{\xi y}} \right) \quad (3.1)$$

where  $\gamma$ ,  $e$  and  $r_e$  are the Lorentz factor, the elementary electric charge and the electron classical radius, respectively. The suffix  $\pm$  specifies the positron(+) or the electron(-). The parameters  $R_L$  and  $R_{\xi y}$  represent re-

Table 3.1: Fundamental parameters of SuperKEKB and present KEKB

	KEKB Achieved	SuperKEKB
Energy (GeV) (LER/HER)	3.5/8.0	4.0/7.0
$\xi_y$	0.129/0.09	0.09/0.088
$\beta_y^*(\text{mm})$	5.9/5.9	0.27/0.41
I(A)	1.64/1.19	3.6/2.62
Luminosity( $10^{34} \text{cm}^{-2}\text{s}^{-1}$ )	2.11	80

duction factors for the luminosity and the vertical beam-beam parameter. Since the ratio of these parameters are usually not far from the unity. Therefore, the luminosity is mainly determined by the three parameters: the total beam current(I), the vertical beam-beam parameter( $\xi_y$ ) and the vertical beta function( $\beta_y^*$ ) at the IP. Table 3.1 shows the choice of the mainly parameters, together with the present KEKB. The machine parameters of SuperKEKB including the three fundamental parameters are shown in Table 3.2.

## Schedule for the SuperKEKB Accelerator

A tentative schedule for the SuperKEKB construction is shown in Fig 3.4. The Injector upgrade and Damping Ring construction are shown in the upper part of the figure, and the Main Ring construction is shown in the lower part. The construction starts after the final run of the KEKB operation in June, 2010. The commissioning of SuperKEKB will begin in April 2014.

Table 3.2: Machine parameters of SuperKEKB. Values in parentheses denote parameters at zero beam current

		LER(e+)	HER(e-)	units
Beam Energy	E	4	7	GeV
Half Crossing Angle	$\phi$		41.5	mrad
Horizontal Emittance	$\varepsilon_x$	3.2(2.7)	2.4(2.3)	nm
Emittance ratio	$\varepsilon_y/\varepsilon_x$	0.4	0.35	%
Beta Function at the IP	$\beta_x^*/\beta_y^*$	32/0.27	25/0.41	mm
Horizontal Beam Size	$\sigma_x^*$	10.2(10.1)	7.75(7.58)	$\mu m$
Vertical Beam Size	$\sigma_y^*$	59	59	nm
Betatron tune	$\nu_x/\nu_y$	45.53/45.57	58.529/52.57	
Momentum Compaction	$\alpha_c$	$2.74 \times 10^{-4}$	$1.88 \times 10^{-4}$	
Energy Spread	$\sigma_\varepsilon$	$8.15(7.96) \times 10^{-4}$	$6.49(6.34) \times 10^{-4}$	
Beam Current	I	3.6	2.62	A
Number of Bunches/ring	$n_b$	2503		
Energy Loss/turn	$U_0$	2.15	2.5	MeV
Total Cavity Voltage	$V_c$	8.4	6.7	MV
Synchrotron Tune	$\nu_s$	-0.0213	-0.0117	
Bunch Length	$\sigma_z$	6.0(4.9)	5(4.9)	mm
Beam-Beam Parameter	$\xi_y$	0.09	0.0875	
Luminosity	L	$8 \times 10^{35}$		$cm^{-2}s^{-1}$

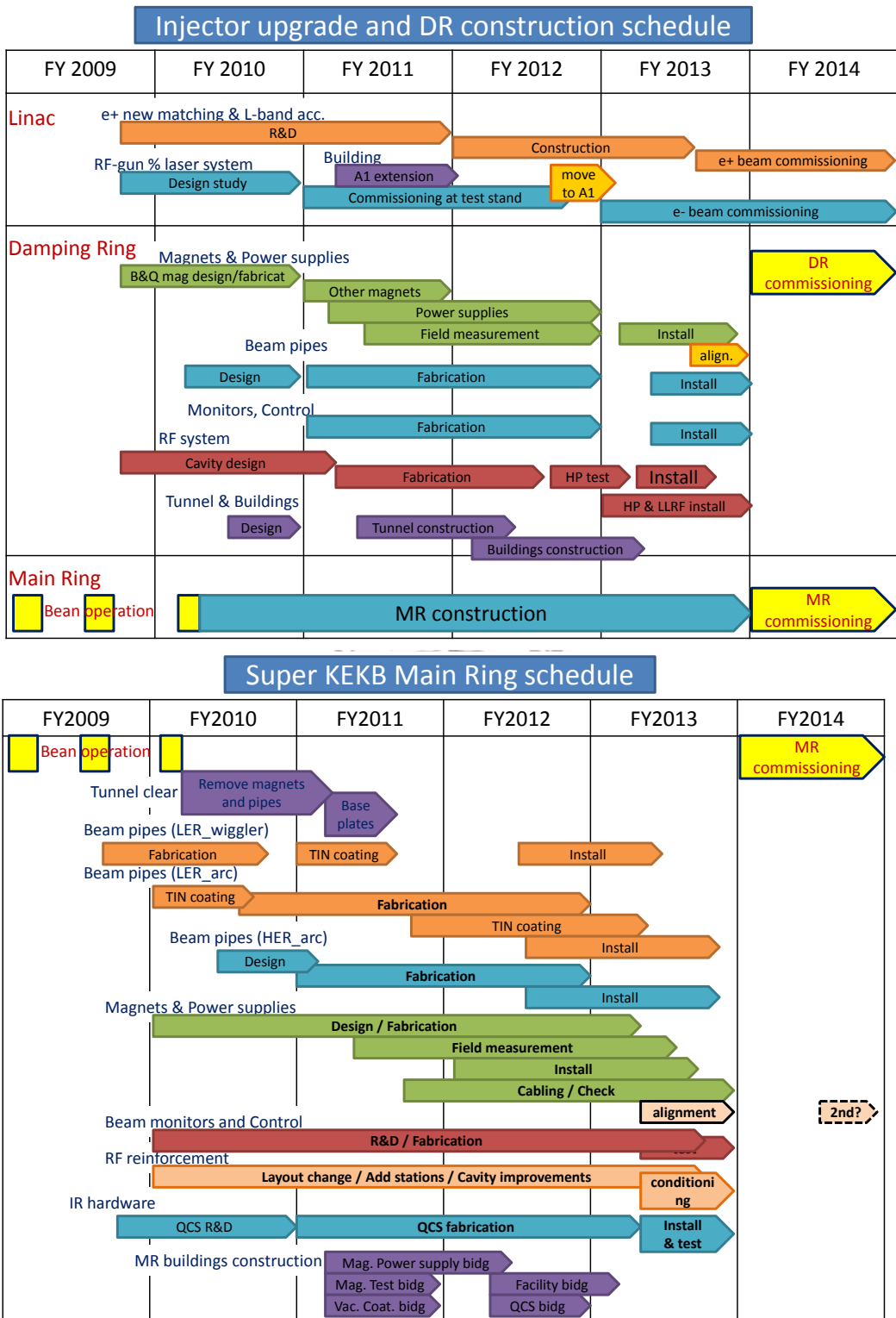


Figure 3.4: Schedules for injector upgrade and damping ring(upper) and Main Ring(lower).

## 3.2 Belle-II Detector

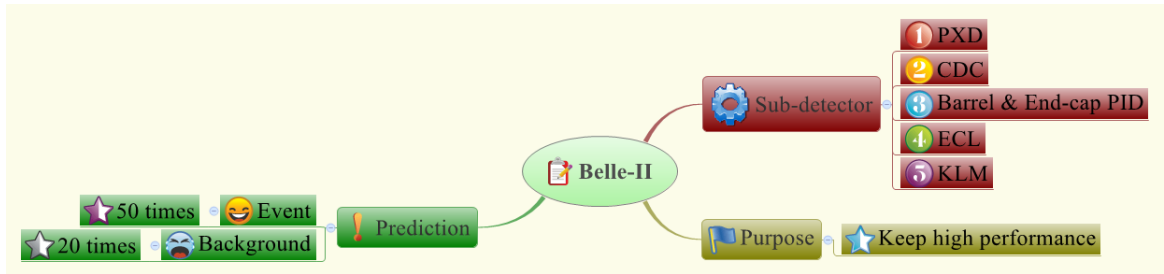


Figure 3.5: The Belle-II related issues in this section.

The main idea of this section is described by the Fig. 3.5. Belle-II is the upgraded detector of Belle.

Belle-II consists several sub-detectors. Almost all of the sub-detectors are upgraded. From the inner to the outer of the Belle-II, the sub-detectors are Pixel Detector(PXD), Silicon Vertex Detector(SVD), Central Drift Chamber(CDC), Barrel and Endcap Particle Identification(PID), Electromagnetic Calorimeter(ECL) and  $K_L$  and  $\mu$  Detector(KLM).

The pixel detector is in the innermost part of the SVD. To increase the crossing angle, we will put the final quadrupoles as close as possible to the interaction point (IP). Meanwhile, we will use smaller beam energy asymmetry ( $7 \text{ GeV}$  for  $e^-$  on  $4 \text{ GeV}$  for  $e^+$  instead of  $8 \text{ GeV}$  on  $3.5 \text{ GeV}$ ).

The Fig. 3.6 shows the geometry difference between Belle-II and Belle detector.

For Belle-II detector, our main concern is to keep the best performance with the considerably high background environment. The possible degradation of the performance in a high background environment can be guessed

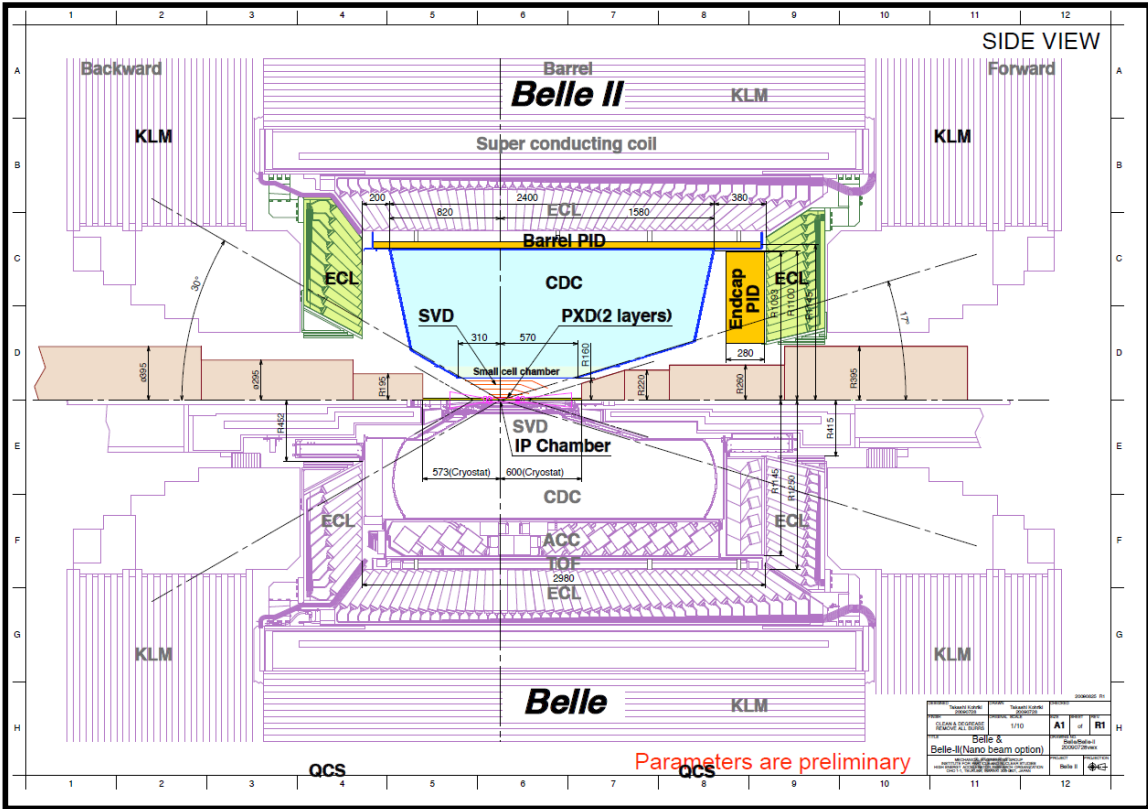


Figure 3.6: The geometry difference between Belle-II (top) and Belle detector (bottom).

from the previous operation in KEKB and Belle. By calculating the scale of each component of background, we find the new environment can be with higher currents, smaller beam size and smaller interaction region. We guess a conservation factor which is twenty times increase in the background. The physics events will be about fifty times higher.

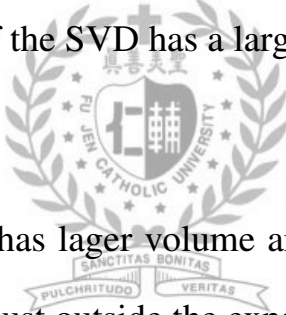
The following changes from Belle will keep comparable or better performance in Belle-II:

- PXD

PXD is just outside the beam pipe. The innermost of SVD is replaced by a two layers pixel detector based on DEPleted Field Effect Transistor(DEPFET) technology. The excellent spatial resolution of PXD improves the vertex resolution.

- **SVD**

The SVD extends from just outside the beam pipe to a larger radius than in Belle. And the readout system is based on the APV25 chip with a much shorter shaping time than the previous. The efficiency for reconstructing  $K_s$  decays to two charged  $\pi$  mesons with hits in the SVD is improved because of the SVD has a larger volume.



- **CDC**

In CDC, the chamber has lager volume and the drift cells are smaller than in Belle. It starts just outside the expanded SVD, and extends to a larger radius.

- **PID system**

The new PID system has higher performance yet more compact. And in the barrel and endcap regions are of the Cherenkov imaging type with very fast readout electronics. The two PID system extend a very good  $\pi/K$  separation to the kinematic limits of the experiment.

- **ECL**

The electronics of the ECL are of the wave-form-sampling type. Re-

placement of the endcap scintillator crystal(CsI(Tl)) is considered with a faster and higher radiation tolerant version (pure CsI) as an upgrade option. The ECL considerably reduces the noise pile up which is particular importance for missing-energy studies.

- **KLM**

The barrel part of the KLM is still equipped with RPCs. But some inner layers of RPCs may be operating in proportional mode. Because the end cap part is replaced with scintillator instrumented with silicon photo multipliers.

- **DAQ**

The new data acquisition system meets the requirements of a considerably higher event rates.



# Chapter 4

## Upgrade CDC and CDC Trigger System

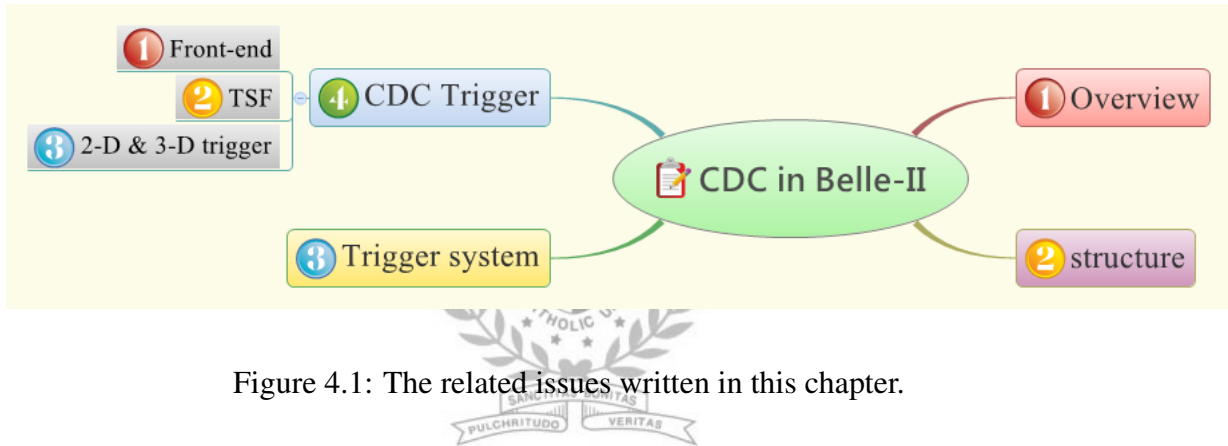


Figure 4.1: The related issues written in this chapter.

CDC plays an important role for track finding and momentum measurement. CDC also provides particle identification and energy loss information for event reconstruction. For low momentum charged tracks, CDC identifies them alone without using other sub-detectors. Moreover, CDC provides efficient and reliable trigger signals from charged particles. The concept of this chapter is plotted in the Figure 4.1.

### 4.1 Overview

The concept of this section is plotted in the Figure 4.2.

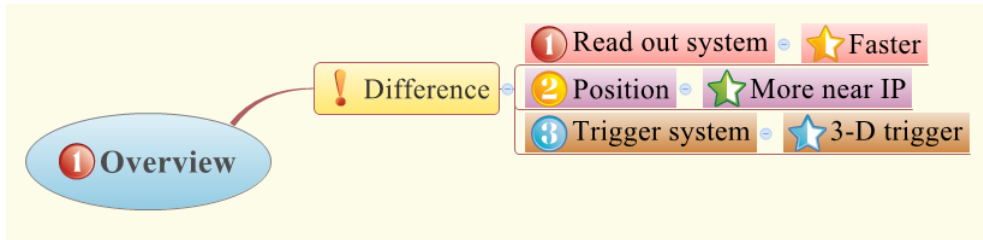


Figure 4.2: The upgrade CDC in Belle-II related issues in this section.

Table 4.1: Main parameter of the CDC Belle and upgraded Belle-II.

	Belle	Belle-II
Radius of inner cylinder(mm)	77	160
Radius of outer cylinder(mm)	880	1130
Radius of innermost sense wire(mm)	88	168
Radius of innermost sense wire(mm)	863	1111.4
Number of layers	50	56
Number of sense wires	8400	14336
Gas	$He - C_2H_6$	$He - C_2H_6$
Diameter of sense wire( $\mu m$ )	30	30

The Belle CDC has operated more than ten years without serious problems. In Belle-II project, CDC keeps the original design. Like the material of the major parts, the super-layer configuration, the cell structure, the wire material, and the gas mixture. The table 4.1 shows the main parameters of CDC in Belle-II and Belle. The CDC size in Belle-II is bigger, the number of layers and sense wires are much more than Belle.

The main difference between the two designs are described as below:

- The new readout electronics system must handle higher trigger rates

with less deadtime. The front-end electronics are located near the backward endplate and send digital signals to the electronics hut through optical fibers.

- To avoid the high radiation and high background and to provide more space to the SVD, the new CDC inner radius is 160 mm. The Belle-II barrel PID system is more compact than in Belle, so the CDC outer radius is 1130 mm. The new wire configuration fills the new modified volume.
- The new CDC provides 3-D trigger information. The z trigger for charged particles is essential to reduce background without loss physics events. In Belle-II, we expect that the beam backgrounds are considerably high, so the z trigger will be important. The z trigger will be based on a 3-D tracking method by using axial and stereo wires. This approach is robust against high beam background and does not need additional material.

## 4.2 Structure

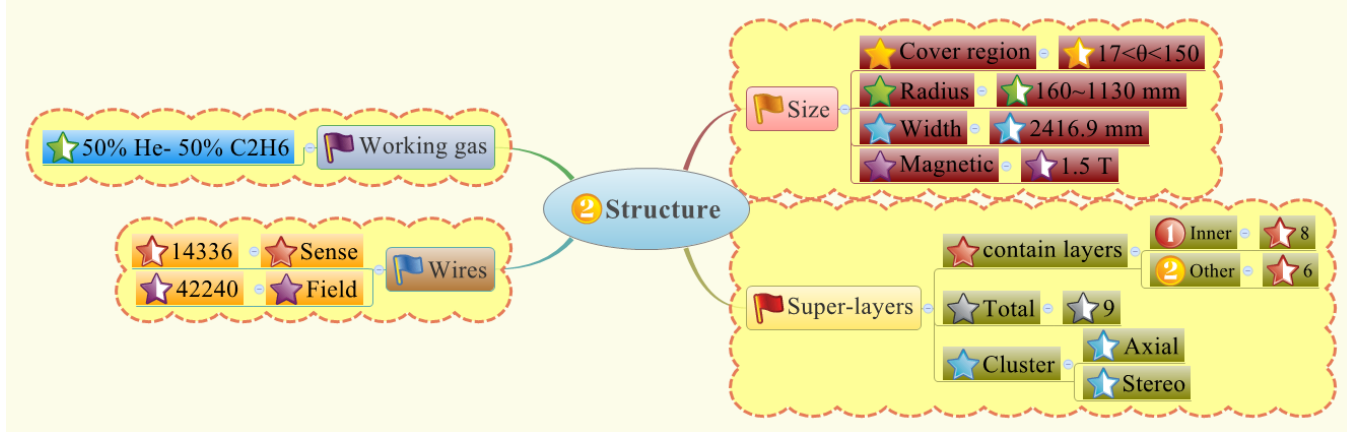


Figure 4.3: The Belle-II CDC Structure related issues in this section.

The main idea of this section is described by the Fig. 4.3. The structure of Belle-II CDC is about the size, the super-layers, the wires and the working gases.

A schematic plot of Belle-II CDC side view is shown in Fig. 4.4. The electron beams fly along the plus z axis. The positron beams fly against the electron beams, along the minus z axis. The yellow middle point is the electron and positron interaction point.

The CDC chamber is a cylindrical wire drift chamber, it covers the region from polar angle  $17^\circ$  to  $150^\circ$ . The red lines are the outermost and innermost of CDC cylinder. And the green lines are the outermost and innermost of sense wires. The total width of CDC structure is 2416.9 mm. The width of front-end region is 1585.7 mm. The back-end width is 831.2 mm. The CDC chamber, it is affected by a 1.5 Tesla magnetic field and filled up with sense

wires.

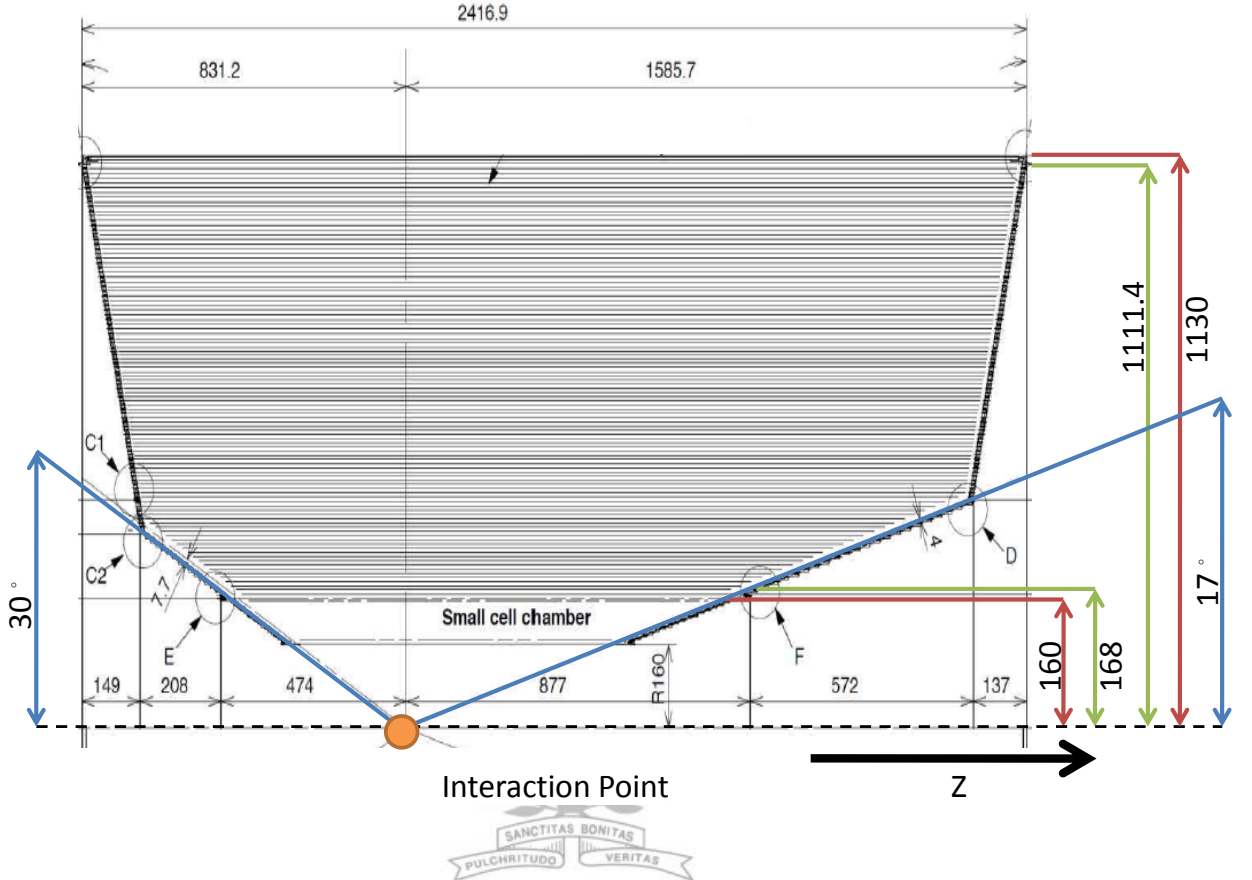


Figure 4.4: A schematic plot of Belle-II CDC side view.

We retain the square cell and super-layer wire configuration from the Belle. There are six layers in each super-layer to make track segment finding easier. The innermost super-layer has additional two layers that contain active guard wires. Even though the performance of these two layers is compromised by the high occupancy from beam backgrounds and the wall effect. The remaining six layers ensure that the innermost super-layer performs as well as the others. The innermost and outermost super-layers contain axial(A) layers. The intervening super-layers alternate between stereo(U or V)

Table 4.2: Configuration of the Belle-II CDC sense wires.

Super-layer type and Number	Number of layers(#)	Signal cells per layer	radius (mm)	Stereo angle (mrad)
Axial 1	8	160	168.0 - 238.0	0
Stereo U 2	6	160	257.0 - 348.0	45.4 - 45.8
Axial 3	6	192	365.2 - 455.7	0
Stereo V 4	6	224	476.9 - 566.9	-55.3 - -64.3
Axial 5	6	256	584.1 - 674.1	0
Stereo U 6	6	288	695.3 - 785.3	63.1 - 70.0
Axial 7	6	320	802.5 - 892.5	0
Stereo V 8	6	352	913.7 - 1003.7	-68.5 - -74.0
Axial 9	6	384	1020.9 - 1111.4	0

and axial layers. In total, there are 9 super-layers(AUAVAUAVA) and 56 layers. The radial cell size is 10 mm for the innermost super-layer and 18.2 mm for the other super-layers. The overall wire configuration shows in Table 4.2 and Fig. 4.5.

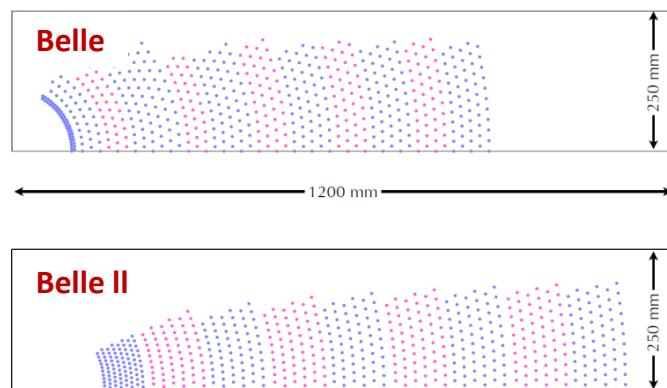


Figure 4.5: Wire configuration of the Belle and Belle-II.

Table 4.3: Main parameter of the CDC Belle and Belle-II.

Wire type	Sense	Field
Material	Tungsten	Aluminium
Plating	Gold	None
Diameter( $\mu m$ )	30	126
Tension(g)	50	80
Number of wires	14336	42240

A larger stereo angle provides better z resolution, but a large variation in radial cell size along the z direction occurs in the boundary region between axial and stereo super-layers. To obtain a 60 mrad stereo angle, a special technique is used without adding insensitive regions: we put string field wires in the transitions with half of the stereo angle. We adjust the radial positions at both end plates around the transitions. The same method is used in Belle. The sense wire is only 1 mm closer to the field wire in this case, so that a large variation is avoided.

The properties of the sense and field wire are shown in Table 4.3. The properties are the same with Belle. The counts are about a factor of 1.7 more than that in Belle. The  $30 \mu m$  diameter of the sense wires will operate at a slightly higher operating voltage. It can make stronger electric field in the drift region and reduces the maximum drift time. The aluminium field wires are used to avoid unnecessary material and to lower the cost.

For the working gas, we prefer to use a new gas with faster drift velocity.

It can reduce the maximum drift time in each cell. But there is no any other mixture gas can be better than that in Belle (mixing of 50% helium-50% ethane). Therefore we won't change the mixture gas. This mixture gas has some advantages: low radiation length, good position resolution, good energy loss resolution, low cross section for synchrotron radiation X-rays and little radiation damage.

### 4.3 Trigger System at Belle-II

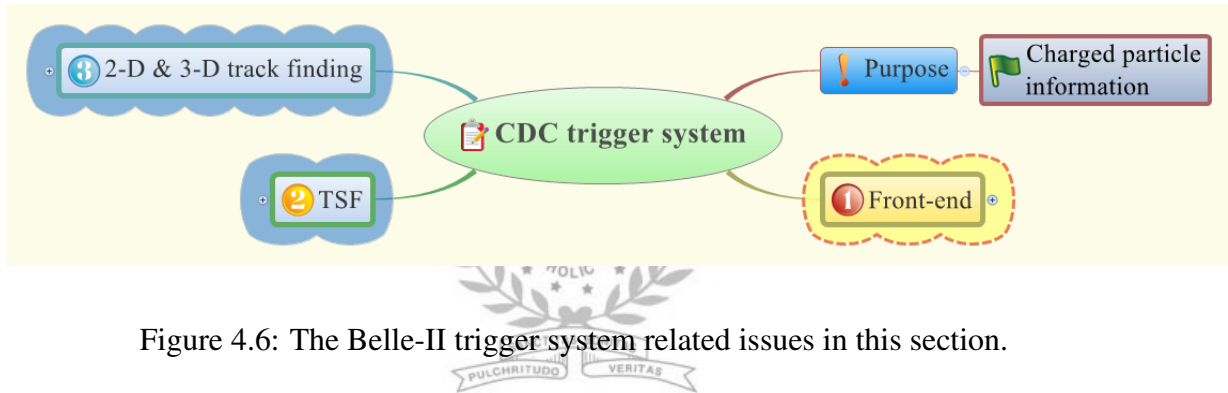


Figure 4.6: The Belle-II trigger system related issues in this section.

The main idea of this section is described by the Fig. 4.6. We are concerned only about the level 1 sub-trigger system, the Global Decision Logic (GDL) and total latency in the trigger system ( $5\mu s$ ).

The schematic overview of Belle-II trigger system is shown in Fig. 4.7. The red lines are new to the trigger system.

About the CDC trigger, it provides the charge track information. Like momentum, position and so on. The ECL trigger provides energy deposit, energy cluster, Bhabha event and cosmic-ray identification.

The Barrel PID trigger provides the precise timing and hit topology in-

formation. The Endcap PID trigger is expected to provide precise timing information, too. The KLM trigger provides muon track information. The Global Decision Logic (GDL) receives all of these sub-trigger informations and make the final trigger decision. This is called level 1 trigger (L1 trigger).

The total latency in the L1 trigger is about  $5\mu s$ . To treat the high efficiency for hadronic events, we use the two independent sub-triggers of CDC and ECL.



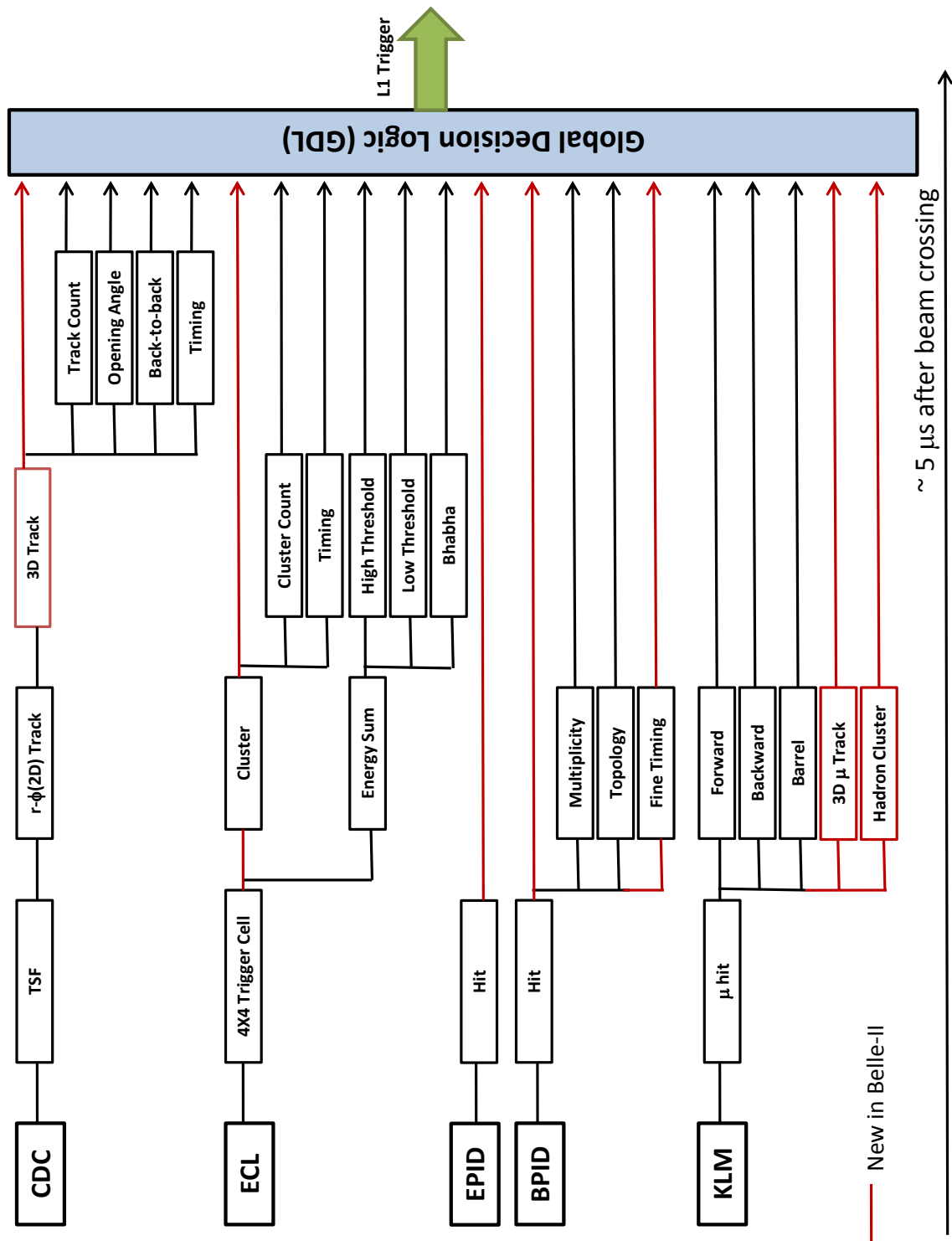


Figure 4.7: The schematic overview of the trigger system. The output from the five sub-trigger system are sent to the Global Decision Logic (GDL). The red lines are new added to the trigger system.

## 4.4 CDC Trigger System at Belle-II

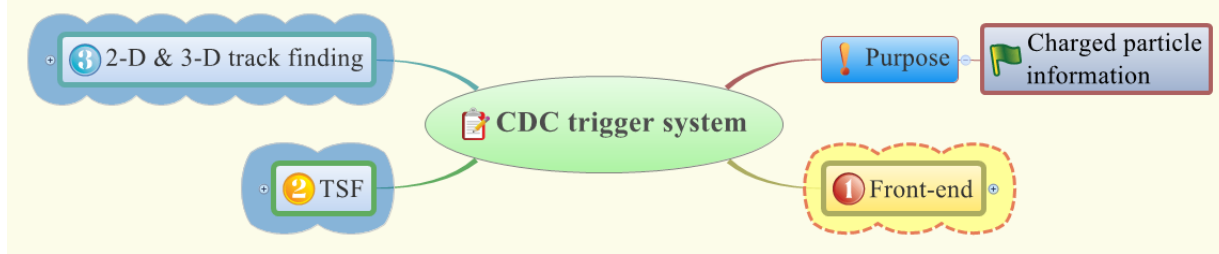


Figure 4.8: The CDC trigger system related issues in this section.

The main idea of this section is described by the Fig. 4.8.

The CDC trigger system provides and characterizes the charged particle tracks detected by the CDC chamber. In the CDC design, we measure  $p_t$ ,  $\lambda$ ,  $d_z$ ,  $\phi$  and the charge of tracks.

Because of the limited solid angle of the CDC chamber, the CDC trigger system isn't detective to charged tracks in the far forward or backward regions. The CDC trigger system should be detective only the charged tracks come from very close to the interaction point( $|d_z| \leq 4\text{cm}$  and  $|d_r| \leq 4\text{cm}$ .).

The Fig. 4.9 is shown the logical flow of CDC trigger system.

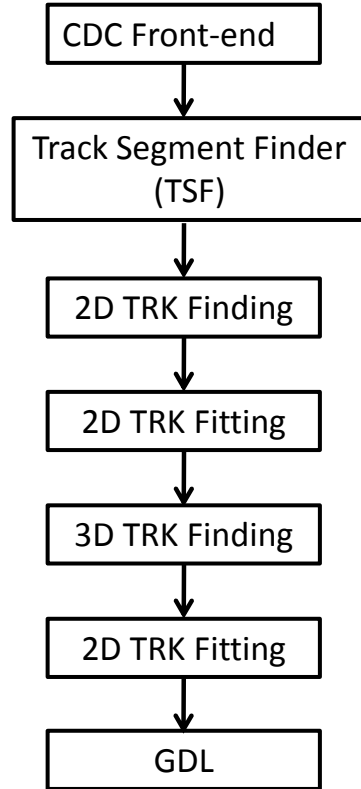


Figure 4.9: The logical flow of CDC trigger system.



#### 4.4.1 CDC Trigger Front-end at Belle-II

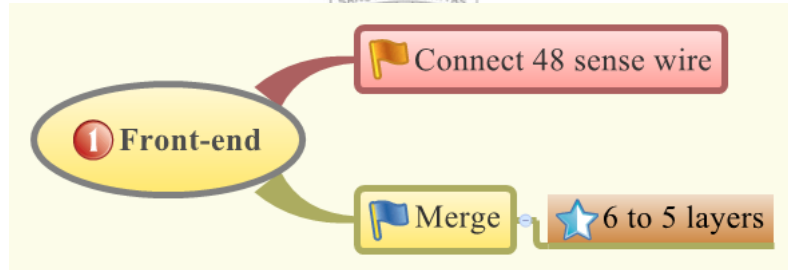


Figure 4.10: The CDC Trigger front-end related issues in this section.

The main idea of this section is described by the Fig. 4.10. This section is mainly discussed the sense wires and layers of CDC trigger system.

Each of 48 CDC sense wires are connected to front-end board. A multiplexer in the front-end board can generate the discriminated signals in each

pulse by using a 1 GHz clock. These precise wire-hit signals are down-sampled by a 62.5 MHz clock.

One-bit hit from the 48 CDC sense wires on the front-end board is sent to the merger multiplexer by the high speed serial links.

The merger multiplexer receives 6 wire layers information from front-end board, and merges the 6 layers information to 5 layers information. The 5 layers information will be sent to TSF stage. Each line in Fig. 4.11 corresponds to a super-layer in the CDC chamber. There are three to six merger multiplexers per super-layer. The number of merger multiplexers are depending on the number of sense wires per super-layer.



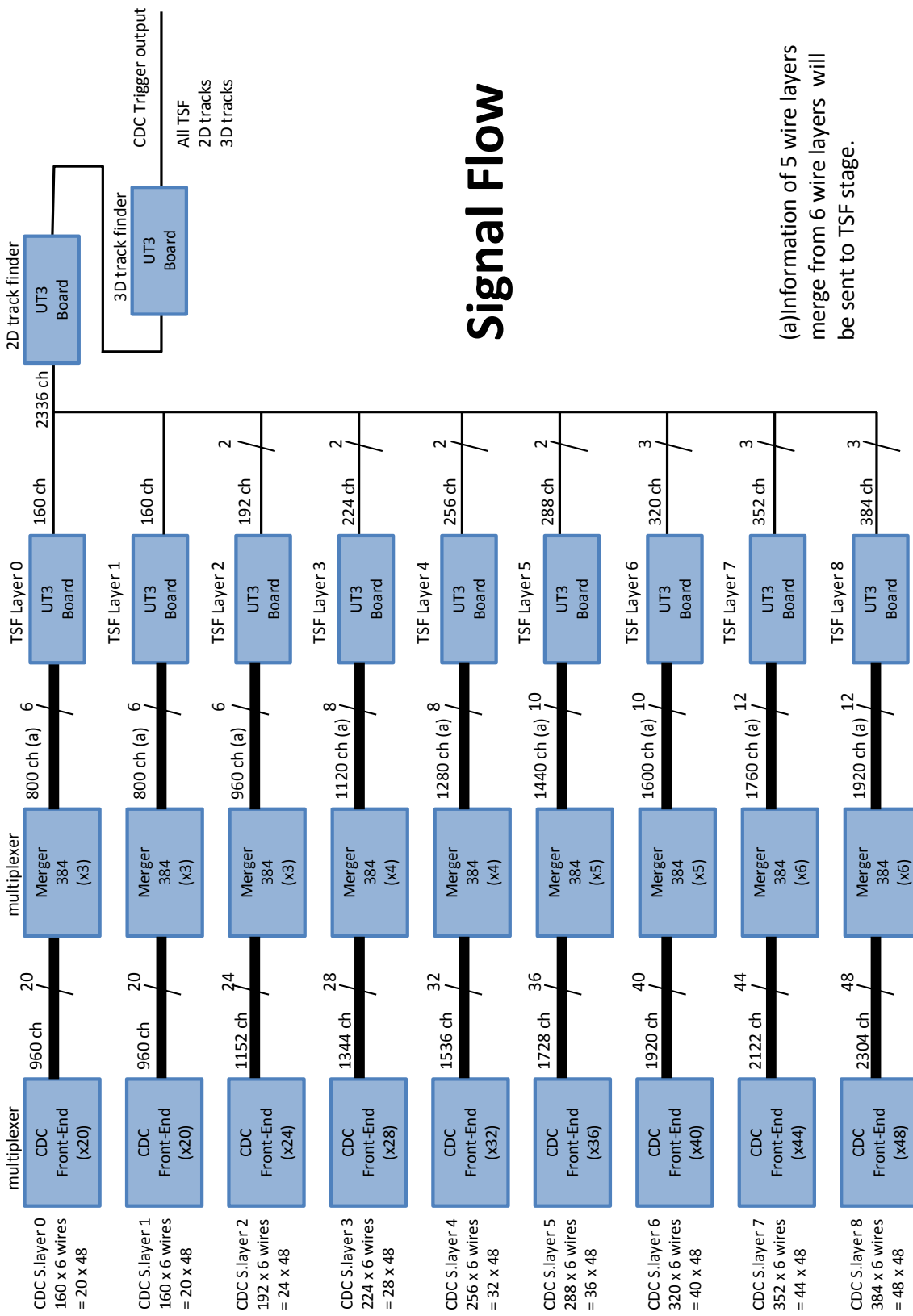


Figure 4.11: Hardware configuration of the CDC trigger system.

#### 4.4.2 Track Segment Finder in CDC at Belle-II

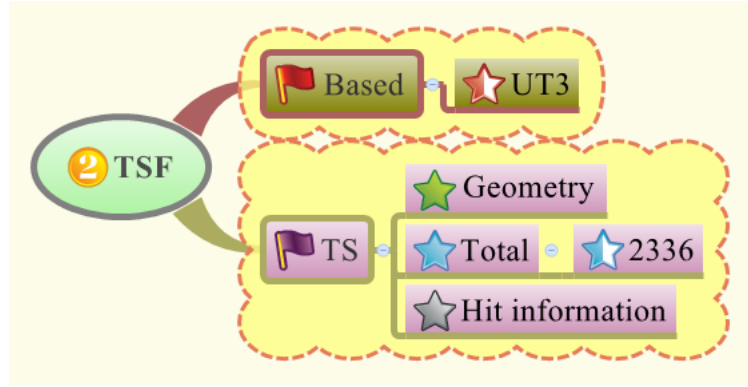


Figure 4.12: The Track Segment Finder (TSF) related issues in this section.

The main idea of this section is described by the Fig. 4.12.

The wire hit information after the collecting of merger multiplexer, is sent to the next stage, the Track segment Finder (TSF). The TSF is realized using one Universal Trigger Board (UT3) per super-layer, so there are nine such board in total.

In Fig. 4.13, it is shown the geometric patterns for Track Segments (TS) in each TSF.

The number of TS in a super-layer are depending on the sense wires in a single wire layer.

Each TS shape overlaps the neighbouring TS, but the center cell doesn't overlaps with other TS. The Fig. 4.14 is shown the sense wires and TS relation. There are 2,336 TS in total. At each tick of the 62.5 MHz clock, the pattern of wire hits in each TS is examined. The hit patterns are expected for

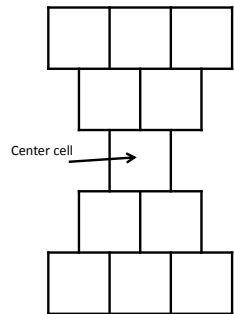
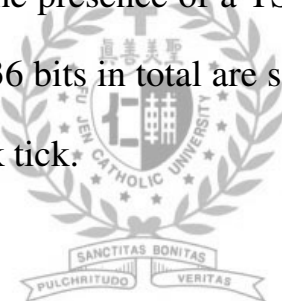


Figure 4.13: The geometric shape of a track segment(TS). Each square corresponds to a wire cell.

a charged particle track. The tracks are predefined and stored in a memory. By searching the memory, the presence of a TS hit can be determined. The TS hit information with 2,336 bits in total are sent to the 2-D Track Finding stage (Fig. 4.9) at each clock tick.



Layer ID	# wires	S.Layer ID	#Wires to TSF	#TSs	Layer	26	256	Layer	27	256	Layer	28	256	Layer	29	256	Layer	30	256	Layer	31	256	Layer	32	288	Layer	33	288	Layer	34	288	Layer	35	288	Layer	36	288	Layer	37	288	Layer	38	320	Layer	39	320	Layer	40	320	Layer	41	320	Layer	42	320	Layer	43	320	Layer	44	352	Layer	45	352	Layer	46	352	Layer	47	352	Layer	48	352	Layer	49	352	Layer	50	384	Layer	51	384	Layer	52	384	Layer	53	384	Layer	54	384	Layer	55	384
Total	# layers	# wires	# S.layers	# wires to TSF	# TSs																																																																																									
Layer 0	160																																																																																													
Layer 1	160																																																																																													
Layer 2	160																																																																																													
Layer 3	160																																																																																													
Layer 4	160	0		800	160																																																																																									
Layer 5	160																																																																																													
Layer 6	160																																																																																													
Layer 7	160																																																																																													
Layer 8	160																																																																																													
Layer 9	160																																																																																													
Layer 10	160	1		800	160																																																																																									
Layer 11	160																																																																																													
Layer 12	160																																																																																													
Layer 13	160																																																																																													
Layer 14	192																																																																																													
Layer 15	192	2		960	192																																																																																									
Layer 16	192																																																																																													
Layer 17	192																																																																																													
Layer 18	192																																																																																													
Layer 19	192																																																																																													
Layer 20	224																																																																																													
Layer 21	224																																																																																													
Layer 22	224	3																																																																																												
Layer 23	224																																																																																													
Layer 24	224																																																																																													
Layer 25	224																																																																																													

Figure 4.14: Table of the sense wire, super-layers and TSs relation

#### 4.4.3 2-D Track Finding and 3-D Trigger in CDC at Belle-II

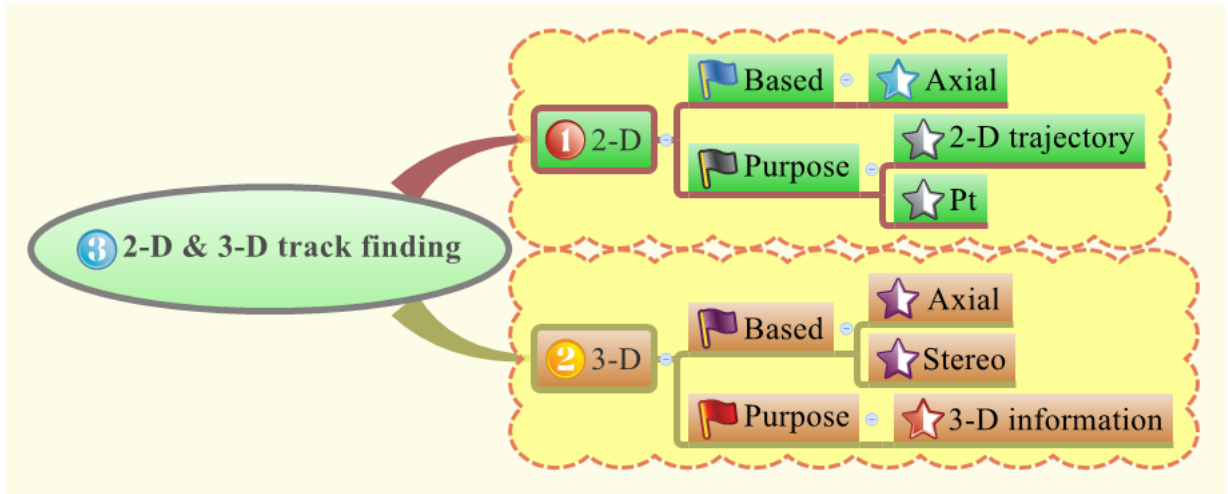


Figure 4.15: The 2-D Track Finding and 3-D trigger related issues in this section.

The main idea of this section is described by the Fig. 4.15. This section is to talk about the main difference and the purpose of 2-D and 3-D track finding.

After Track Segment Finder (TSF) finishing its job, the TS hits information are sent to the 2-D Track Finding program.

The CDC 2-D track finding program is one of main component of the charged track triggers. The 2-D track finding is based on the signals from axial super-layers. The main purpose is to identify the charge tracks originating from the interaction point, and determination of the charge particle transverse momentum  $p_t$ . In short, the 2-D track finding is a function to obtain the charge track function in x-y plane. These charge track informations are sent to the 3-D trigger later.

The CDC 3-D trigger is another main component of the charge track trig-

gers. It is the last stage in CDC trigger system. The CDC 3-D trigger system is received the track information in  $r - \phi$  plane, and the signals from stereo and axial super-layers. The 3-D trigger system provides the 3-D information of the track, like  $p_z$  and the 3-D track function. The 3-D informations are sent to the Global Decision Logic (GDL) to make the final L1 trigger decision.



# Chapter 5

## 2-D Track Finding Algorithm and Hough Transformation

The main idea of this section is described by the Fig. 5.1. The 2-D Track finding algorithm is a method to obtain the track functions. The method itself is called Hough Transformation.

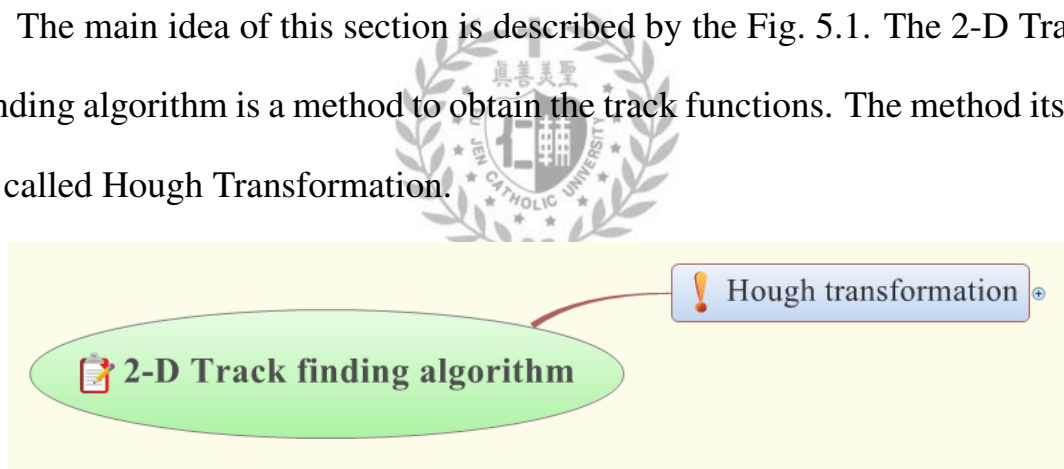


Figure 5.1: The 2-D Track finding algorithm and Hough Transformation related issues in this chapter.

### 5.1 2-D Track Finding Algorithm

My thesis is mainly dealing with the 2-D Track finding. For the 2-D track finding, we should find the charge track function in the CDC x-y plane.

After we obtain the TS hits information from axial super-layers, we apply the Hough transformation method to find the track functions.

The Hough transformation is a feature extraction technique used in image analysis. The purpose of the technique is to find imperfect instances of objects within a certain class of shapes by a voting procedure. This voting procedure is performed in a parameter (Hough) space.

## 5.2 Hough Transformation

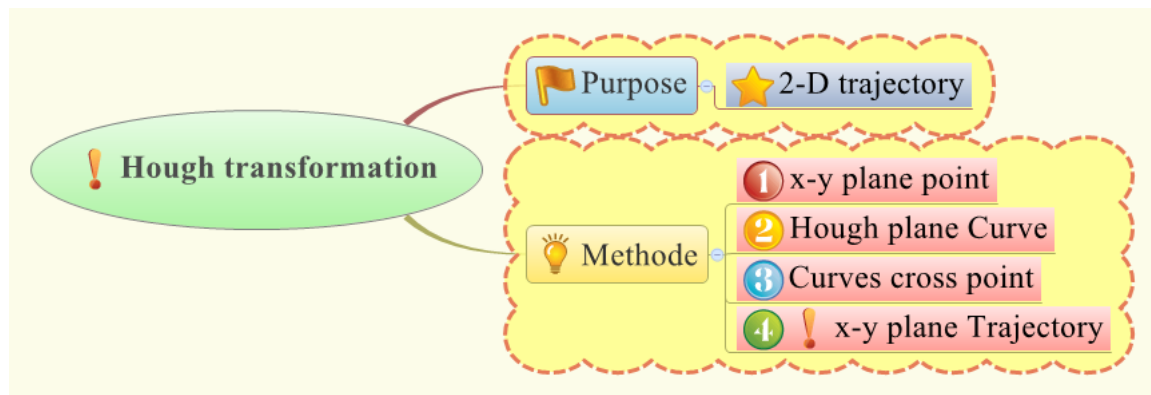


Figure 5.2: The Hough transformation related issues in this section.

The main idea of this section is described by the Fig. 5.2.

Every point in 2-dimensional space (x-y space), we can find two kinds of circles with different size through the zero point and the point itself.

One kind of the circles is right handed circle, and the other kind is left handed circle. It is plotted as in Fig. 5.3.

The two kinds of circles are all satisfied the following equation:

CDC x-y plane

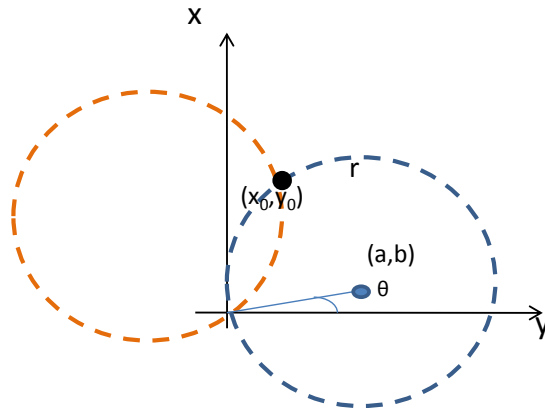


Figure 5.3: Schematic view of the right handed and left handed circles in the CDC x-y plane.

$$(x - a)^2 + (y - b)^2 = r^2 = a^2 + b^2 \quad (5.1)$$

In equation 5.1,  $(a, b)$  is the circle center and  $r$  is the circle radius. To satisfy different circles size, the  $a$  and  $b$  should be free parameters.

The equation 5.1 expands to equation 5.2.

$$x^2 - 2ax + y^2 - 2by = 0 \quad (5.2)$$

Because  $a$  and  $b$  should satisfy different radius size circles,  $a$  and  $b$  can be from  $-\infty$  to  $+\infty$ . It's hard to restrict the maximum value. We replace  $a$  and  $b$  parameters to  $r$  and  $\phi$ . The relation of  $a, b$  and  $r, \phi$  are as below:

$$a = r \cos \phi, b = r \sin \phi$$

This is a transformation from the Cartesian coordinate system to Polar

coordinate system. The  $r$  is the radius and the  $\phi$  is the polar angle.

The  $\phi$  can be limited within 0 to  $2\pi$ . We can therefore restrict the maximum radius value.

In the circle equation 5.2, we transform the Cartesian coordinate system to Polar coordinate system. The equation becomes the following equation 5.3.

$$x^2 - 2xr \cos \phi + y^2 - 2br \sin \phi = 0 \quad (5.3)$$

The radius in equation 5.3 can be written as the following equation 5.4.

$$r = \frac{x^2 + y^2}{2x \cos \phi + 2y \sin \phi} \quad (5.4)$$

If we can have a certain point  $(x_0, y_0)$  in x-y space, we can rewrite the equation 5.4 to be a  $r - \phi$  relation function.

$$r = \frac{x_0^2 + y_0^2}{2x_0 \cos \phi + 2y_0 \sin \phi}$$

The relation function above corresponds to two arcs in Hough plane (the  $r - \phi$  space).

We use the logarithm of  $r$  to scale up the difference of  $r$ .

One of the two arcs satisfies the right handed circle, and the other satisfies the left handed circle.

We named the left handed circle curves in the Hough plus plane and the right handed circle curves in the Hough minus plane. Their plots are shown in the Fig. 5.4.

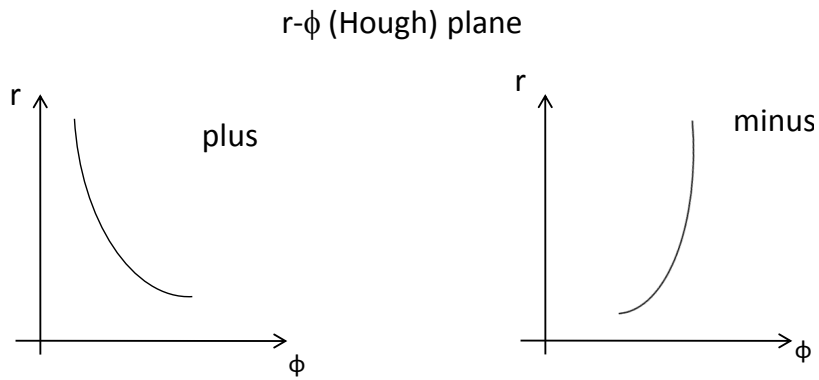


Figure 5.4: Schematic view of Hough plane. (a) left handed side is plus plane. (b) right handed side is minus plane.

Each point in x-y space corresponds one arc in the Hough plane. We call this procedure the Hough Transformation.

When a track passing through the CDC, there are many points  $(x_i, y_i)$  shown in x-y space. We have to transform every point in the Cartesian coordinate system to Polar coordinate system by Hough Transformation.

We can check the Hough plus plane and Hough minus plane to find the track function.

For example, in the Fig. 5.5. In Hough minus plane, there are 4 arcs in parallel. They can't have a single solution for CDC x-y plane. But in Hough plus plane, there are 4 arcs all passing through a point. The cross point  $r_0$  and  $\phi_0$  are the solution for the track function in the CDC x-y plane. The solution is shown in the Fig. 5.6.

It is important to obtain the crossing point in Hough plane. In 2-D Track finding, we use the Hough transformation algorithm to obtain the charge tra-

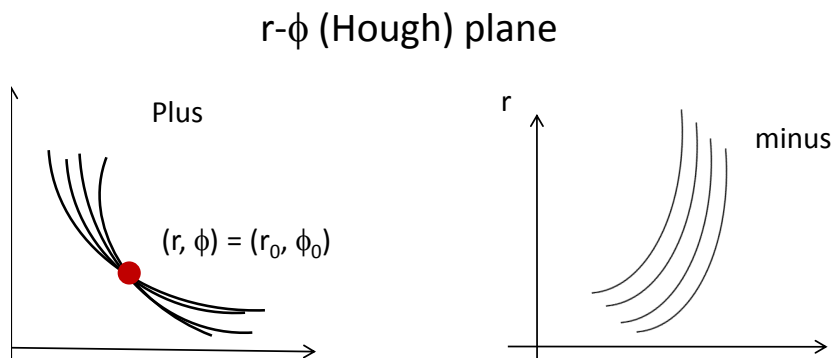


Figure 5.5: In Hough plus plane, there are 4 arcs and they all pass through a point. A track function can be formed in this case. In Hough minus plane, there are 4 arcs in parallel. That means no track function can be formed.

jectory function. After we find the crossing point, we find the trajectory function too.

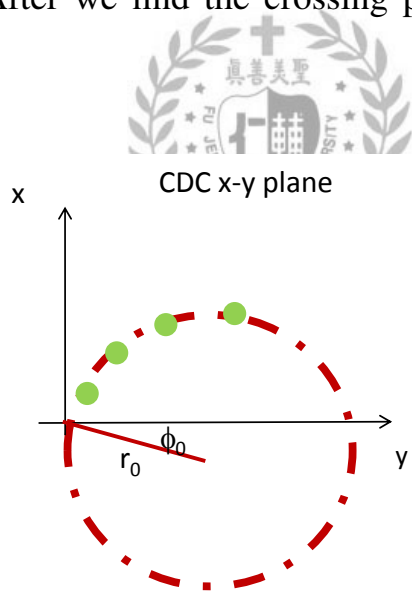
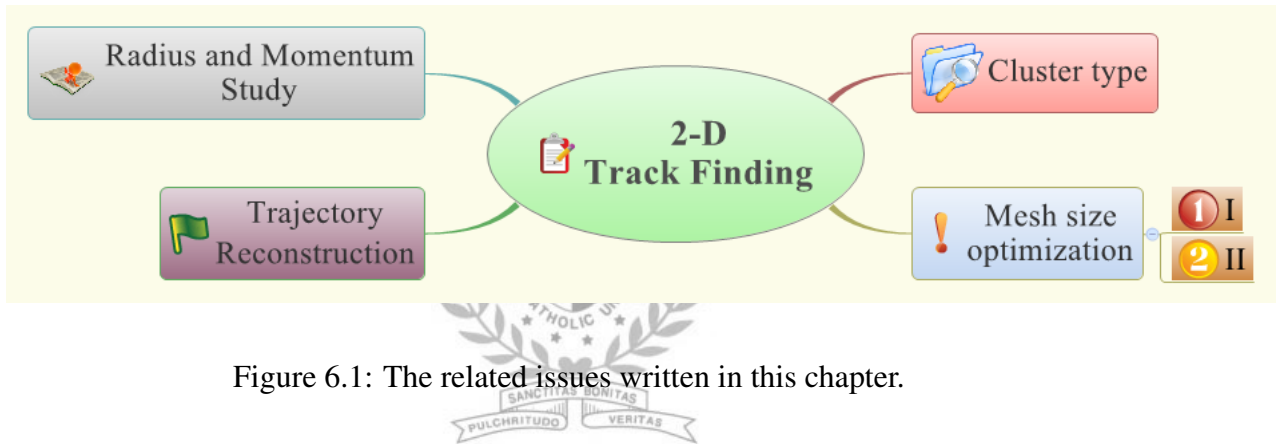


Figure 5.6: The cross point  $r_0$  and  $\phi_0$  are the solution of the track function in the CDC x-y plane.

# Chapter 6

## 2-D Track Finding Simulation



In this chapter, we discuss the types of clusters, separate the good and bad cluster types, optimize the mesh size, and check the basic relationship between the momentum and the radius of the charged particles.

### 6.1 Types of Clusters

The concept plot for this section is described in the Figure 6.2.

We generate a single charged particle using basf2. We set this charged particle to be a  $\pi^+$  meson, with momentum  $0.8 \text{ GeV}/c$  passing through the CDC chamber. In Fig. 6.3, it is an event display showing a flying track in

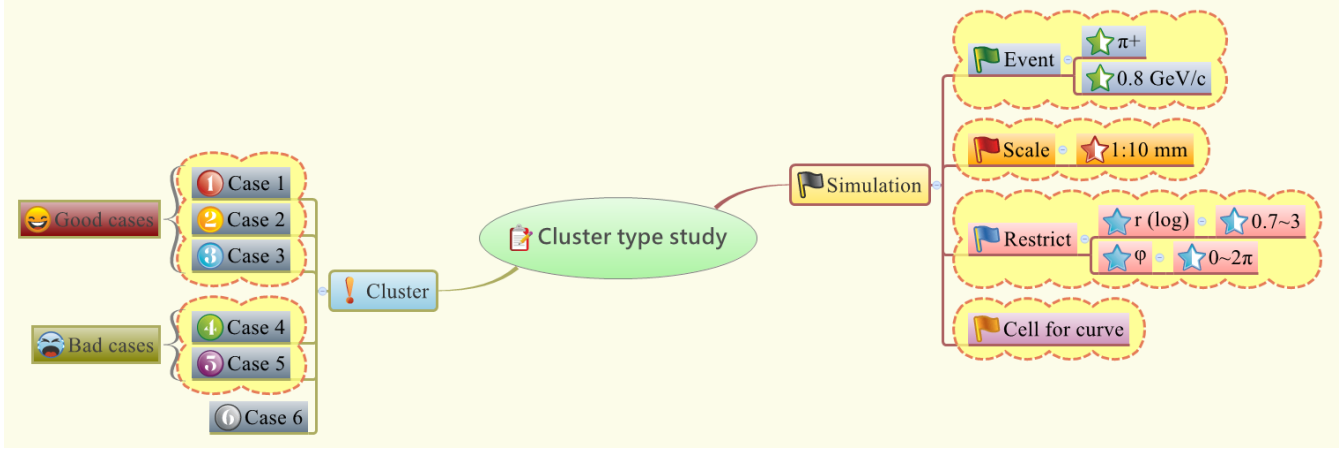


Figure 6.2: The Cluster type study related issues in this section.

CDC real-plane (x-y plane). In this CDC x-y plane, each bin size stands for 10 mm.

In total, there are 9 super-layers in CDC chamber. Among the 9 super-layers, there are 5 axial super-layers. For 2-D track finding, we need only the hit information from the axial super-layers. So, our maximum hit layers is 5.

We use Hough transformation to get each Track Segment(TS) points, and put the corresponding arcs in Hough plus and minus plane. One arc is for one TS hit. In Hough plane, we use logarithm radius which is from 0.7 to 3. The  $\phi$  region is from 0 to  $2\pi$ . The Track Segment is described in the previous section 4.4.2.

An example of our Hough transformation is shown in Fig. 6.4.

Ideally, these arcs in Hough plane should be a perfectly curve line. However, these arcs are stacked as some clusters.

The size of mesh is related to resolution. We need to find a best mesh size for operation.

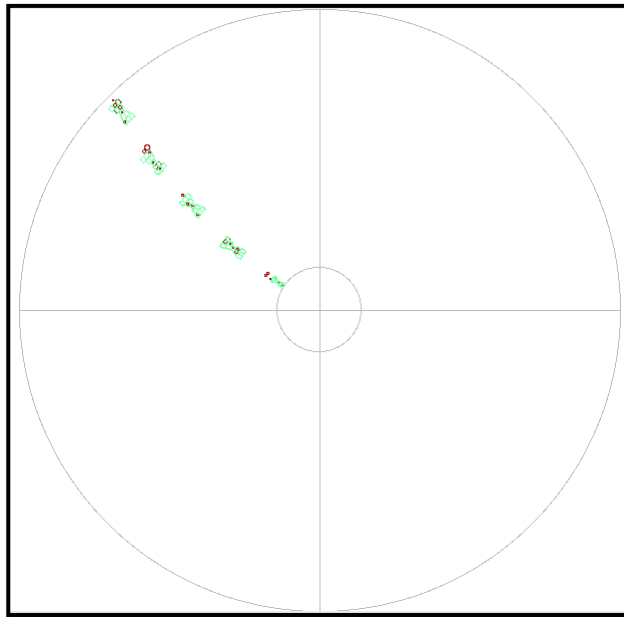


Figure 6.3: A single  $\pi^+$  passes through the CDC chamber. The green tracking points are the TS hits in each axial super-layers.

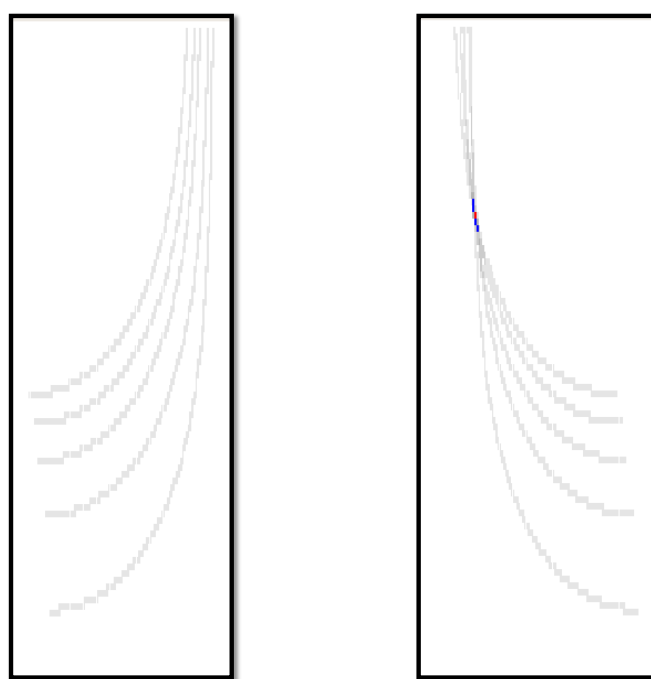


Figure 6.4: An example of our Hough transformation.

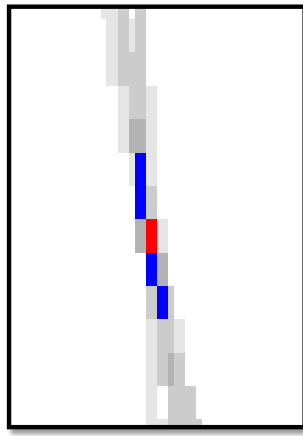


Figure 6.5: Only one peak region in Hough plane.

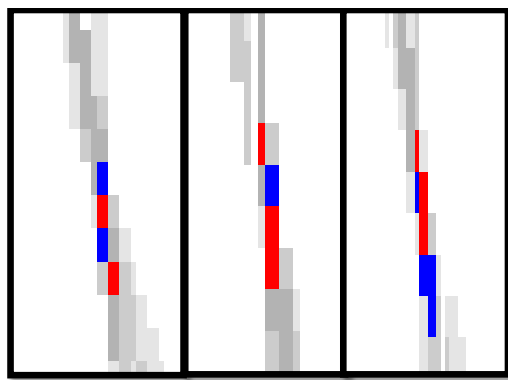


Figure 6.6: More than one peak region in Hough plane.

Ideally, these arcs in Hough plane should be perfectly across one mesh, as shown in the Fig. 6.5. The blue block means 4 arcs are collected and the red block means 5 arcs are collected. The red block is named peak region. Only one peak region exists in this plot. It is easy for us to decide the peak position. But, there are some other cases, like Fig. 6.6. We need to find a method to deal with the peak position.

We classify these peak performance into six cases. According these cases,

we manage to calculate their peak position. If we can find the peak position, we call this kind of case a good case. If we can't, we call this kind of case a bad case.

- Case 1.

Case 1 is a perfect case. Only one peak region exists in the Hough plane. The peak position is the center of the only red block. The Figure 6.7 shows the results.

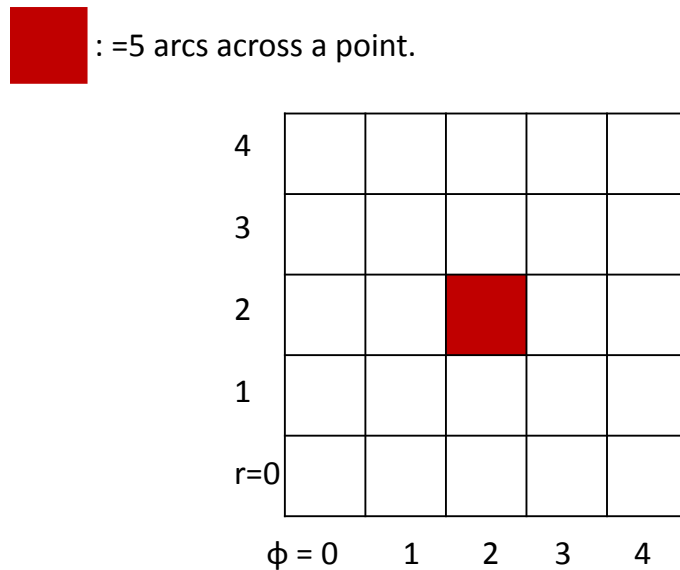


Figure 6.7: Schematic of the case 1, a perfect case. There is only one red block in the Hough plane. The peak position is the center of the only red block.

- Case 2.

Case 2 is another good case. Because the peak regions are connected with each other. The Figure 6.8 shows the results. In this case, we can average the center of the red blocks and get an averaged peak position.

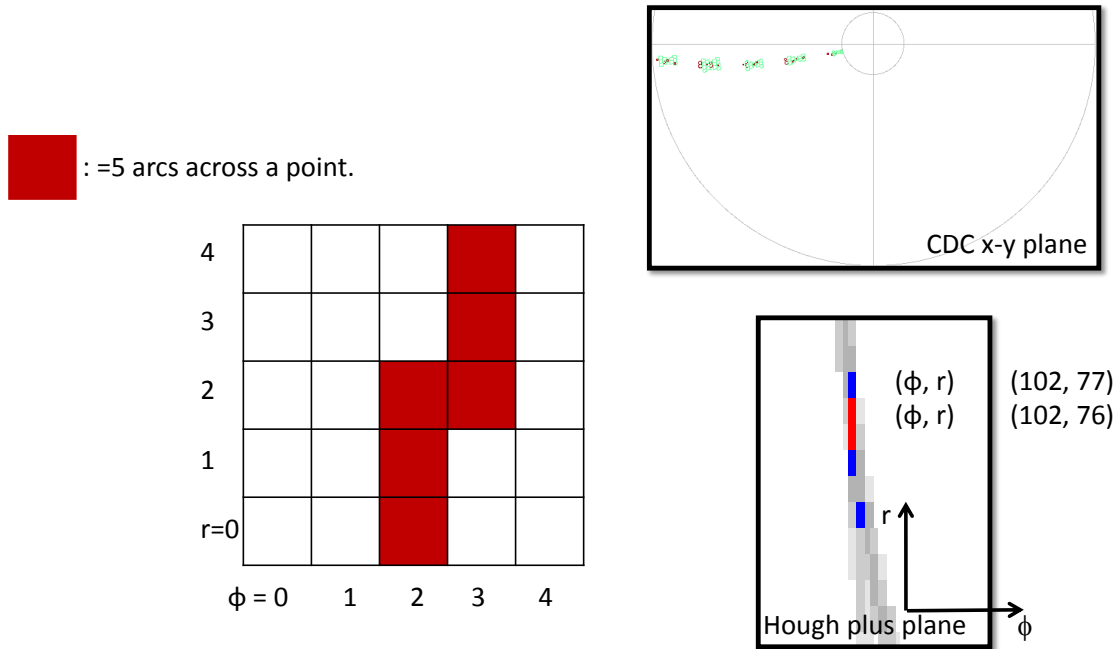


Figure 6.8: Left plot is the schematic of the case 2, a good case. Right-up is the corresponding simulation result in the CDC x-y plane. Right-bottom plot is the case in the Hough plus plane.

- Case 3.

Case 3 is another good case. Because most of the peak regions are connected with each other. The Figure 6.9 shows the results. In this case, we can average the center of the connected red blocks and get an averaged peak position. The fewer isolated red blocks are removed.

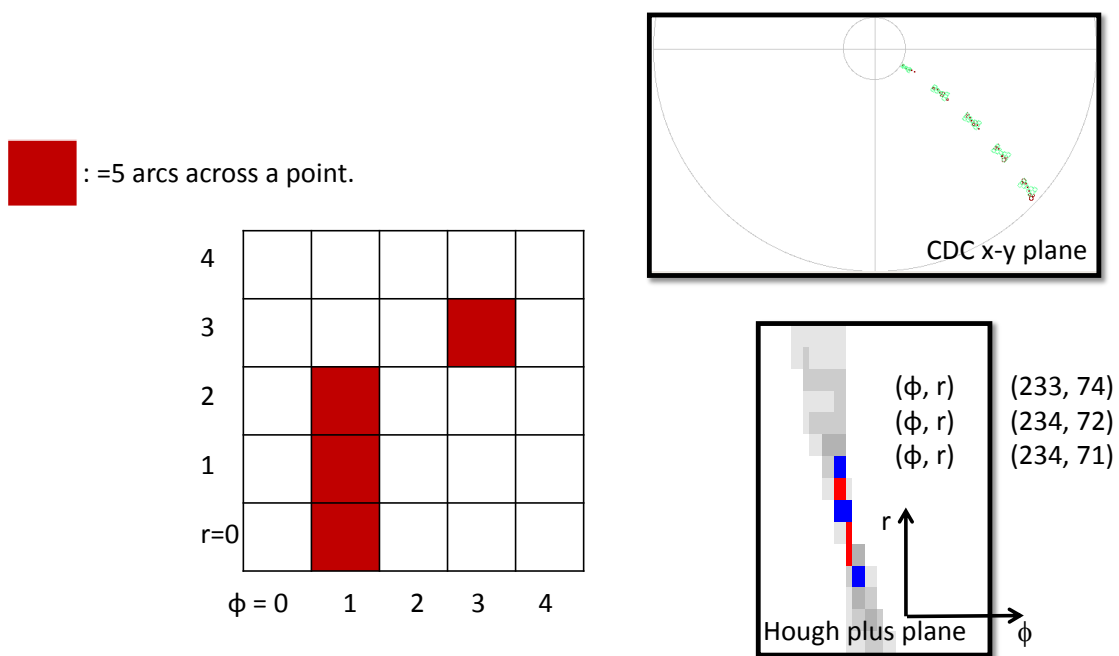


Figure 6.9: Left plot is the schematic of the case 3, a good case. Right-up is the corresponding simulation result in the CDC x-y plane. Right-bottom plot is the case in the Hough plus plane.

- Case 4.

Case 4 is a bad case. Because we can't find the most connected peak regions. We can't calculate the peak position. The Figure 6.10 and Figure 6.11 show the results.

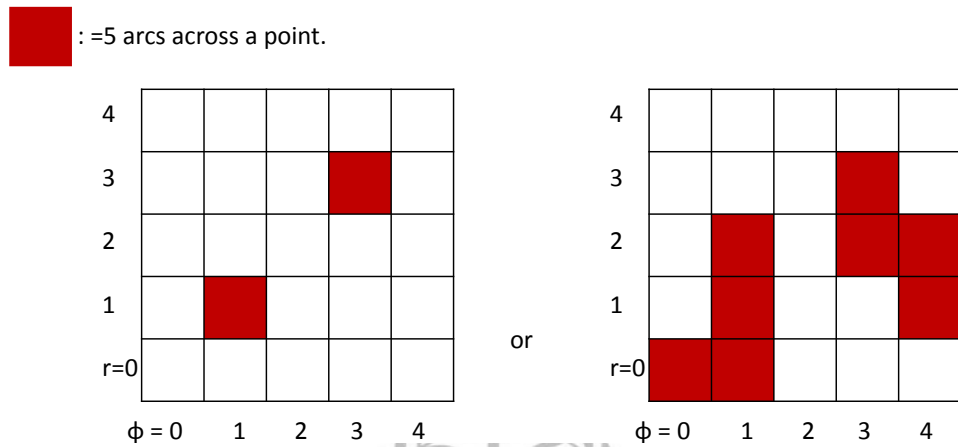


Figure 6.10: Two kinds of schematic of the case 4, bad cases.



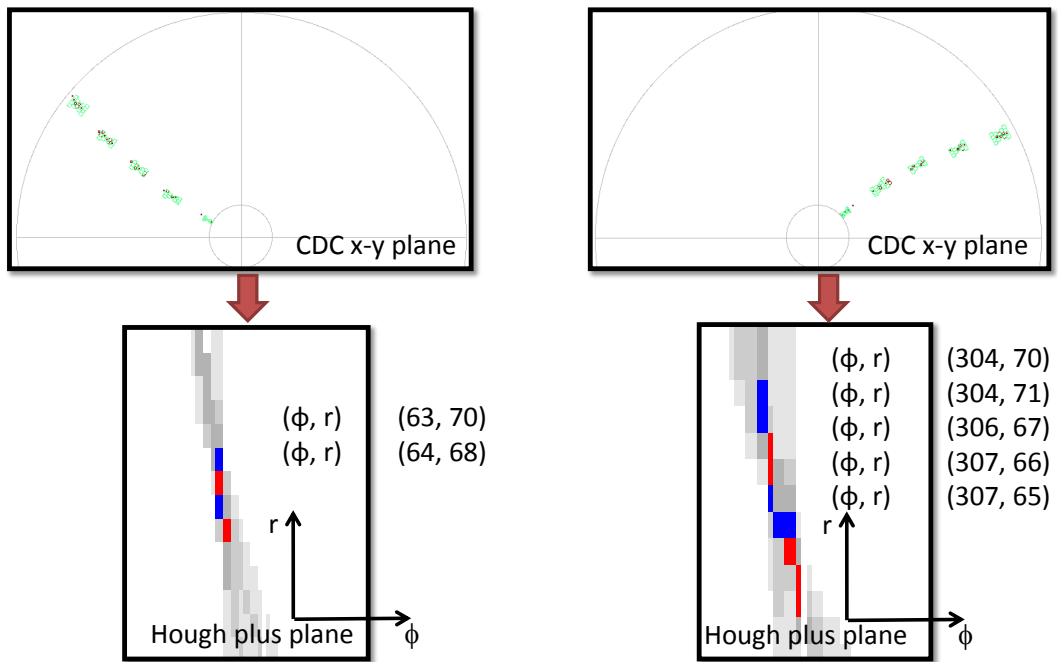


Figure 6.11: Two kinds of case 4 plots, bad cases. Top plots are the corresponding simulation results in the CDC x-y plane. Bottom plots are the cases in the Hough plus plane.

- Case 5.

Case 5 is a bad case. Because we can't find any red blocks. We can't calculate the peak position. The Figure 6.12 shows the results.

 :=4 arcs across a point.

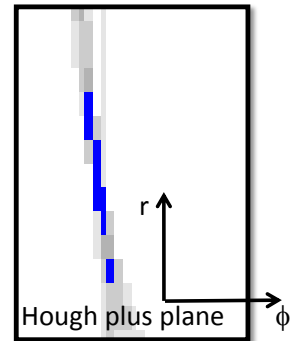
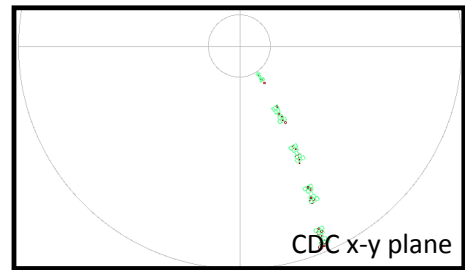
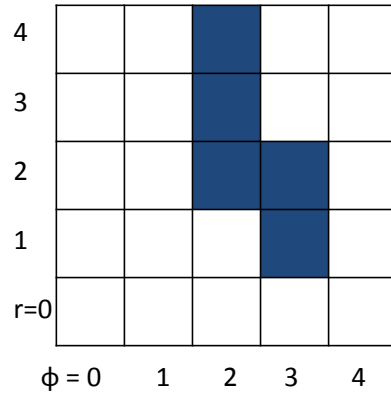
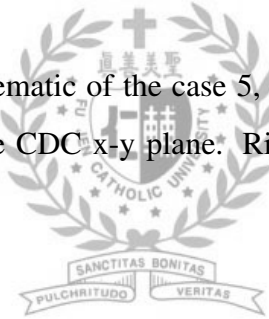


Figure 6.12: Left plot is the schematic of the case 5, a bad case. Right-up is the corresponding simulation result in the CDC x-y plane. Right-bottom plot is the case in the Hough plus plane.



- Case 6

Case 6 is a bad case. It is a mistake case because the incorrect boundary condition settings. The Fig 6.13 shows the results.

The six cases above can be classified into two categorises. One kind is called good case because we know how to obtain the peak position. The other kind is called bad case because we don't know how to obtain the peak position.

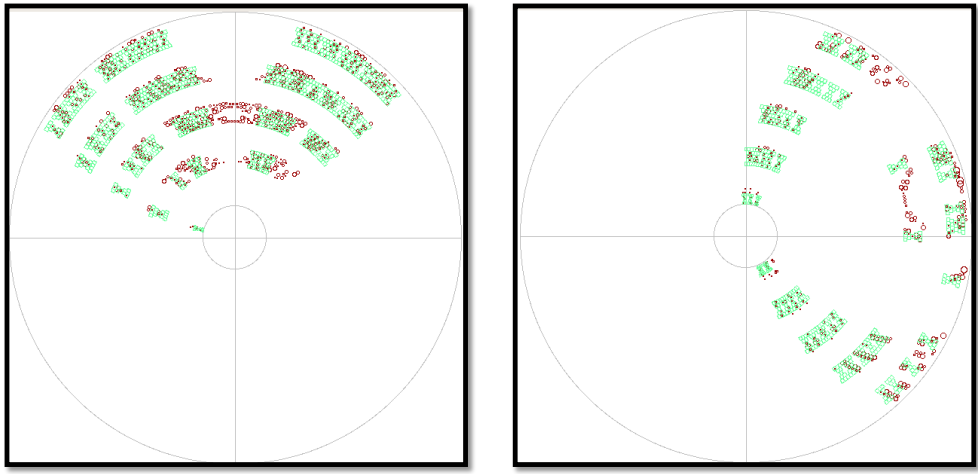


Figure 6.13: Two kinds of the simulation result in the CDC x-y plane of the case 6, bad cases.

## 6.2 Mesh Size Optimization



Figure 6.14: The Mesh size optimization related issues in this section.

In the beginning, the default mesh size is divided into 350 bins in the  $\phi$  region and 100 bins in the logarithm  $r$  region. We use  $(\phi 350, r 100)$  to present this idea throughout the whole study.

We generate a hundred events to understand the percentage of the good cases and bad cases in this mesh size. The environmental setting is a single

charged particle  $\pi^+$  passing through the CDC, with 0.8 GeV/c momentum.

Table 6.1 and Table 6.2 show the percentage results. In the Table 6.1, we only separate the 100 events into six cases. In the Table 6.2, we remove the contribution from case 6 and calculate the percentage of good cases and bad cases. The percentage of good cases is 78% and bad cases is 22%.

Table 6.1: We separate the 100 events into six cases, in the divided mesh size of ( $\phi$  350,  $\log r$  100).

case	numbers (#)	ratio (%)
Case 1	21	21
Case 2	29	29
Case 3	11	11
Case 4	5	5
Case 5	12	12
Case 6	22	22



We want to improve the ratio of good cases by modifying the divided mesh size.

For each divided mesh size, we use the same environmental settings as the previous test. The environmental setting is a single charged particle  $\pi^+$  passing through the CDC, with 0.8 GeV/c momentum. One hundred generated events are used.

The table 6.3 shows the overall ratios of the good and bad cases in each mesh size. More details are shown in the Appendix A.

We can find two tendencies. One is when the divided  $r$  size is fixed, the

Table 6.2: We remove the contribution from case 6 and calculate the percentage of good cases and bad cases. The percentage of good cases is 78% and bad cases is 22%. The divided mesh size is  $(\phi 350, \log r 100)$ .

case	ratio without case 6 (%)	ratio (%)	
Case 1	26.9		
Case 2	37.2	78.2	Good Case
Case 3	14.1		
Case 4	6.4		
Case 5	15.4	21.8	Bad Case
Case 6	×	×	×

increasing of  $\phi$  divided regions can improve the ratio of good cases. The other one is when the divided  $\phi$  size is fixed, the increasing of  $r$  divided regions can reduce the ratio of good cases.

In the table 6.3, we can see the best mesh size should be divided into  $(\phi 200, r 50)$ .

Table 6.3: The ratio of good and bad cases in different divided mesh sizes. The best mesh size should be divided into  $(\phi 200, \log r 50)$ .

Divided mesh size $(\phi, \log r)$	Good cases ratio(%)	Bad cases ratio(%)	Divided mesh size $(\phi, r)$	Good cases ratio(%)	Bad cases ratio(%)
Default	78.2	21.8	$(200, 100)$	82	18
$(50, 50)$	71.8	28.2	$(200, 200)$	75.6	24.4
$(50, 100)$	59	41	$(300, 50)$	82.1	17.9
$(50, 200)$	52.6	47.4	$(300, 100)$	75.6	24.4
$(100, 50)$	80.8	19.2	$(300, 200)$	70.5	29.5
$(100, 100)$	66.7	33.3	$(400, 50)$	80.8	19.2
$(100, 200)$	60.3	39.7	$(400, 100)$	57.7	42.3
$(200, 50)$	91	9	$(400, 200)$	57.7	42.3

### 6.3 Track Reconstruction



Figure 6.15: The track reconstruction related issues in this section.

Exclude those case 6 events, we use the divided mesh size  $(\phi 96, \log r 96)$  to demo how we reconstruct the tracks.

There are two variables  $\phi$  and  $\log r$  should be defined.

We use the following equation (6.1) to define the  $\log r$ .

$$\log r = \frac{3 - 0.7}{96} \times (N_r + 0.5) + 0.7 \quad (6.1)$$

In this equation (6.1),  $\frac{3-0.7}{96}$  is the bin size of  $\log r$ , where 3 and 0.7 are the maximum and minimum value of  $\log r$  and 96 is the total divided number of bins. The  $N_r$  is the serial number of each bins. We shift 0.5 unit to obtain the center position.

Another variable  $\phi$  is defined as the following equation (6.2).

$$\phi = \frac{2\pi}{96} \times (N_\phi + 0.5) \quad (6.2)$$

In this equation (6.2),  $\frac{2\pi}{96}$  is the bin size of  $\phi$ , where  $2\pi$  and 0 are the maximum and minimum value of  $\phi$  and 96 is the total divided number of bins. The  $N_\phi$  is the serial number of each bins. We shift 0.5 unit to obtain the center position.

We can use the peak position of  $(\log r, \phi)$  in the Hough plane to obtain the center of the track circle,  $(C_x, C_y)$  in the CDC  $x - y$  plane through the transformation equation (6.3).

$$C_x = r \cos \phi, C_y = r \sin \phi \quad (6.3)$$

The Fig. 6.16 is an example. The red blocks in Hough plane are all connected with each other. We average the center position of the connected red blocks to obtain the peak position. The peak position of  $(\log r, \phi)$  in the

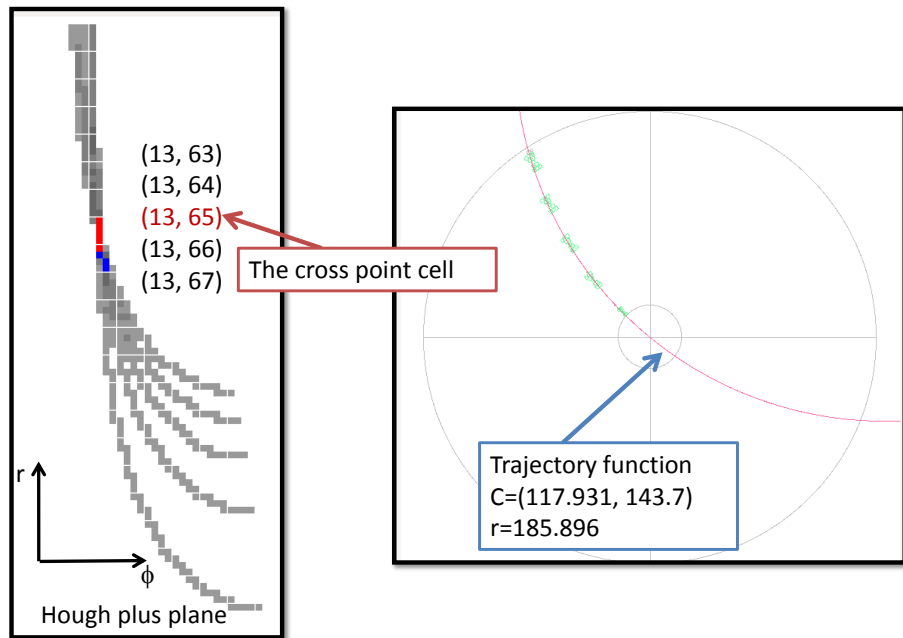


Figure 6.16: Left plot: the red blocks in Hough plane are all connected with each other. Right plot: The peak position of  $(\log r, \phi)$  in the Hough plane translate to the center of the track circle,  $(C_x, C_y)$  in the CDC  $x - y$  plane.

Hough plane is translated to the center of the track circle,  $(C_x, C_y)$  in the CDC  $x - y$  plane. Then, the 2-D trajectory function is obtained.

## 6.4 Some Testing

### 6.4.1 Some Calculations Related to Physics Laws

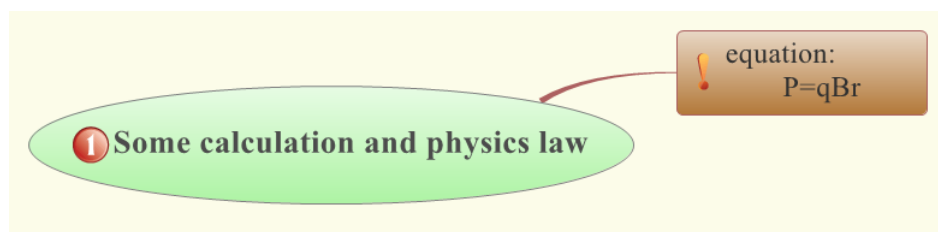
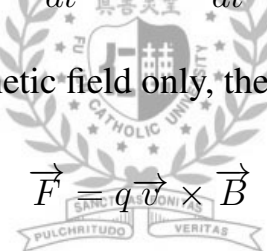


Figure 6.17: Some calculations related issues in this section.

Starting from the energy conservation:

$$\frac{dW}{dt} = mc^2 \frac{d\gamma}{dt} \quad (6.4)$$

In the presence of a magnetic field only, the Lorentz force is:



$$\vec{F} = q \vec{v} \times \vec{B} \quad (6.5)$$

Since:

$$\frac{dW}{dt} = \vec{F} \bullet \vec{v} = 0 \quad (6.6)$$

it follows that:

$$\frac{d\gamma}{dt} = 0 \quad (6.7)$$

meaning that  $\gamma$  is a constant, and so is v. This is instrumental in solving the equation of motion for a charge particle of charge q in a magnetic field of induction B as follows:

$$F = \frac{d\gamma m_0 v}{dt} = \gamma m_0 \frac{dv}{dt} \quad (6.8)$$

On the other hand:

$$\vec{F} = q \vec{v} \times \vec{B} \quad (6.9)$$

Thus:

$$\gamma m_0 \frac{dv}{dt} = q \vec{v} \times \vec{B} \quad (6.10)$$

Separating by components, we obtain:

$$qBv_y = \gamma m_0 \frac{dv_x}{dt} \quad (6.11)$$

$$-qBv_x = \gamma m_0 \frac{dv_y}{dt} \quad (6.12)$$



$$0 = \gamma m_0 \frac{dv_z}{dt} \quad (6.13)$$

The solutions are:

$$v_x = r\omega \cos(\omega t) \quad (6.14)$$

$$v_y = -r\omega \sin(\omega t) \quad (6.15)$$

$$\omega = \frac{qB}{\gamma m_0} \quad (6.16)$$

Then:

$$r = \frac{\gamma m_0 v_0}{qB} \quad (6.17)$$

$$P = \gamma m_0 v_0 = qBr \quad (6.18)$$

### 6.4.2 Different Particle vs. Track Radius

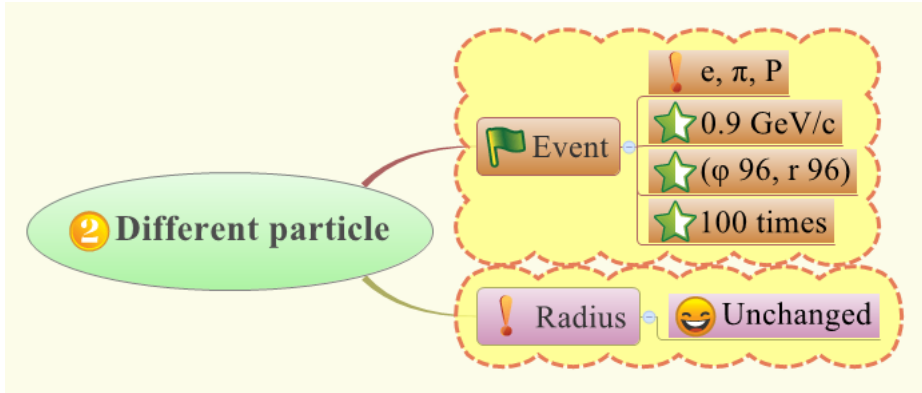


Figure 6.18: The related issues written in this section.

We know the particle passing the CDC would be affected by a uniform magnetic field 1.5 Tesla. And  $q$  is the unit of coulomb. According to the calculation in the previous equation (6.18), we can simplify that equation and obtain a new equation (6.19) as below.

$$P(GeV/c) = 0.45r \quad (6.19)$$

where  $r$  is the radius and  $P$  is the momentum.

According to the equation (6.19), the particle mass won't affect the radius. We can do some tests to confirm this physics law.

We simulate three kinds of particles with the same momentum, and study their track radius in good cases. The three kinds of particles are proton( $P$ ), pion( $\pi$ ), and electron( $e$ ). They fly through the CDC with the momentum of  $0.9 \text{ GeV}/c$ . We generate 100 events for each of them. The mesh size is divided as  $(\phi 96, r 96)$ . The table 6.4 is a summary of the settings.

Since the momentum is  $0.9 \text{ GeV}/c$ , we can easily know the expected radius is 200 cm by the equation (6.19). Let's try to find the answers from our simulation.

Table 6.4: A summary of the environment settings in this section.

Particle	$P$ $\pi^+$ $e^-$
Momentum	$0.9 \text{ GeV}/c$
Number of generated Events	100
Divided Mesh size	$(\phi 96, \log r 96)$



- Proton Sample.

The proton mass is about  $938 \text{ MeV}/c^2$ . The table 6.5 shows the number of events in each cases. The Fig 6.19 is the track radius obtaining from good cases. The averaged track radius is  $199.5 \pm 20.0$ .

Table 6.5: The number of events in each cases,  $P$  sample.

case	number of events
Case 1	0
Case 2	58
Case 3	5
Case 4	37
Case 5	0

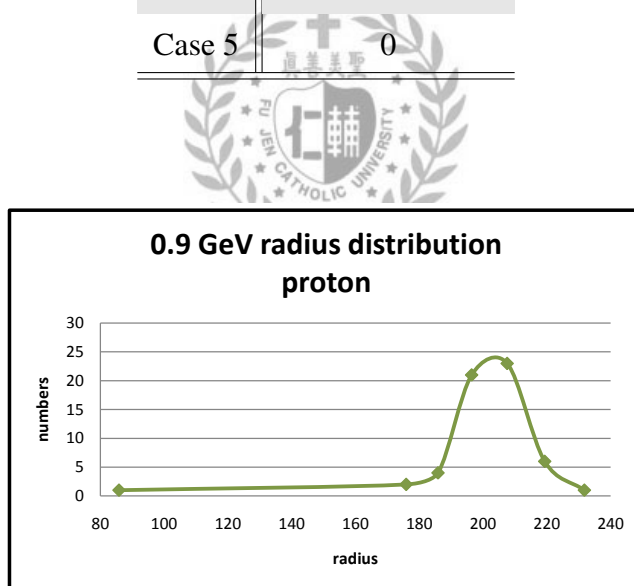


Figure 6.19: The track radius obtained from good cases,  $P$  sample.

- $\pi^+$  Sample.

The  $\pi$  meson mass is about  $140 \text{ MeV}/c^2$ . The table 6.6 shows the number of events in each cases. The Fig 6.20 is the track radius obtaining from good cases. The averaged track radius is  $201.2 \pm 20.1$ .

Table 6.6: The number of events in each cases,  $\pi^+$  sample.

case	number of events
Case 1	0
Case 2	70
Case 3	3
Case 4	27
Case 5	0

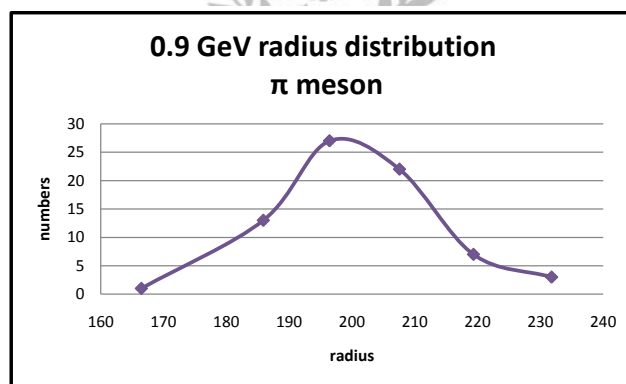
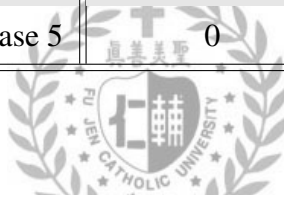


Figure 6.20: The track radius obtained from good cases,  $\pi^+$  sample.

- $e^-$  Sample.

The electron mass is about  $0.51 \text{ MeV}/c^2$ . The table 6.7 shows the number of events in each cases. The Fig 6.21 is the track radius obtaining from good cases. The averaged track radius is  $195.9 \pm 19.6$ .

Table 6.7: The number of events in each cases,  $e^-$  sample.

case	number of events
Case 1	0
Case 2	70
Case 3	10
Case 4	18
Case 5	2

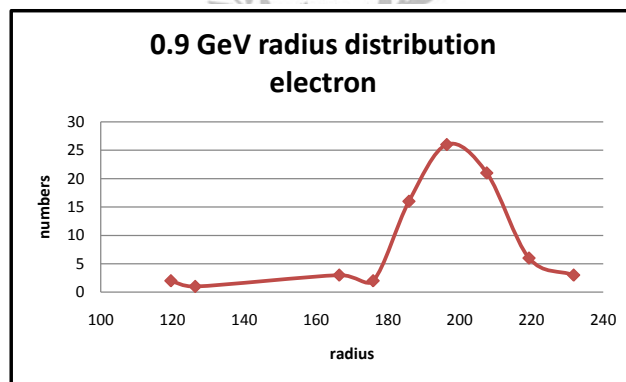
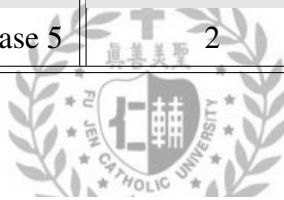


Figure 6.21: The track radius obtained from good cases,  $e^-$  sample.

The table 6.8 shows the results of track radius using  $P$ ,  $\pi^+$ , and  $e^-$  in the same momentum. We may conclude that their averaged track radius are close to each other. The results show no relationship between the track radius and the particle mass. This obeys the physics law in the relativity.

Some more details about this section are shown in the appendix B.

Table 6.8: The summary of the averaged track radius using  $P$ ,  $\pi^+$ , and  $e^-$  in the same momentum. The expected radius is 200 cm. The results are very close to the expected result.

	$P$	$\pi^+$	$e^-$
averaged track radius	$199.5 \pm 20.0$	$201.2 \pm 20.1$	$195.9 \pm 19.6$



### 6.4.3 Different Momentum vs. Track Radius

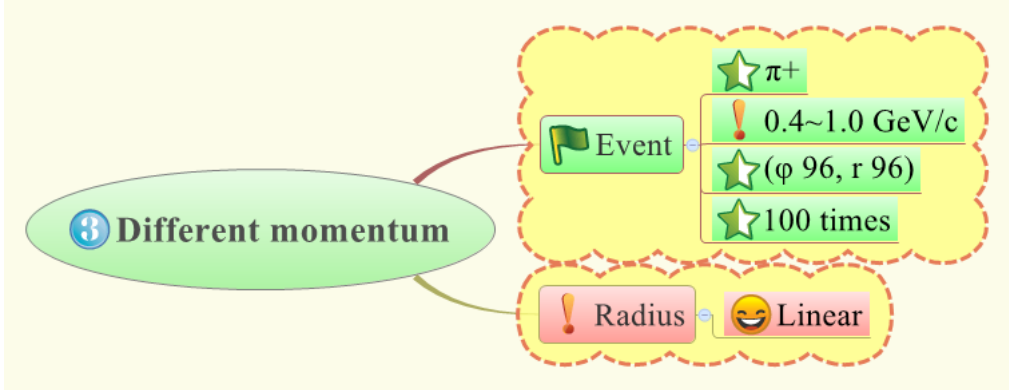


Figure 6.22: The related issues written in this section.

Again, according to the equation (6.19), we know the relationship between momentum and radius is linear. Let's find the answer in our simulation.

In our code, each size in CDC x-y plane is 1 *cm* in real space. So these average radius should be in the unit of *cm*. Before simulation, the expected radius is calculated as written in the table 6.9.

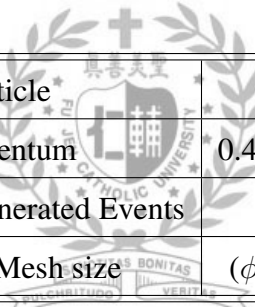
We use  $\pi^+$  carrying the momentum varying from 0.4 to 1.0  $GeV/c$ , 0.1  $GeV/c$  increased each time. Because if the momentum is less than 0.4  $GeV/c$ , the particle will not completely pass through the CDC chamber.

We generate one hundred events of each momentum range with the divided mesh size ( $\phi$  96,  $\log r$  96). The table 6.10 is the summary of the simulation settings. The detail of the results are shown in the following sections.

Table 6.9: The Momentum and the expected Radius.

Momentum ( $GeV/c$ )	radius(cm)
0.4	88.9
0.5	111.1
0.6	133.3
0.7	155.6
0.8	177.8
0.9	200
1.0	222.2

Table 6.10: A summary of the environment settings in this section.



Particle	$\pi^+$
Momentum	$0.4 \sim 1.0 GeV/c$
Number of generated Events	100
Divided Mesh size	( $\phi$ 96, log $r$ 96)

- $0.4 GeV/c$ .

The table 6.11 shows the number of events in each cases. The Fig 6.23 is the track radius obtaining from good cases. The averaged track radius of  $0.4 GeV/c$  is  $87.2 \pm 8.7$ .

Table 6.11: The number of events in each cases( $0.4 \text{ GeV}/c$ ).

case	number of events
Case 1	0
Case 2	47
Case 3	11
Case 4	6
Case 5	36

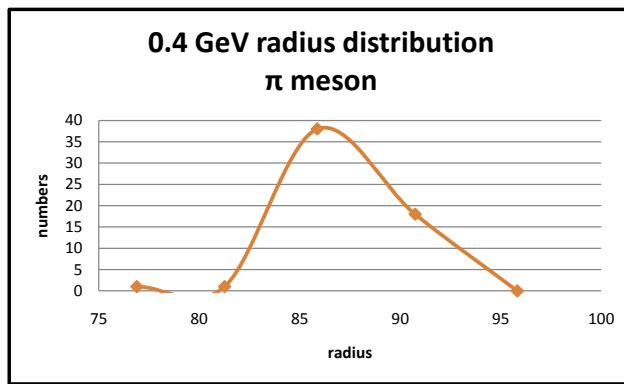


Figure 6.23: The track radius obtaining from good cases( $0.4 \text{ GeV}/c$ ).

- $0.5 \text{ GeV}/c$ .

The table 6.12 shows the number of events in each cases. The Fig 6.24 is the track radius obtaining from good cases. The averaged track radius of  $0.5 \text{ GeV}/c$  is  $110.3 \pm 11.0$ .

Table 6.12: The number of events in each cases( $0.5 \text{ GeV}/c$ ).

case	number of events
Case 1	0
Case 2	66
Case 3	13
Case 4	19
Case 5	2

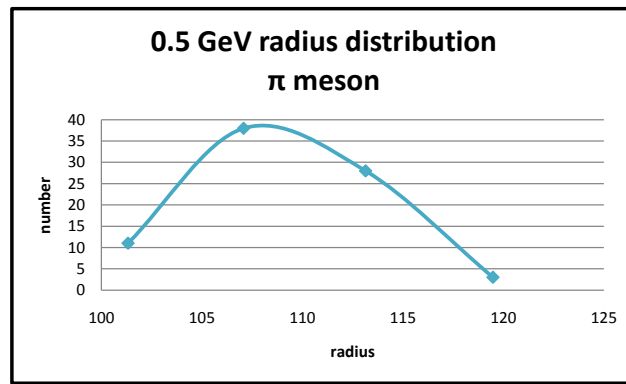


Figure 6.24: The track radius obtaining from good cases( $0.5 \text{ GeV}/c$ ).

- $0.6 \text{ GeV}/c$ .

The table 6.13 shows the number of events in each cases. The Fig 6.25 is the track radius obtaining from good cases. The averaged track radius of  $0.6 \text{ GeV}/c$  is  $130.2 \pm 13.0$ .

Table 6.13: The number of events in each cases( $0.6 \text{ GeV}/c$ ).

case	number of events
Case 1	0
Case 2	69
Case 3	5
Case 4	24
Case 5	2

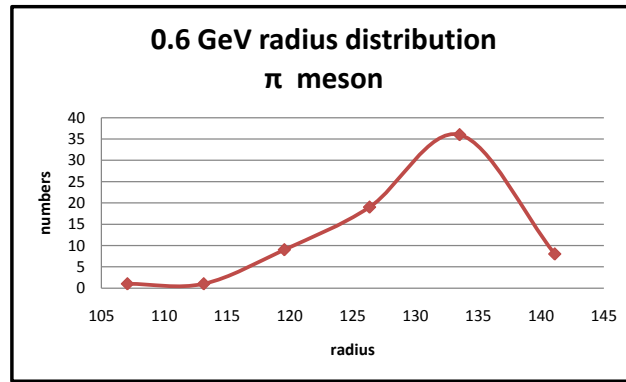


Figure 6.25: The track radius obtaining from good cases( $0.6 \text{ GeV}/c$ ).

- $0.7 \text{ GeV}/c$ .

The table 6.14 shows the number of events in each cases. The Fig 6.26 is the track radius obtaining from good cases. The averaged track radius of  $0.7 \text{ GeV}/c$  is  $154.7 \pm 15.5$ .

Table 6.14: The number of events in each cases( $0.7 \text{ GeV}/c$ ).

case	number of events
Case 1	0
Case 2	63
Case 3	9
Case 4	28
Case 5	0

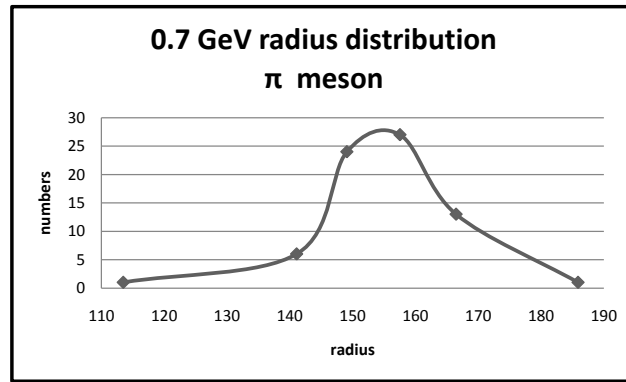


Figure 6.26: The track radius obtaining from good cases( $0.7 \text{ GeV}/c$ ).

- $0.8 \text{ GeV}/c$ .

The table 6.15 shows the number of events in each cases. The Fig 6.27 is the track radius obtaining from good cases. The averaged track radius of  $0.8 \text{ GeV}/c$  is  $180.1 \pm 18.0$ .

Table 6.15: The number of events in each cases( $0.8 \text{ GeV}/c$ ).

case	number of events
Case 1	0
Case 2	43
Case 3	26
Case 4	31
Case 5	0

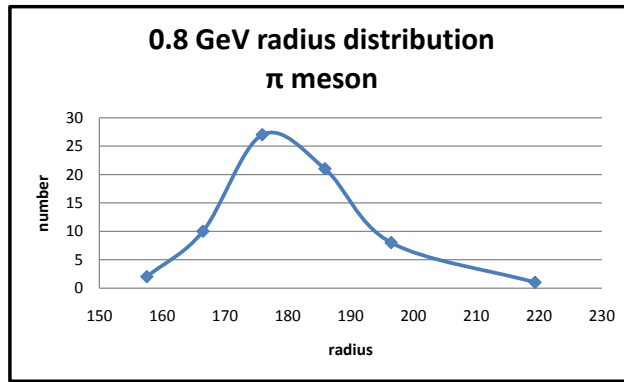


Figure 6.27: The track radius obtaining from good cases( $0.8 \text{ GeV}/c$ ).

- $0.9 \text{ GeV}/c$ .

We use the results obtained from the previous section 6.4.2. The table 6.16 shows the number of events in each cases. The Fig 6.28 is the track radius obtaining from good cases. The averaged track radius of  $0.9 \text{ GeV}/c$  is  $201.2 \pm 20.1$ .

Table 6.16: The number of events in each cases( $0.9 \text{ GeV}/c$ ).

case	number of events
Case 1	0
Case 2	70
Case 3	3
Case 4	27
Case 5	0

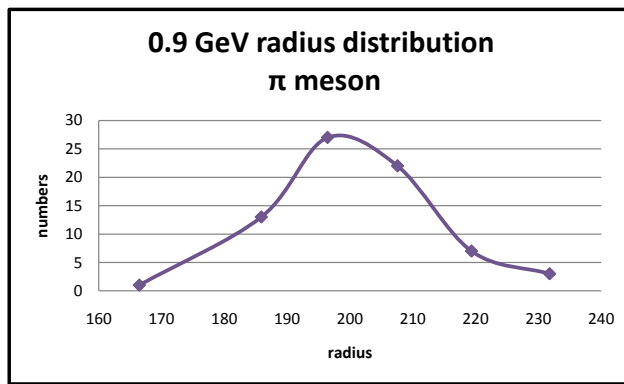


Figure 6.28: The track radius obtaining from good cases( $0.9 \text{ GeV}/c$ ).

- $1.0 \text{ GeV}/c$ .

The table 6.18 shows the number of events in each cases. The Fig 6.30 is the track radius obtaining from good cases. The averaged track radius of  $1.0 \text{ GeV}/c$  is  $227.8 \pm 22.8$ .

Table 6.17: The number of events in each cases( $1.0 \text{ GeV}/c$ ).

case	number of events
Case 1	0
Case 2	49
Case 3	21
Case 4	30
Case 5	0

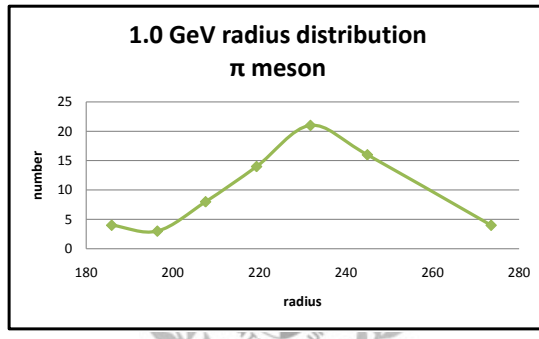


Figure 6.29: The track radius obtaining from good cases( $1.0 \text{ GeV}/c$ ).

We summarize the previous results of average radius in different momentum range in the table 6.18. The corresponding plot is shown in the Fig. 6.9. We can see a linear relationship between the radius and momentum. This obeys the physics law in the relativity.

Some more details about this section are shown in the appendix C.

Table 6.18: Summary of the average radius in different momentum range.

Momentum ( $GeV/c$ )	0.4	0.5	0.6
Averaged radius	$87.2 \pm 8.7$	$110.3 \pm 11.0$	$130.2 \pm 13.0$
0.7	0.8	0.9	1.0
$154.7 \pm 15.5$	$180.1 \pm 18.0$	$201.2 \pm 20.1$	$227.8 \pm 22.8$

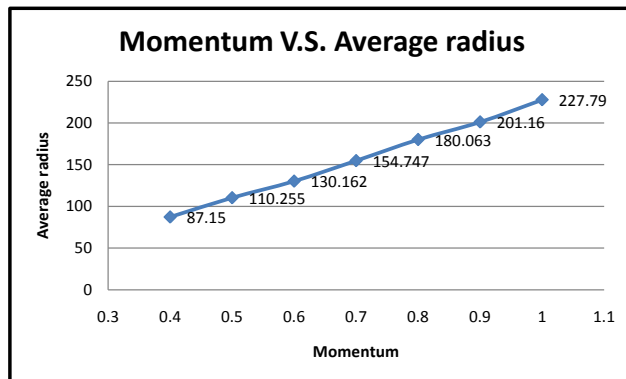


Figure 6.30: The relationship between averaged radius and momentum.

Table 6.19 shows the values of expected momentum, averaged radius and the trace back momentum from the averaged radius.

We can see the difference between input momentum and trace back momentum in each cases are all smaller than 2.5 %.

Table 6.19: The values of expected momentum, averaged radius and the trace back momentum from the averaged radius.

Input	Averaged	Trace Back	Momentum Error(%)
Momentum ( $GeV/c$ )	radius(10 mm)	Momentum ( $GeV/c$ )	
0.4	$87.15 \pm 8.7$	$0.392 \pm 0.04$	$1.96 \pm 0.20$
0.5	$110.255 \pm 11.0$	$0.496 \pm 0.05$	$0.77 \pm 0.08$
0.6	$130.162 \pm 13.0$	$0.586 \pm 0.06$	$2.37 \pm 0.24$
0.7	$154.747 \pm 15.5$	$0.696 \pm 0.07$	$0.57 \pm 0.06$
0.8	$180.063 \pm 18.0$	$0.81 \pm 0.08$	$1.290.13$
0.9	$201.16 \pm 20.1$	$0.905 \pm 0.09$	$0.58 \pm 0.06$
1.0	$227.79 \pm 22.8$	$1.025 \pm 0.10$	$2.5 \pm 0.25$

## 6.5 Mesh Size Optimization II

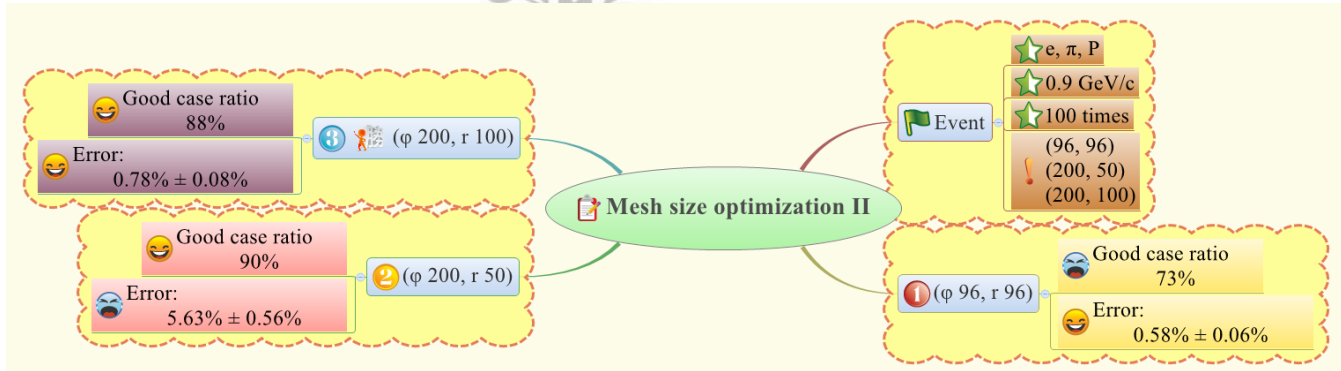


Figure 6.31: The Mesh size optimization II issues in this section.

According to the results in the previous section, we consider that the mesh size can not only be determined by the ratio of good cases. We should obtain the smaller error between the input and output momentum, too. In this sec-

tion, we try three kinds of divided mesh size to know their good case ratio and the momentum error. The simulation environment settings for mesh size optimization-II are listed in the table 6.20.

Table 6.20: The simulation environment settings for mesh size optimization-II.

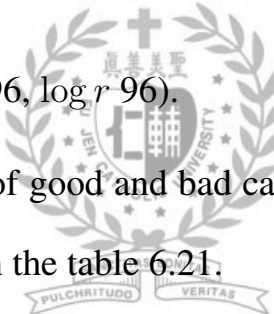
Particle	$\pi^+$
Momentum	$0.9 \text{ GeV}/c$
Number of generated events	100
Divided Mesh size	( $\phi 96, \log r 96$ ) ( $\phi 200, \log r 50$ ) ( $\phi 200, \log r 100$ )



Table 6.21: Divided mesh size ( $\phi$  96,  $\log r$  96). Left side is the number of events and the ratio of good and bad cases. Right side is the averaged radius from good cases.

cases	number of events	ratio	Circle radius	total number of events
Case 1	0	Good case	166.477	1
Case 2	70	73%	185.896	13
Case 3	3		196.44	27
Case 4	27	Bad case	207.581	22
Case 5	0	27%	219.354	7
			231.795	3
			Averaged radius	$201.2 \pm 20.1$

- Divided mesh size ( $\phi$  96,  $\log r$  96).



The events and ratios of good and bad cases, the averaged radius from good cases are listed in the table 6.21.

The ratio of good cases is about 73% and the averaged radius is about  $201.2 \pm 20.1$  cm. The trace back momentum is  $0.91 \pm 0.09$   $GeV/c$ . Comparing to the input momentum,  $0.9$   $GeV/c$ , the momentum error between the input and output is about  $0.58\% \pm 0.06\%$ .

Table 6.22: Divided mesh size ( $\phi$  200,  $\log r$  50). Left side is the number of events and the ratio of good and bad cases. Right side is the averaged radius from good cases.

cases	number of events	ratio	Circle radius	total number of events
Case 1	11	Good case	156.675	4
Case 2	69	90%	174.181	33
Case 3	10		193.642	38
Case 4	10	Bad case	215.178	14
Case 5	0	10%	239.332	1
Averaged radius				$188.7 \pm 18.9$

- Divided mesh size ( $\phi$  200,  $\log r$  50).

The events and ratios of good and bad cases, the averaged radius from good cases are listed in the table 6.22.

The ratio of good cases is about 90% and the averaged radius is about  $188.7 \pm 18.9$  cm. The trace back momentum is  $0.85 \pm 0.09$   $GeV/c$ . Comparing to the input momentum,  $0.9$   $GeV/c$ , the momentum error between the input and output is about  $5.63\% \pm 0.56\%$ .

Although the ratio of good cases is very high, but the trace back momentum is not very close to the input momentum. Maybe because the bin size in radius axis is too large. We reduce the mesh bin size in the radius axis as ( $\phi$  200,  $\log r$  100).

Table 6.23: Divided mesh size ( $\phi 200$ ,  $\log r 100$ ). Left side is the number of events and the ratio of good and bad cases. Right side is the averaged radius from good cases.

cases	number of events	ratio	Circle radius	total number of events
Case 1	8	Good case	169.629	1
Case 2	61	88%	178.855	10
Case 3	19		188.582	25
Case 4	10	Bad case	198.838	27
Case 5	2	12%	209.652	14
			221.055	7
			233.077	4
Averaged radius			$198.4 \pm 19.8$	

- Divided mesh size ( $\phi 200$ ,  $\log r 100$ ).

The events and ratios of good and bad cases, the averaged radius from good cases are listed in the table 6.23.

The ratio of good cases is about 88% and the averaged radius is about  $198.4 \pm 19.8$  cm. The trace back momentum is  $0.89 \pm 0.09$   $GeV/c$ . Comparing to the input momentum,  $0.9$   $GeV/c$ , the momentum error between the input and output is about  $0.78\% \pm 0.08\%$ .

We put the all results from previous three divided mesh sizes in the table 6.24. If we want to have a higher ratio of good case events and smaller error between input and output momentum, we can choose the divided mesh size ( $\phi$  200,  $\log r$  100). This is our final mesh size optimization result.

Table 6.24: Summary of the previous divided mesh size results.

	$(\phi 96, \log r 96)$	$(\phi 200, \log r 50)$	$(\phi 200, \log r 100)$
ratio of good cases	73%	90%	88%
Errors of momentum(%)	$0.56 \pm 0.06$	$5.63 \pm 0.56$	$0.78 \pm 0.08$



# Chapter 7

## Summary

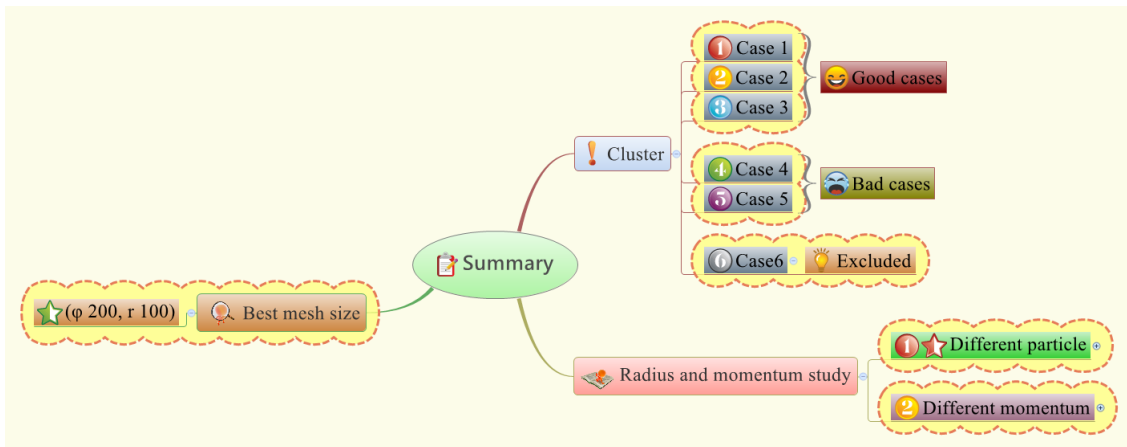


Figure 7.1: The summary related issues in this section.

We successfully use the Hough transformation to find 2D trajectory in CDC chamber.

We classify the cluster types into six. Three types are called the good cases and the rest three are called the bad cases. Among the three bad cases, we exclude the case 6 which is the mistake coming from detector boundary settings.

We optimize the mesh size by calculating the good case ratio and the

smallest momentum error. The optimization results for the divided mesh size is ( $\phi$  200,  $\log r$  100).



# Appendix

## Appendix A

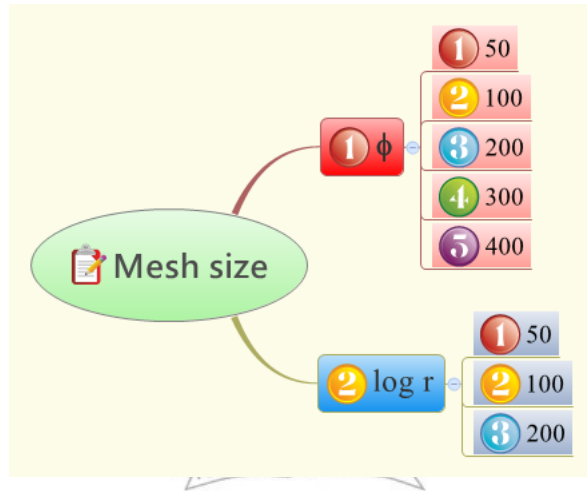


Figure 2: The related issues written in this Appendix A.

Here is the details for the mesh size study. In each mesh size, we compare the good case ratio and pick up the best mesh size as the optimization mesh size.

Table 1: ( $\phi$  50,  $\log r$  50).

case	numbers (#)	ratio (%)	Without special case (%)
Case 1	0	0	0
Case 2	49	49	62.8
Case 3	7	7	7.7
Case 4	20	20	26.9
Case 5	2	2	2.6
Case 6	22	22	$\times$

Table 2: ( $\phi$  50,  $\log r$  100).

case	numbers (#)	ratio (%)	Without special case (%)
Case 1	0	0	0
Case 2	42	42	53.8
Case 3	4	4	5.1
Case 4	30	30	38.5
Case 5	2	2	2.6
Case 6	22	22	$\times$

Table 3: ( $\phi$  50,  $\log r$  200).

case	numbers (#)	ratio (%)	Without special case (%)
Case 1	0	0	0
Case 2	39	39	50
Case 3	2	2	2.6
Case 4	35	35	44.9
Case 5	2	2	2.6
Case 6	22	22	$\times$

Table 4: ( $\phi$  100,  $\log r$  50).

case	numbers (#)	ratio (%)	Without special case (%)
Case 1	0	0	0
Case 2	48	48	61.5
Case 3	15	15	19.2
Case 4	13	13	16.7
Case 5	2	2	2.6
Case 6	22	22	$\times$

Table 5: ( $\phi$  100,  $\log r$  100).

case	numbers (#)	ratio (%)	Without special case (%)
Case 1	0	0	0
Case 2	38	38	48.7
Case 3	14	14	17.9
Case 4	24	24	30.8
Case 5	2	2	2.6
Case 6	22	22	$\times$

Table 6: ( $\phi$  100,  $\log r$  200).

case	numbers (#)	ratio (%)	Without special case (%)
Case 1	0	0	0
Case 2	36	36	46.2
Case 3	11	11	14.1
Case 4	29	29	37.2
Case 5	2	2	2.6
Case 6	22	22	$\times$

Table 7: ( $\phi$  200,  $\log r$  50).

case	numbers (#)	ratio (%)	Without special case (%)
Case 1	11	11	14.1
Case 2	53	53	67.9
Case 3	7	7	9
Case 4	5	5	6.4
Case 5	2	2	2.6
Case 6	22	22	$\times$

Table 8: ( $\phi$  200,  $\log r$  100).

case	numbers (#)	ratio (%)	Without special case (%)
Case 1	4	4	5.1
Case 2	44	44	56.4
Case 3	16	16	20.5
Case 4	12	12	15.4
Case 5	2	2	2.6
Case 6	22	22	$\times$

Table 9: ( $\phi$  200,  $\log r$  200).

case	numbers (#)	ratio (%)	Without special case (%)
Case 1	2	2	2.6
Case 2	43	43	55.1
Case 3	14	14	17.9
Case 4	17	17	21.8
Case 5	2	2	2.6
Case 6	22	22	$\times$

Table 10: ( $\phi$  300,  $\log r$  50).

case	numbers (#)	ratio (%)	Without special case (%)
Case 1	19	19	24.4
Case 2	44	44	56.4
Case 3	1	1	1.3
Case 4	10	10	12.8
Case 5	4	4	5.1
Case 6	22	22	$\times$

Table 11: ( $\phi$  300,  $\log r$  100).

case	numbers (#)	ratio (%)	Without special case (%)
Case 1	13	13	16.7
Case 2	36	36	46.1
Case 3	10	10	12.8
Case 4	11	11	14.1
Case 5	8	8	10.3
Case 6	22	22	$\times$

Table 12: ( $\phi$  300,  $\log r$  200).

case	numbers (#)	ratio (%)	Without special case (%)
Case 1	6	6	7.7
Case 2	3.6	3.6	46.2
Case 3	13	13	16.7
Case 4	12	12	15.4
Case 5	11	11	14.1
Case 6	22	22	$\times$

Table 13: ( $\phi$  400,  $\log r$  50).

case	numbers (#)	ratio (%)	Without special case (%)
Case 1	16	16	20.5
Case 2	42	42	53.8
Case 3	5	5	6.4
Case 4	2	2	2.6
Case 5	13	13	16.7
Case 6	22	22	$\times$

Table 14: ( $\phi$  400,  $\log r$  100).

case	numbers (#)	ratio (%)	Without special case (%)
Case 1	13	13	16.7
Case 2	23	23	29.5
Case 3	9	9	11.5
Case 4	14	14	17.9
Case 5	19	19	24.4
Case 6	22	22	$\times$

Table 15: ( $\phi$  400,  $\log r$  200).

case	numbers (#)	ratio (%)	Without special case (%)
Case 1	10	10	12.8
Case 2	28	28	35.9
Case 3	7	7	9
Case 4	10	10	12.8
Case 5	23	23	29.5
Case 6	22	22	$\times$

# Appendix B

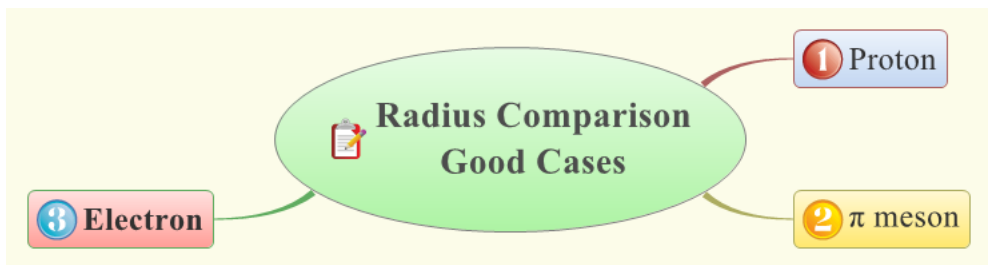
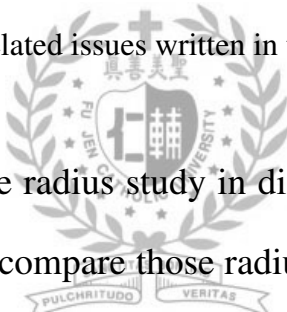


Figure 3: The related issues written in this Appendix B.



Here is the details for the radius study in different particle type: proton, pion and electron. We only compare those radius in good cases. The results obey the physics laws. No radius difference between the particle types while the particles carrying the same momentum.

Table 16: Proton

Circle radius	Case 2 numbers (#)	Case 3 numbers (#)	total numbers (#)
85.875	1	0	1
175.919	2	2	4
185.896	4	0	4
196.44	21	3	24
207.581	23	0	23
219.354	6	0	6
231.795	1	0	1



Table 17:  $\pi$  meson

Circle radius	Case 2 numbers (#)	Case 3 numbers (#)	total numbers (#)
166.477	0	1	1
185.896	13	0	13
196.44	25	2	27
207.581	22	0	22
219.354	7	0	7
231.795	3	0	3

Table 18: Electron

Circle radius	Case 2 numbers (#)	Case 3 numbers (#)	total numbers (#)
119.565	1	1	2
126.346	1	0	1
166.477	1	2	3
175.919	1	1	2
185.896	16	0	6
196.44	20	6	26
207.581	21	0	21
219.354	6	0	6
231.795	3	0	3

# Appendix C

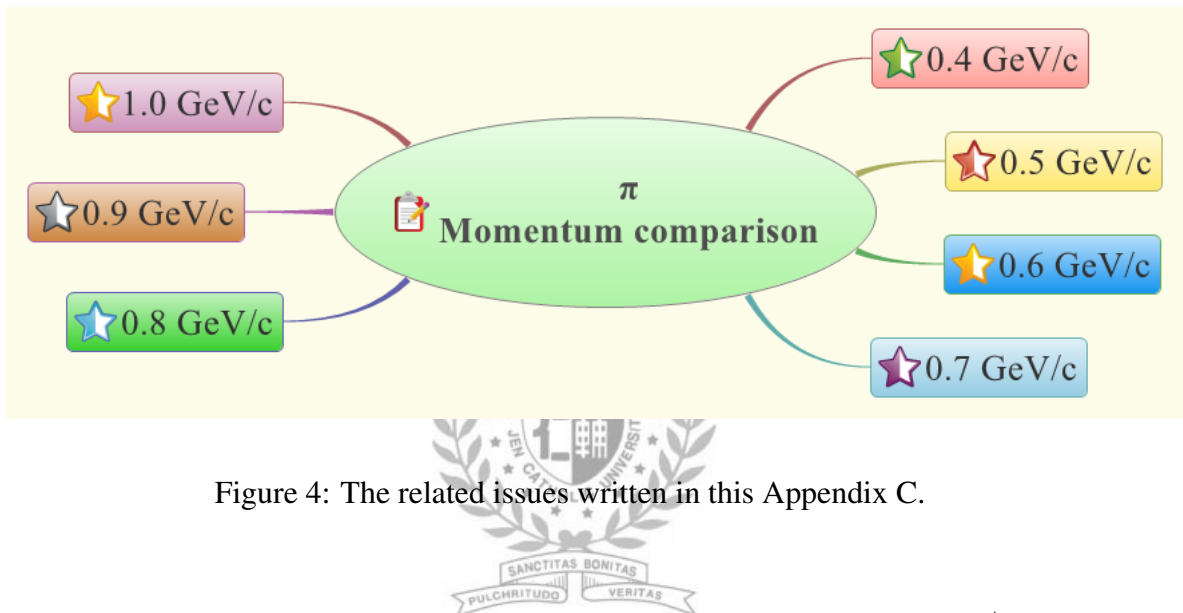


Figure 4: The related issues written in this Appendix C.



Here is the details for the momentum and radius study. The  $\pi^+$  momentum starts from 0.4 GeV to 1.0 GeV, we compare the momentum and radius relationship. It obeys the physics laws as linear relationship.

Table 19: 0.4  $GeV/c$

Circle radius	Case 2 numbers (#)	Case 3 numbers (#)	total numbers (#)
76.9	0	1	1
81.264	1	0	1
85.873	30	8	38
90.743	16	2	18

Table 20:  $0.5 \text{ GeV}/c$

Circle radius	Case 2 numbers (#)	Case 3 numbers (#)	total numbers (#)
101.328	11	0	11
107.078	27	10	37
113.148	28	0	28
119.565	0	3	3

Table 21:  $0.6 \text{ GeV}/c$

Circle radius	Case 2 numbers (#)	Case 3 numbers (#)	total numbers (#)
107.075	0	1	1
113.148	1	0	1
119.565	9	0	9
126.346	18	1	19
133.512	33	3	36
141.084	8	0	8

Table 22:  $0.7 \text{ GeV}/c$

Circle radius	Case 2 numbers (#)	Case 3 numbers (#)	total numbers (#)
113.48	1	0	1
141.084	6	0	6
149.086	19	5	24
157.542	24	3	27
166.477	13	0	13
185.896	0	1	1

Table 23:  $0.8 \text{ GeV}/c$

Circle radius	Case 2 numbers (#)	Case 3 numbers (#)	total numbers (#)
157.542	2	0	2
166.477	9	1	10
175.919	18	9	27
185.896	10	11	21
196.44	3	5	8

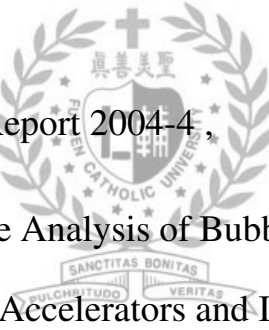
Table 24:  $0.9 \text{ GeV}/c$

Circle radius	Case 2 numbers (#)	Case 3 numbers (#)	total numbers (#)
166.477	0	1	1
185.896	13	0	13
196.44	25	2	27
207.581	22	0	22
219.354	7	0	7
231.795	3	0	3

Table 25:  $1.0 \text{ GeV}/c$

Circle radius	Case 2 numbers (#)	Case 3 numbers (#)	total numbers (#)
185.896	4	0	4
193.44	3	0	3
207.581	6	2	8
219.354	10	4	14
231.795	20	1	21
244.942	6	10	16
273.514	0	4	4

# Bibliography

- [1] <http://en.wikipedia.org/wiki/Luminosity>
- [2] A. Abashian et al. , “The Belle detector” , NIM A479,117(2002)
- [3] Z. Dolezal and S. Uno et al. , “Belle II Technical Design Report” , KEK Report(2010)
- [4] M. Akatsu et al. KEK Report 2004-4 ,  

- [5] P.V.C Hough , “Macgine Analysis of Bubble Chamber Pictures” , Proc. Int. Conf. High Energy Accelerators and Instrumentation, 1905
- [6] <http://belle.kek.jp/>
- [7] <http://ekpbelle2.physik.uni-karlsruhe.de/twiki/bin/view>